

Colloidal Metal-Halide Perovskite Nanoplatelets: Thickness-Controlled Synthesis, Properties, and Application in Light-Emitting Diodes

Clara Otero-Martínez, Junzhi Ye, Jooyoung Sung, Isabel Pastoriza-Santos, Jorge Pérez-Juste, Zhiguo Xia, Akshay Rao, Robert L. Z. Hoyer, and Lakshminarayana Polavarapu*

Colloidal metal-halide perovskite nanocrystals (MHP NCs) are gaining significant attention for a wide range of optoelectronics applications owing to their exciting properties, such as defect tolerance, near-unity photoluminescence quantum yield, and tunable emission across the entire visible wavelength range. Although the optical properties of MHP NCs are easily tunable through their halide composition, they suffer from light-induced halide phase segregation that limits their use in devices. However, MHPs can be synthesized in the form of colloidal nanoplatelets (NPLs) with monolayer (ML)-level thickness control, exhibiting strong quantum confinement effects, and thus enabling tunable emission across the entire visible wavelength range by controlling the thickness of bromide or iodide-based lead-halide perovskite NPLs. In addition, the NPLs exhibit narrow emission peaks, have high exciton binding energies, and a higher fraction of radiative recombination compared to their bulk counterparts, making them ideal candidates for applications in light-emitting diodes (LEDs). This review discusses the state-of-the-art in colloidal MHP NPLs: synthetic routes, thickness-controlled synthesis of both organic–inorganic hybrid and all-inorganic MHP NPLs, their linear and nonlinear optical properties (including charge-carrier dynamics), and their performance in LEDs. Furthermore, the challenges associated with their thickness-controlled synthesis, environmental and thermal stability, and their application in making efficient LEDs are discussed.


1. Introduction

2D colloidal semiconductor nanocrystals have attracted significant attention due to their unique optical and optoelectronic properties that are distinct from their bulk counterparts.^[1–9] These properties include the ability to tune their emission wavelength through the thickness of the nanocrystals, large absorption cross-sections, narrow emission peaks, higher exciton binding energies than their bulk counterparts, high photoluminescence quantum yields, and giant oscillator strengths.^[3,5–7] Over the past two decades, classical 2D semiconductor nanocrystals, such as CdSe, ZnS, and CdSe/CdS core/shell nanoplatelets or nanobelts, have attracted significant attention, with many works aiming to understand their optical and electronic properties, as well as to explore their potential applications in bioimaging, light-emitting diodes (LEDs) and lasers, among others.^[10–13] Recently, metal-halide perovskite nanocrystals (MHP NCs), especially lead-halide perovskite

C. Otero-Martínez, L. Polavarapu
CINBIO, Universidade de Vigo, Materials Chemistry and Physics Group,
Department of Physical Chemistry
Campus Universitario Lagoas, Marcosende
Vigo 36310, Spain
E-mail: lakshmi@uvigo.es

C. Otero-Martínez, I. Pastoriza-Santos, J. Pérez-Juste
CINBIO, Universidade de Vigo, Department of Physical Chemistry
Campus Universitario Lagoas, Marcosende
Vigo 36310, Spain

C. Otero-Martínez, I. Pastoriza-Santos, J. Pérez-Juste
Galicia Sur Health Research Institute (IIS Galicia Sur). SERGAS-UVIGO
Vigo 36310, Spain

 The ORCID identification number(s) for the author(s) of this article can be found under <https://doi.org/10.1002/adma.202107105>.

© 2022 The Authors. Advanced Materials published by Wiley-VCH GmbH. This is an open access article under the terms of the Creative Commons Attribution License, which permits use, distribution and reproduction in any medium, provided the original work is properly cited.

J. Ye, J. Sung, A. Rao
Cavendish Laboratory
University of Cambridge
19 JJ Thomson Avenue, Cambridge CB3 0HE, UK

J. Sung
Department of Emerging Materials Science
DGIST
Daegu 42988, Republic of Korea

Z. Xia
School of Physics and Optoelectronics
State Key Laboratory of Luminescent Materials and Devices and Guangdong
Provincial Key Laboratory of Fiber Laser Materials and Applied Techniques
South China University of Technology
Guangzhou, Guangdong 510641, P. R. China

R. L. Z. Hoyer
Department of Materials
Imperial College London
Exhibition Road, London SW7 2AZ, UK

DOI: 10.1002/adma.202107105

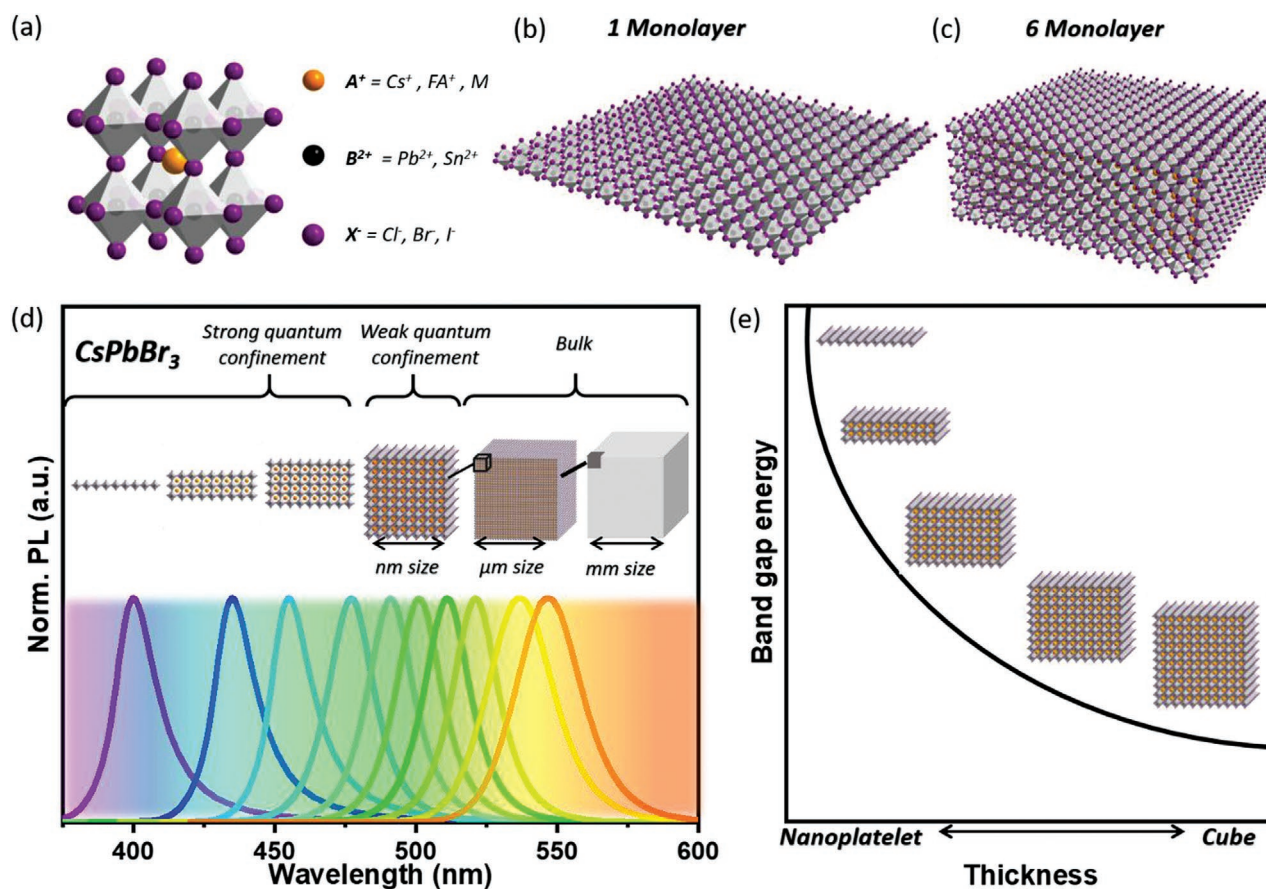


Figure 1. a) Typical cubic crystal structure of ABX_3 perovskites (A = methylammonium (MA) or formamidinium (FA) or cesium (Cs) cation, B = lead (Pb) or Tin (Sn) divalent cation, X = chloride, bromide or iodide). b,c) Schematic illustration of a monolayer and a six-layer perovskite NPLs. d) Spectral illustration of the approximate PL spectra for bulk, weakly confined nanocubes and nanoplattlets of $CsPbBr_3$. All spectra are manually drawn based on the literature reports. e) Schematic representation of the thickness-dependent emission energy of lead halide perovskite NPLs.

NCs (LHP NCs), have emerged as a new class of semiconductors with many interesting characteristics, such as defect-tolerance (for bromide and iodide-based perovskites), long charge-carrier diffusion lengths, and facile synthesis with a wide range of low-temperature, solution-based methods.^[14–22] Unlike classical core/shell semiconductor NCs, MHP NCs can achieve extremely high PLQYs (in some cases close to unity) without requiring a wide-bandgap passivation shell, which arises in part from their defect tolerant nature, but also from the ability to passivate surface defects with a wide range of functionalized ligands.^[14,15,19,23,24] Recently, research into MHP NCs has been sparked not only for the fundamental understanding of their nanoscale optical properties but also by their appeal in various technological applications.^[14] Bulk MHPs exhibit an ABX_3 perovskite cubic crystal structure, where A is a monovalent organic (e.g., methylammonium (MA^+) or formamidinium (FA^+)) or inorganic (Cs^+) cation, B is a divalent cation (Pb^{2+} , Sn^{2+} or Ge^{2+}), and X is a halide ion (Cl^- , Br^- or I^-). The typical 3D ABX_3 perovskite crystal structure is illustrated in **Figure 1a**, in which the B cation is coordinated to six halide anions in an octahedral arrangement, while the A -site cation occupies the cuboctahedral vacancies. The optical properties of MHP NCs are generally tunable by varying the composition of these constituent ions (A , B , and X).^[14,16,25,26] For instance, the bandgap

of LHP NCs is finely tunable across the visible range by tuning the halide composition from pure iodide (near-infrared) to bromide (visible) to chloride (ultraviolet).^[14,25,26]

1.1. General Features of Halide Perovskite Nanoplattlets

The optical and electronic properties of halide perovskites are also tunable by accessing quantum confinement effects in these materials, which can be achieved by reducing the size of at least one dimension below the Bohr diameter (≈ 7 nm for $CsPbBr_3$).^[14,16,27] Over the last few years, significant progress has been made in the colloidal synthesis of MHP NCs with excellent shape-control, ranging from nanocubes to nanowires, nanorods, and nanoplattlets.^[14,18] Among all, 2D and quasi-2D nanoplattlets (NPLs) have been receiving special attention owing to their thickness-dependent optical properties caused by the 1D spatial confinement of charge carriers.^[9,25,28–30] Halide perovskite NPLs generally exhibit narrow absorption and emission (fwhm ≈ 10 – 15 nm) features with small Stokes shift (<10 meV), regardless of their lateral dimensions, meaning that the emission wavelength is mainly dependent on the thickness of the NPLs, while it is less dependent on their lateral dimensions.^[25,28–32] Thus 2D NPLs exhibit blue-shifted emission

compared to their bulk counterparts, and the extent of the blue-shift depends on their thickness. As the NPLs get thinner, they no longer possess an ABX_3 chemical composition, instead, they can be represented with the composition $L_2[ABX_3]_{n-1}BX_4$, where L is a ligand (long-chain alkylammonium cation), and n is the number of octahedral monolayers (MLs).^[25] The monolayer (ML) refers to the 2D layer of PbX_6^{4-} octahedra, as illustrated in Figure 1b. However, for convenience, we still call these perovskites as ABX_3 NPLs in this review.

The thickness of colloidal perovskite NPLs is precisely controllable from a strongly quantum-confined monolayer (Figure 1b) to weakly quantum-confined few monolayers (Figure 1c).^[25,28,30,32,33] Figure 1d illustrates the expected photoluminescence (PL) spectra for bulk, weakly-confined nanocubes, and nanoplatelets of $CsPbBr_3$.^[26,29–31,33] According to literature survey, bulk single-crystals (millimeter and micron size) and polycrystalline thin films of $CsPbBr_3$ exhibit weak PL in the range of ≈ 530 – 560 nm,^[34–38] while the corresponding nanocubes (≈ 8 – 12 nm) exhibit a strong PL peak in the range of ≈ 510 – 520 nm.^[16,26,29] The PL peak of nanocubes compared to bulk single crystals suggests that the nanocubes are weakly quantum-confined. On the other hand, the $CsPbBr_3$ NPLs exhibit further blue-shifted emission compared to nanocubes and their PL peak varies between ≈ 400 and 500 nm depending on their thickness (Figure 1d).^[29–31] For instance, monolayer $CsPbBr_3$ NPLs exhibit PL ≈ 400 nm, which is significantly blue-shifted compared to nanocubes, suggesting strong quantum confinement.^[33] Figure 1e illustrates the thickness-dependent emission energy trend for lead halide perovskite NPLs. As the thickness of the NPL decreases, the emission energy nonlinearly increases due to the strong quantum confinement of thinner NPLs.^[29] Similarly, the emission wavelength for $CsPbI_3$ NPLs is tunable from ≈ 525 to 700 nm by controlling their thickness.^[31] Thus, the emission color is tunable across the visible wavelength range by controlling the thickness of bromide and iodide-based lead halide perovskite NPLs.^[31] **Table 1** provides a summary of PL peaks for inorganic–organic hybrid and inorganic colloidal perovskite NPLs of different thicknesses (in terms of numbers of monolayers (ML)).

Over the last five years, we have witnessed great progress in the synthesis of MHP NPLs with monolayer-level control over their thickness.^[9,14,25,29–31,33,64] It has been found that the synthetic method, reaction temperature, and ligands (surfactants) play a crucial role in the synthesis of colloidal MHP NPLs. The early reports on the synthesis of hybrid perovskite NPL were

inspired by the fabrication of Ruddlesden–Popper (R.-P.) phase layered metal halide perovskites reported in the 1980s and 1990s using long alkyl chain ammonium molecules as A-site cations.^[65,66] These layered perovskites are thin films consisting of alternative metal halide octahedral layers and long alkyl chain ammonium cations.^[67] The octahedral layers in between dielectric organic layers exhibit a strong quantum confinement effect and thus have distinct optical and electronic properties compared to bulk thin films, and they have many similarities with the properties of colloidal NPLs well-dispersed in solutions.^[1,67] First, this approach was extended to the synthesis of atomically thin 2D organic–inorganic hybrid perovskite nanosheets on a substrate by using a ternary cosolvent.^[68] Later, it was demonstrated that the introduction of long-chain ammonium halides in the precursor solution of perovskites results in the formation of 2D hybrid colloidal perovskite NPLs instead of 3D perovskites by ligand-assisted reprecipitation approach.^[28,69] In addition, other methods such as temperature control,^[31] ultrasonication approaches,^[26,70,71] spontaneous crystallization in organic medium,^[56] etc. have been reported for the thickness controlled synthesis of both organic–inorganic hybrid and all-inorganic perovskite NPLs, and are discussed in the general synthesis methods section.

In this review, we first discuss the general synthesis methods developed for the thickness-controlled synthesis of MHP NPLs, followed by the state of the art in the synthesis of organic–inorganic hybrid and all-inorganic perovskite NPLs. In addition, recent developments in the synthesis of lead-free perovskite NPLs are also provided. We then discuss the current understanding of nonlinear optical properties and charge-carrier dynamics of perovskite NPLs before presenting the research progress in perovskite NPL-based LEDs and the efficiencies achieved for different colors. Finally, we present the outstanding challenges that still remain in the thickness control of perovskite NPLs, their colloidal stability, and achieving high-efficiency LEDs.

2. Synthesis of Nanoplatelets

2.1. General Synthesis Methods

In general, most of the methods reported for the synthesis of perovskite nanocrystals are also applicable to NPLs under

Table 1. Summary of the range of PL peaks reported for different kinds of halide perovskite NPLs of different thicknesses in terms of the number of monolayers (ML).

	$CsPbBr_3$	$MAPbBr_3$	$FAPbBr_3$	$CsPbI_3$	$MAPbI_3$	$FAPbI_3$
1 ML	403–405 ^[25,31]	396–406 ^[25,28,39–41]	398–403 ^[25,39]	513 ^[25]	513–527 ^[25,39,42–45]	513 ^[25,39]
2 ML	433–435 ^[25,29,31,46,47]	431–440 ^[25,28,40,41,48,49]	434–440	559–565 ^[25,50]	574–584 ^[25,32,39,42–45,50]	575–580 ^[25,39,50–52]
3 ML	449–462 ^[25,29,31,46,47,53]	445–456 ^[28,40,41,54]	470 ^[55]	600 ^[26]	616–625 ^[42–45]	620–630 ^[51,56]
4 ML	470–475 ^[29–31,46,47,56,57]	456–477 ^[28,32,40,41,49]	490 ^[55]	623–633 ^[26,47,56]	650–652 ^[43–45,58]	650 ^[56]
5 ML	487–488 ^[29,31,47,57]	482–485 ^[28]	–	647–655 ^[26,47]	677 ^[45] [R.-P.] ^{a)}	–
6 ML	492–495 ^[29,57,59]	489–490 ^[28,49]	–	682–685 ^[26,47,60]	–	–
NCs	512–515 ^[16,29,31]	520 ^[28]	530 ^[61]	680–685 ^[16,52]	740 ^[62]	740–780 ^[52,63]

^{a)}R.-P.: Ruddlesden–Popper perovskite NPLs.

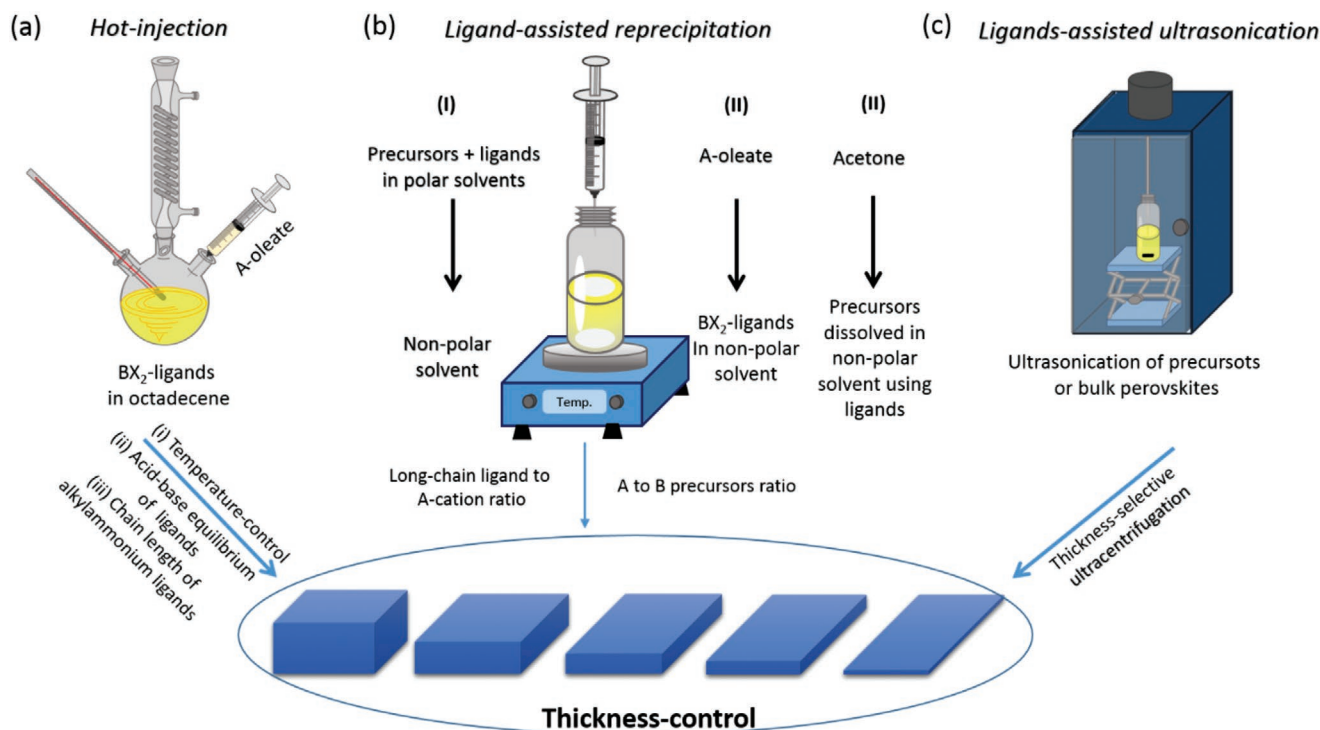


Figure 2. a) Hot-injection synthesis in which monovalent cation (A^+)-oleic acid complex so-called A-oleate, is usually injected into a mixture of divalent metal salt (BX_2) and ligands in octadecene. Generally, hot-injection synthesis carried out at reaction temperatures ≤ 130 °C usually produces NPLs. b) Ligand-assisted reprecipitation: (i) perovskite precursors and long-chain alkylammonium ligands dissolved in a good solvent are usually injected into a non-polar solvent to initiate the crystallization of perovskite NPLs; (ii) spontaneous crystallization of perovskite NPLs by the addition of A-oleate solution into pre-synthesized BX_2 -ligand dissolved in a non-polar solvent such as toluene. c) Ultrasonication approach in which precursor salts and ligands are dissolved in a solvent followed by tip-sonication of the resultant mixture. This method generally produces a mixture of NPLs of different thicknesses which then have to be separated by thickness-selective ultracentrifugation.

optimized conditions. The key parameters to control for NC synthesis include the reaction temperature, precursor ratio, ligand concentration, acid-base equilibrium of ligands, and chain-length of alkylamine ligands.^[9,14,18,72,73] The synthesis methods for perovskite NPLs can be broadly classified into three main categories, as illustrated in **Figure 2**. Among these, hot injection has been extensively explored for the shape-controlled synthesis of inorganic perovskite NCs.^[14,18] Although a wide range of ligands have been explored in the hot-injection synthesis of perovskite NCs, the combination of oleylamine (OLA) and oleic acid (OA) has been the most successful in achieving excellent shape control. This approach is based on the injection of a presynthesized monovalent cation-oleic acid complex (A-oleate) into a mixture of divalent metal salt and ligands in octadecene at a specific reaction temperature (Figure 2a). This method generally yields NPLs at reaction temperatures below ≈ 130 °C, and their thickness is tunable from a monolayer (1 ML) to a few layers by controlling the temperature.^[30] The thickness of NPLs decreases by decreasing the reaction temperature. However, a recent study by Otero-Martínez et al.^[73] found that the decrease of reaction temperatures initially leads to a decrease in the edge length of nanocubes, while only below 100 °C yields monodisperse NPLs. Therefore, further in-depth studies are needed to explore other reaction conditions required for achieving precise control over the thickness of NPLs by the reaction temperature. Besides, the concentration of ligands and

the chain length of ligands along with reaction temperature plays an important role in the formation of perovskite NPLs in hot-injection synthesis.^[33,74,75] For instance, Almeida et al. demonstrated the formation of NPLs at high reaction temperature (≈ 190 °C) by increasing the ratio of alkylammonium ion to monovalent cation in the reaction medium.^[33]

The second strategy that has been widely used for the synthesis of perovskite NCs, especially for NPLs, is the ligand-assisted reprecipitation (LARP) approach (Figure 2b).^[22,25,28,29,32,56,76,77] In this method, perovskite precursors dissolved in a good solvent (such as *N,N*-dimethylformamide (DMF), dimethylsulfoxide (DMSO), etc.), and a poor solvent (such as toluene, hexane, etc.) is subsequently added in the presence of ligands to induce the formation of perovskite NCs through supersaturation (Figure 2bi). In the case of hybrid perovskites, this LARP approach often produces NPLs, and their thicknesses are tunable by varying the ratio between long-chain and short-chain (MA or FA) alkylammonium ligands. The thickness of NPLs decreases with increasing the concentration of long-chain ligands with respect to the A-site cations. The LARP approach has also been extended to inorganic lead halide perovskite nanocubes^[55] as well as NPLs of different thicknesses with slight modifications.^[29,30,56] For example, the addition of A-oleate to BX_2 -ligand complex dissolved in non-polar solvent (such as toluene) leads to the formation of NPLs, and their thickness is controllable through the ratio of monovalent to divalent

cation–ligand complexes (Figure 2bii).^[56] Besides, the addition of acetone (a polar aprotic solvent) to a nonpolar solvent containing precursors and ligands induces the formation of NPLs at room temperature, with tunable varying the ratio of A-oleate to BX_2 precursor in the reaction medium (Figure 2biii).^[29] This approach is generally applicable to both hybrid and inorganic perovskite NPLs. The third synthesis method for perovskite NPLs is based on ligand-assisted ultrasonication (tip-sonication) of precursor powders together with ligands in a nonpolar solvent, typically toluene or octadecene.^[26,70] This strategy is also applicable to transform bulk perovskite crystals into a mixture of NPLs of different thicknesses that could be separated into individual thicknesses by ultracentrifugation.^[71] In addition to these three common synthesis methods, solvothermal and microwave-assisted synthesis have also been reported for the preparation of NPLs.^[78–80]

In the following sections, we discuss the synthesis of organic–inorganic hybrid, all-inorganic, and lead-free perovskite NPLs with controlled thickness using different protocols. **Table 2** provides a summary of the most relevant reports on the thickness-controlled synthesis of organic–inorganic hybrid and inorganic halide perovskite NPLs by different synthesis methods.

2.2. Synthesis of Organic–Inorganic Perovskite Nanoplatelets

In 2014, Pérez-Prieto and co-workers first reported the highly green emissive ($\approx 80\%$ PLQY) colloidal organic–inorganic hybrid perovskites (MAPbBr_3) by acetone-induced reprecipitation of precursor salts (MABr and PbBr_2) in a mixture of DMF and octadecene and in the presence of ligands (octylammonium bromide and oleic acid).^[22,103] The transmission electron microscopy (TEM) characterization of the samples revealed the presence of both spherical nanoparticles (NPs) and NPLs, which were assigned as perovskites and organic impurities, respectively.^[103] However, around 2015, Tyagi et al.^[69] and Sichert et al.^[28] simultaneously reported the formation of quantum-confined colloidal MAPbBr_3 perovskite NPLs by repeating the synthesis initially reported by Pérez-Prieto and co-workers. In particular, Sichert et al.^[28] demonstrated that the thickness of NPLs is tunable from bulk to strongly quantum-confined 2D monolayers by tuning the ratio of octylammonium bromide to MABr (**Figure 3a–d**). They showed that the thickness of NPLs decreases with increasing the octylammonium bromide content in the precursor solution, and they were the first to assign the PL peaks for NPLs of thicknesses $n = 1–5$. The decrease in the thickness of NPL clearly reflects in the PL spectra with a significant blue-shift due to quantum size effect (**Figure 3b**; see **Table 1** for the thickness-dependent PL peak position for MAPbBr_3 perovskite NPLs). Importantly, Sichert et al.^[28] found that the spherical NPs observed by TEM are lead (Pb^0) particles which were evolved by the electron beam-induced degradation of perovskite NPLs (We recommend reading ref ^[14] for more details on electron microscopy characterization of perovskite NCs). Meanwhile, Dou et al. reported the fabrication of atomically thin (monolayer) single-crystalline 2D NPLs of hybrid perovskites on a substrate by controlled solvent evaporation of a drop of a dilute solution of precursor salts dissolved in a ternary co-solvent system (acetonitrile, DMF, chlorobenzene)

and butylammonium bromide.^[68] The 2D NPLs exhibited a well-defined square shape with a lateral size of few microns, which enabled to study of their optical properties at single-particle level. However, unlike the colloidal solutions, the NPLs on the substrate are made of stacks of ML perovskites separated by organic cations, in which the 2D MLs are held by weak van der Waals interactions.^[104] Since there is a significant separation in between MLs, they still exhibit monolayer-like optical properties regardless of the thickness of the NPL on the substrate. The optical properties of these monolayer perovskites on the substrate are tunable across the visible range by the halide composition.^[68] Such monolayer hybrid perovskites can also be prepared in colloidal suspensions. Tisdale's group has done excellent work on the synthesis and study of the optical properties of hybrid perovskite NPLs of different compositions.^[25] They demonstrate the preparation of mono- and bilayer ($n = 1$ and 2) hybrid perovskite NPLs of different compositions (A: Cs, MA and FA, B: Pb and Sn, X: Cl, Br and I) by LARP using octylammonium or butylammonium ligands (**Figure 4**). The NPLs prepared exhibited a broad distribution of lateral sizes ranging from 100 nm to 1 μm , which had the tendency to self-assemble into stacked superlattices. The thickness of the NPLs was determined by XRD through periodic reflections from NPL stacks. **Figure 4c** presents the absorption and PL spectra of FA-based mono- and bilayer perovskite NPLs with different B-site cations (Pb and Sn) and halides (Cl, Br, and I). A summary of their PL peak positions is included in **Table 1**. Despite the polydispersity in their lateral dimensions, the NPLs exhibit narrow emission because of the fact that the lateral size has less influence on their emission energy. The emission properties of perovskite NPLs are tunable from visible to NIR range by the halide composition and B-site cation, while the A-site cation has subtle influence on their properties. However, the A-site cation selected has significant influence on the colloidal stability and PLQY of the NPLs. It was found that the FA-based NPLs exhibit significantly higher PLQY compared to MA and Cs-based NPLs.^[25] Nevertheless, FA perovskite NPLs suffer from colloidal instability. Replacing FA with MA, and the addition of excess alkylammonium bromide ligands leads to a drastic enhancement in the stability of perovskite NPLs in both colloidal solution as well as in thin films.^[105] Furthermore, it was found that the freshness of the precursor solution is important for obtaining stable colloidal hybrid perovskite NPLs with high PLQY.^[105] Very recently, Biesold et al. integrated the LARP approach with microfluidic synthesis for the continuous production of R.-P. perovskite NPLs.^[106] Using this approach, they demonstrated the fabrication of monolayer stacked perovskite NPLs, with synthesis rates 8 times higher than conventional batch methods. Interestingly, it has been demonstrated that the use of chiral ammonium halide ligands in the LARP approach results in the formation of chiral MAPbBr_3 NPLs.^[107]

Besides using alkylammonium halide ligands, long-chain alkylamines (such as OLA) in combination with alkyl acids (such as OA) has been used to prepare hybrid perovskite NPLs of different thicknesses by the LARP approach.^[32,63,91,95] In this case, it is most likely that the acid reacts with the amine to form an ammonium cation that stabilizes the colloidal perovskite NCs. Zhang et al. initially reported this approach, in which they claimed the formation of spherical NCs.^[76] However,

Table 2. Summary of synthesis methods and thickness-selective strategies reported for lead halide and lead-free perovskite NPLs with different A-site cations (Cs, MA, FA).

Thickness-controlled synthetic strategies							
	Composition	Year	Synthesis method	Tunability strategy	Range (PL)	Range (ML)	Refs.
CsPbX ₃ perovskite nanoplatelets	CsPbBr ₃	2015	Hot injection	Reaction temperature	403–478 nm	1–5	[31]
	CsPbBr ₃	2016	LARP	HBr concentration	438–459 nm	3–5	[30]
	CsPbBr ₃	2016	Hot injection	Short and long chain ligands ratio	452–491 nm	3–4	[81]
	CsPbBr ₃	2016	LARP	Precursors ratio (LX:BX ₂ :AX)	403–433 nm	1–2	[25]
	CsPbBr ₃	2016	Hot injection	Reaction temperature	462–501 nm	–	[82]
	CsPbBr ₃	2016	Hot injection	–	449 nm	–	[74]
	CsPbBr ₃	2016	Hot injection	Reaction temperature and ligands length	460–495 nm	3–7	[75]
	CsPbBr ₃	2018	LARP	–	462 nm	3	[53]
	CsPbBr ₃	2018	LARP	Precursors ratio (Cs ⁺ :PbBr ₂)	432–497 nm	2–6	[29]
	CsPbBr ₃	2018	LARP	Ligand concentration	481–510 nm	4–12	[57]
	CsPbBr ₃	2018	Hot injection	[Cs ⁺]	403–464 nm	1–4	[33]
	CsPbBr ₃	2018	LARP	H ₂ O concentration	505–518 nm	–	[83]
	CsPbBr ₃	2019	Hot injection	–	492 nm	6	[59]
	CsPbBr ₃	2020	LARP + heating-up	–	450 nm	3	[84]
	CsPbBr ₃	2020	Hot injection	–	510 nm	8	[85]
	CsPbBr ₃	2021	LARP	Precursors ratio (Cs ⁺ : PbBr ₂)	430–501 nm	–	[86]
	CsPbBr ₃	2021	Hot injection	–	446 nm	–	[87]
	CsPbBr ₃	2021	LARP	–	460 nm	3	[88]
	CsPbI ₃	2016	LARP	Precursors ratio (LX:BX ₂ :AX)	512–561 nm	1–2	[25]
	CsPbI ₃	2016	Tip -ultrasonication	Precursors ratio (Cs ⁺ :PbI ₂)	600–685 nm	3–6	[26]
	CsPbI ₃	2020	LARP	–	560 nm[RP] ^{a)}	2	[50]
	MAPbBr ₃	2015	LARP	Thickness-selective centrifugation	–504 nm	2–7	–
	MAPbBr ₃	2015	LARP	Ligand:precursor ratio (L:MA ⁺)	427–508 nm	2–6	[28]
MAPbX ₃ perovskite nanoplatelets	MAPbBr ₃	2016	LARP	Ligand length and precursors ratio	403–530 nm	1–5	[89]
	MAPbBr ₃	2016	LARP	Precursor ratio (LX:BX ₂ :AX)	398–437 nm	1–2	[25]
	MAPbBr ₃	2016	LARP	Ligand length and ratio	433–506	2–7	[90]
	MAPbBr ₃	2016	LARP	Ligand and precursor ratio	440–490 nm	1 – n > 3	[40]
	MAPbBr ₃	2016	LARP	Ligands ratio	436–489 nm	2–6	[49]
	MAPbBr ₃	2017	LARP	Ligands ratio	447–514 nm	3–8	[91]
	MAPbBr ₃	2017	LARP	Temperature	445–508 nm	3–9	[48]
	MAPbBr ₃	2018	LARP	Precursors ratio	396–490 nm	1–5	[41]
	MAPbBr ₃	2018	LARP	Ligands ratio	452–501 nm	–	[92]
	MAPbBr ₃	2019	LARP	Precursors ratio (LX:BX ₂ :AX) and ligands composition	405–440 nm (aprox)	1–2	[39]
	MAPbI ₃	2016	Exfoliation	Thickness-selective centrifugation	539–610 nm	1–3	[71]
	MAPbI ₃	2016	LARP	Precursors ratio (LX:BX ₂ :AX)	512–573 nm	1–2	[25]
	MAPbI ₃	2016	LARP	Precursors ratio	527–652 nm [RP] ^{a)}	1 – 4	[43]
	MAPbI ₃	2017	LARP	Ligands ratio	549–722 nm	–	[91]
	MAPbI ₃	2017	LARP	Precursors ratio	516–677 nm [RP] ^{a)}	1–5	[45]
	MAPbI ₃	2019	LARP	Precursors ratio (LX:BX ₂ :AX) and ligands composition	510–575 nm	1–2	[39]
	MAPbI ₃	2020	LARP	Ligands composition and ratio	510–650 nm	1–4	[44]
	MAPbI ₃	2020	LARP	–	579 nm [RP] ^{a)}	2	[50]
FAPbX ₃ perovskite nanoplatelets	FAPbBr ₃	2016	LARP	Precursors ratio (LX:BX ₂ :AX)	398–439 nm	1–2	[25]

Table 2. Continued.

Thickness-controlled synthetic strategies							
	Composition	Year	Synthesis method	Tunability strategy	Range (PL)	Range (ML)	Refs.
	FAPbBr ₃	2017	LARP	Ligands ratio	438–530 nm	2–NCs	[63]
	FAPbBr ₃	2017	LARP	Ligands ratio	438–533 nm	2–NCs	[93]
	FAPbBr ₃	2018	Microfluidic synthesis	–	432 nm	2	[94]
	FAPbBr ₃	2018	LARP	Ion-exchange-mediated self-assembly	398–490 nm	1–4	[55]
	FAPbBr ₃	2019	LARP	Ligands ratio	440–532 nm	2–8	[95]
	FAPbBr ₃	2019	LARP	Precursors ratio (LX:BX ₂ :AX) and ligands composition	405–440 nm (aprox)	1–2	[39]
	FAPbBr ₃	2020	LARP	–	440 nm	2	[96]
	FAPbBr ₃	2021	Hot Injection	–	440 nm	2	[97]
	FAPbI ₃	2016	LARP	Precursors ratio (LX:BX ₂ :AX)	512–575 nm	1–2	[25]
	FAPbI ₃	2017	LARP	Ligands ratio	668–737 nm	–	[63]
	FAPbI ₃	2017	Hot injection	–	580 nm	2	[52]
	FAPbI ₃	2019	LARP	Precursors ratio (LX:BX ₂ :AX) and ligands composition	510–575 nm	1–2	[39]
	FAPbI ₃	2020	LARP	–	582 nm [RP] ^{a)}	2	[50]
Lead-free perovskite nanoplatelets	Cs ₂ AgBiBr ₆	2018	Hot injection	–	426–465 nm	–	[98]
	Cs ₂ AgBiBr ₆	2021	Hot injection	–	630 nm	–	[99]
	Cs ₂ AgBiBr ₆	2021	Low-temperature injection + heating-up	Heating-up temperature	475–650 nm	1, 3, 4	[100]
	Cs ₂ AgBiI ₆	2018	Hot injection	–	610–680 nm	–	[98]
	CsSnI ₃	2018	Hot injection	–	780 nm	–	[101]
	Cs ₃ Sb ₂ I ₉	2017	Hot injection	–	575 nm	–	[102]
	FASnI ₃	2016	LARP	Precursors ratio (LX:BX ₂ :AX)	628–689 nm	1–2	[25]

Levchuk et al. demonstrated the preparation of highly luminescent MAPbX₃ (X = Br and I) NPLs by the LARP approach using OLA and OA ligands.^[91] It is important to use the proper ratio of acetonitrile and toluene mixture for washing MAPbBr₃ NPLs without degradation. They found that the thickness of NPLs decreases with increasing the ratio of OLA/OA. Moreover, it was found that the PLQY of NPLs decreases with decreasing their thickness. The lateral size of the NPLs prepared in this approach is generally much smaller compared to the NPLs obtained using alkylammonium cation ligands, and therefore they exhibited higher PLQY.^[28,91] The NPLs tend to form bookshelf-like side-by-side stacks on the TEM grid, which enables accurate thickness determination.

In general, because of their ionic nature, lead-halide perovskites crystallize easily into NCs in the presence of alkylammonium or alkylamine ligands, however, this could also be a problem for their stability. Tong et al. found that the bulk-like hybrid perovskite NPLs transform into quantum-confined NPLs upon the dilution of their colloidal solution in the presence of excess ligands.^[32] They observed a gradual blue-shift in the PL of the solution with an increase in the dilution factor, indicating the decrease in the thickness of NPLs with increasing dilution. Besides, the extent of the blue-shift strongly depended on the excess ligands present in the colloidal NPL solution. The authors proposed that the fragmentation of NPLs into thinner NPLs was due to osmotic swelling induced upon dilution. The addition

of solvent leads to the desorption of surface ligands and fragmentation of thicker NPLs, while the excess organic ligands in the solvent quickly passivate the newly formed surfaces, stabilizing the thinner NPLs in the process.^[32] Interestingly, the newly formed colloidal NPLs and their thin films were found to be stable under continuous UV light illumination. Time-resolved PL measurements show that the PL decay becomes faster with decreasing NPL thickness due to an increase in the radiative decay rate for thinner NPLs, which is likely due to an increase in the exciton binding energy with decreasing NPL thickness.^[32] The transformation of bulk perovskites into thin NPLs can also be achieved by ligand-assisted ultrasonication, as demonstrated by Hintermayr et al. (Figure 2c).^[71] Tip-sonication of bulk perovskite crystals in the presence of oleylamine gives a mixture of NPLs of different thicknesses, which can be separated into NPLs of individual thicknesses by ultracentrifugation at different speeds. Figure 5a presents the UV light illuminated colloidal dispersions of MAPbI₃ NPLs of different thicknesses ($n = 1, 2, 3, >3$ and ∞) prepared by ultrasonication of bulk MAPbI₃. As it is shown, the emission color is tunable from green to near IR by their thickness. The TEM images show that the NPLs obtained by this approach are rather polydisperse in their dimensions (Figure 5b). The PL spectra of NPLs obtained by ultracentrifugation at different speeds exhibit narrow emission for $n = 1–3$, while it is difficult to separate the thicknesses ($n > 3$ MLs) (Figure 5c). The time-resolved PL studies revealed

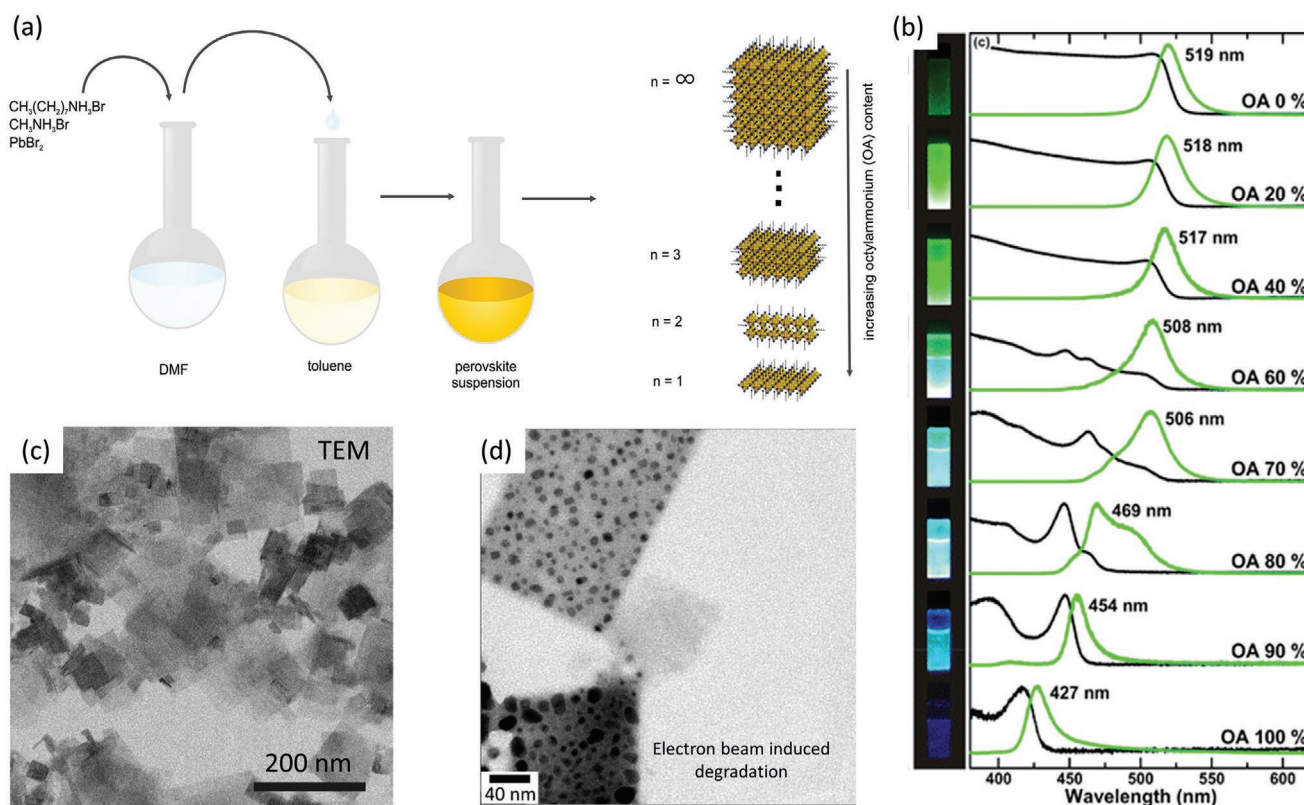


Figure 3. a) Schematic illustration of the synthesis of the MAPbBr₃ perovskite NPLs by antisolvent-induced reprecipitation. The thickness of the NPLs is tunable by varying the content of ratio octylammonium bromide (OABr) with respect to methylammonium bromide (MABr). b) Absorption (black line) and PL (green line) spectra of perovskite nanocrystal films prepared from colloidal suspensions obtained by varying the ratio of OABr/MABr (right panel) and photographs of the corresponding colloidal solutions under UV light (left panel) (in the figure OA refers to OABr). c) TEM and SEM images of MAPbBr₃ perovskite NPLs obtained with 80% OABr. d) TEM image of NPLs showing the electron beam-induced evolution of spherical Pb particles. Reproduced with permission.^[28] Copyright 2015, American Chemical Society.

that the decay becomes faster with decreasing the NPL thickness (Figure 5d). Interestingly, the decay profile changes from bimolecular to monomolecular with decreasing NPL thickness, likely due to the excitonic nature of 2D perovskites. In 3D MAPbI₃ perovskites, the decay is bimolecular due to the formation of free carriers at room temperature owing to their low exciton binding energy. However, for thinner NPLs, it is less likely to form free carriers due to higher exciton binding energy than thermal energy, thus leading to exciton recombination, which is a monomolecular process.

Although the synthesis and optical properties of MAPbX₃ perovskite NPLs have been thoroughly explored, FAPbX₃ NPLs, an important hybrid perovskite system, have been less investigated. To the best of our knowledge, thickness-dependent PL peaks for FAPbX₃ NPLs are not well documented in the literature. In principle, the synthesis methodologies developed for MA perovskite NPLs could also be extended to FA perovskite NPLs. For instance, Levchuk et al. reported the synthesis of thickness-tunable FAPbBr₃ NPLs by the LARP approach initially used for MAPbX₃ NPLs (Figure 6a).^[63] The thickness of NPLs is controllable by varying the ratio of OLA/OA ligands in the precursor solution. The gradual increase in the OLA content leads to a decrease in the NPL thickness and thus a gradual blue-shift of the PL peak (Figure 6a-i). In addition, it was found that the PLQY of NPLs decreases with decreasing thickness (Figure 6a-ii),^[63] which is likely due to an

increase in the density of deep traps as the bandgap increases (refer to the surface passivation section for more details). The lateral dimensions of the NPLs are in the same range as the MAPbX₃ NPLs prepared by the same LARP approach.^[63,91] Figure 6a-iii presents the theoretical and experimental PL peak positions for FAPbBr₃ NPLs of different thicknesses and they match quite well. The peaks at 438, 486, 533 nm were assigned to *n* = 2, 3, and 4, respectively. However, this needs further in-depth investigation because the PL peak for *n* = 4 is already very near to its bulk, and this is very different from MAPbBr₃ system (see Table 1). The LARP approach, but using octylamine instead of OLA, also give rise NPLs of different thicknesses with tunable from green to blue range.^[95] However, in contrast to the OLA-case, the thickness of NPLs increases with increasing octylamine content in the precursor solution. Furthermore, Zhang et al. demonstrated that the use of short alkylamines during synthesis results in micron-sized *n* = 2 R-P. FAPbBr₃ NPLs.^[108] Despite great successes in the synthesis of hybrid perovskite NPLs by the conventional LARP approach, the DMF used for precursors can affect the stability of the NPLs. To overcome this, Huang et al. modified the LARP approach in which no DMF is required for the dissolution of precursor salts (Figure 6b-i).^[56] The introduction of Cs-oleate complex into toluene containing PbX₂-ligand complex leads to the formation of perovskite NPLs. The FAPbI₃ NPLs prepared using this approach exhibit near-monodispersity, and they tend

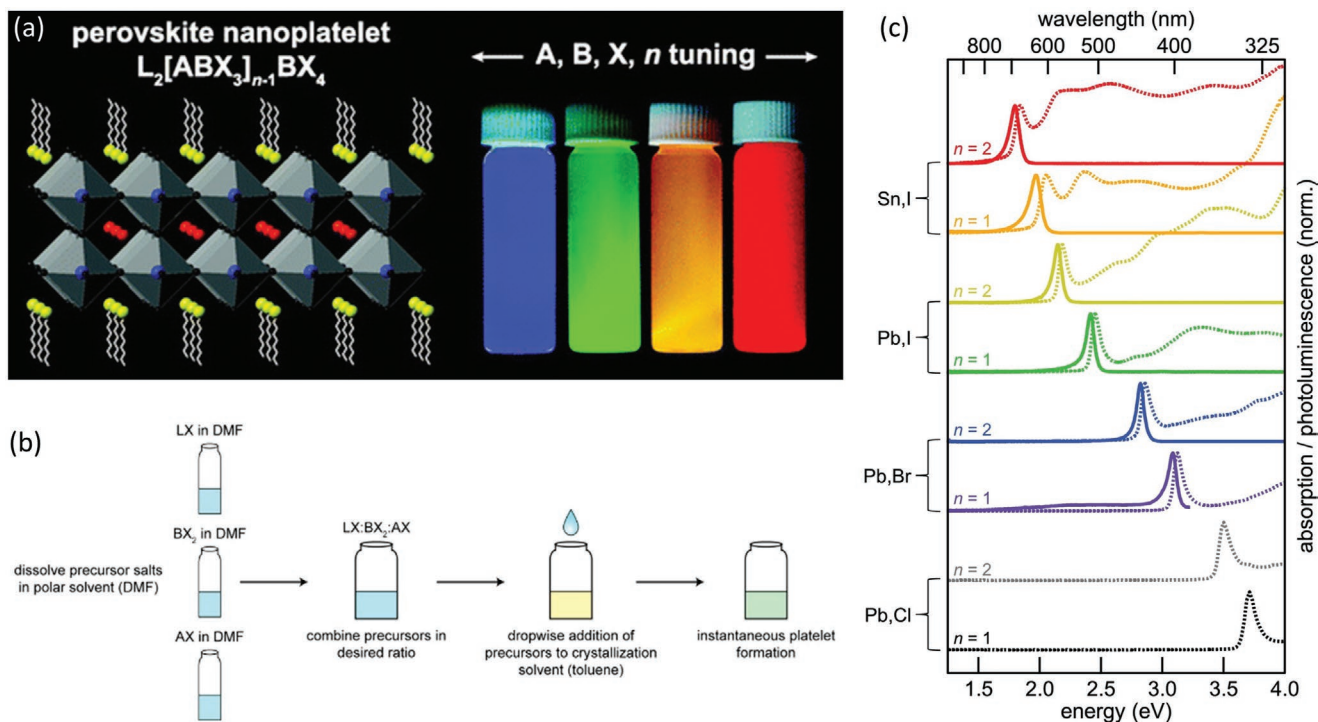


Figure 4. a) Schematic of perovskite NPLs structure and their tunable emission color across the visible range by composition (A, B, and X) and thickness (n). b) Schematic of the steps involved in the LARP approach for the synthesis of hybrid perovskite NPLs. c) Absorption (dotted lines) and PL (solid lines) spectra for $n = 1$ and $n = 2$ FA perovskite nanoplatelets of different B (Pb and Sn) and X (Cl, Br, and I) compositions. Reproduced with permission.^[25] Copyright 2016, American Chemical Society.

to form stacks upon solvent drying (Figure 6b-ii). In this method, the thickness of the NPLs is tunable by controlling the ratio of monovalent (MA^+ or FA^+) to divalent (Pb^{2+}) cation–ligand com-

plexes. Very recently, Patra et al. demonstrated the synthesis of monodisperse $n = 2$ stacked NPLs by hot-injection approach using oleylammonium cation ligand (Figure 6c).^[97]

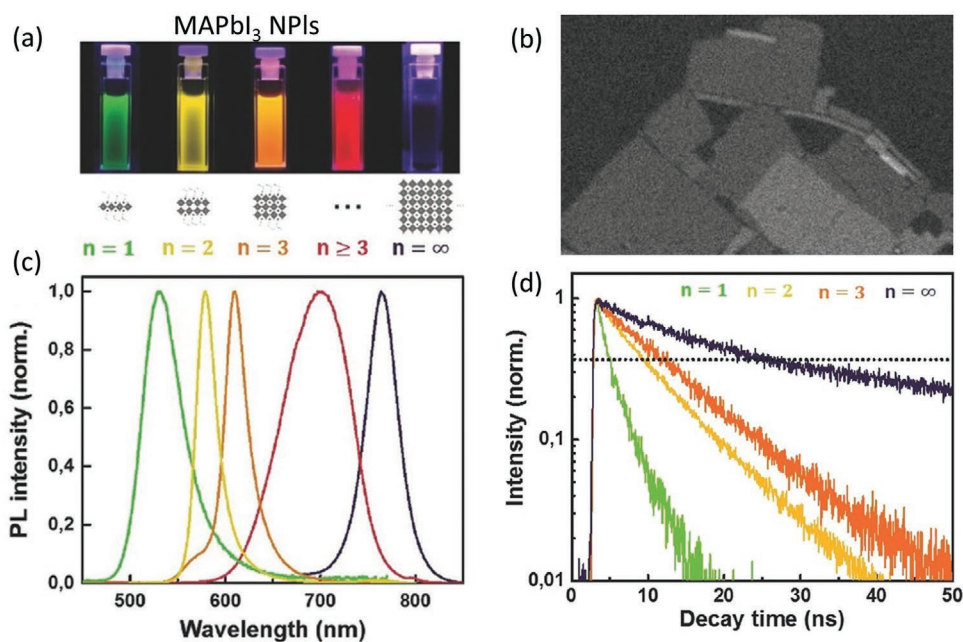


Figure 5. a) Colloidal solutions of MAPbI₃ NPLs of different thicknesses under UV light illumination. b) HAAD-STEM image of MAPbI₃ NPLs obtained by ligand ultrasonication of bulk perovskites. c,d) Corresponding PL spectra and time-resolved PL lifetime of MAPbI₃ NPLs of different thicknesses. Reproduced with permission.^[71] Copyright 2016, John Wiley & Sons.

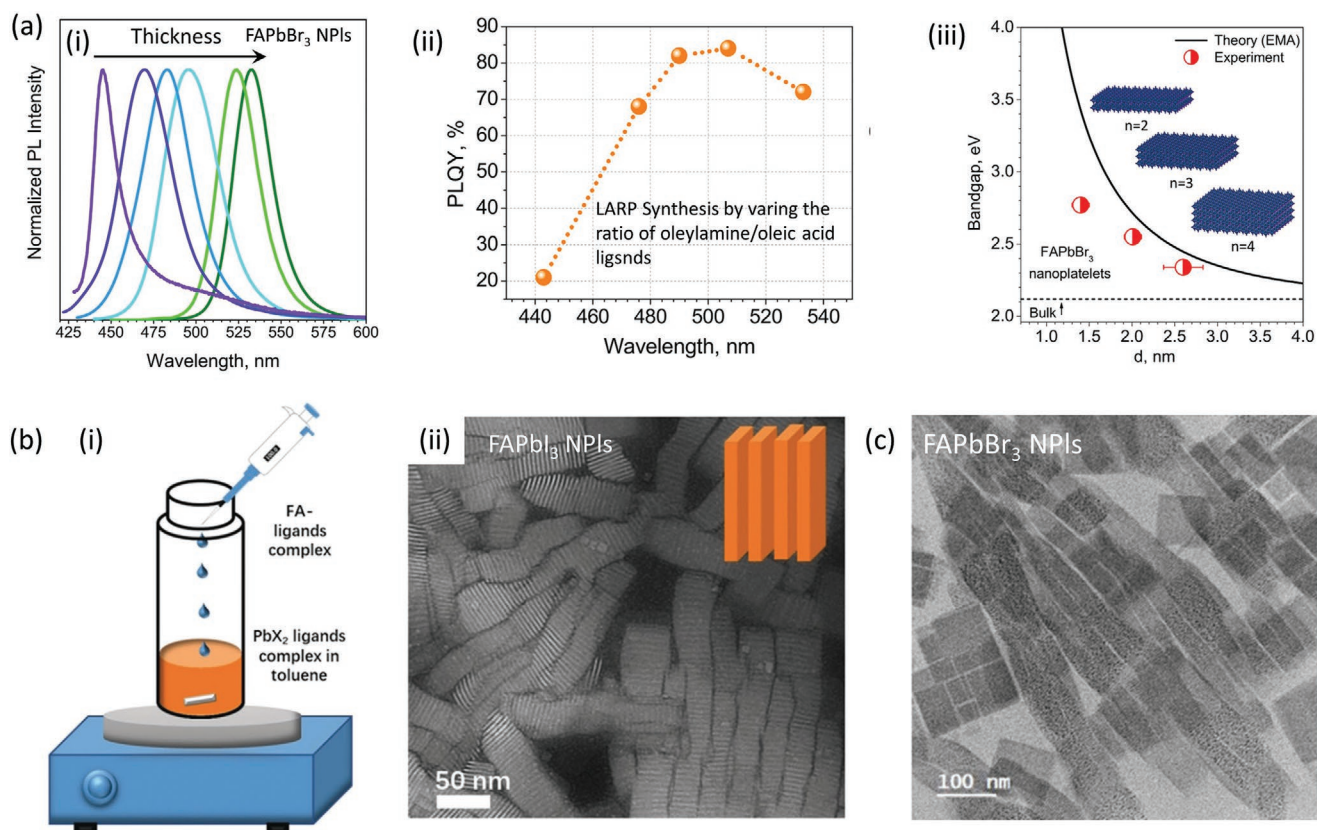


Figure 6. a-i) PL spectra for colloidal FAPbBr₃ NPLs of different thicknesses prepared by LARP approach using different ratios of OLA/OA ligands. The thickness of NPLs decreases with an increase in OLA concentration, and thus results in a blue-shift of PL peak. a-ii) PLQY of FAPbBr₃ NPLs of different thicknesses. The PLQY decreases with decreasing the NPL thickness. a-iii) Experimental and theoretical bandgaps versus thickness of FAPbBr₃ NPLs. Reproduced with permission.^[63] Copyright 2017, American Chemical Society. b) Spontaneous crystallization of ABX₃ perovskite NPLs upon the addition of A-ligand complex to BX₂-ligand complex in toluene (i) and the TEM image of FAPbI₃ NPLs prepared by this approach (ii). Reproduced with permission.^[56] Copyright 2019, John Wiley & Sons. c) TEM image of blue-emitting FAPbBr₃ NPLs prepared using oleylammonium bromide ligands. Reproduced with permission.^[97] Copyright 2021, American Chemical Society.

2.3. Synthesis of Inorganic Perovskite Nanoplatelets

There has been tremendous progress in the synthesis of inorganic halide perovskite NPLs, especially CsPbBr₃ NPLs, compared to hybrid perovskites regarding their thickness control, monodispersity and understanding their properties.^[14,29–31,33,47,53,59,74,75,84,109–114] Around the beginning of 2016, the groups of Alivisatos and Manna simultaneously reported the thickness-controlled synthesis of CsPbX₃ NPLs.^[30,31] Alivisatos' group first reported the formation of CsPbBr₃ NPLs by decreasing the reaction temperature (<140 °C) in the hot injection method initially developed for CsPbX₃ nanocubes by Protesescu et al.^[16] and the thickness of NPLs gradually decreased with decreasing reaction temperature (Figure 7a).^[31] The change in morphology is easily noticeable by the emission color of the resulting colloidal solution. In general, CsPbBr₃ nanocubes exhibit green emission (unless they are strongly quantum-confined under specific synthetic conditions), while the NPLs emit colors ranging from blue to violet depending on their thickness. It is worth mentioning that NPLs can emit green color if the thickness is greater than 5–6 nm for CsPbBr₃. It is critical to purify the product using a mixture of ethyl acetate and methyl-ethyl ketone to obtain highly luminescent CPbBr₃ NPLs, while

the use of common antisolvent mixtures such as methanol/acetone can significantly quench their PLQY and influence their chemical stability. By applying suitable purification steps, they were able to obtain and characterize CsPbBr₃ NPLs of different thicknesses ($n = 1, 2, 3, 4, 5$, and ∞ , n references to the thickness in terms of number of MLs) (Figure 7b). As shown in Figure 7b, the NPLs exhibit sharp excitonic features because of greater confinement of excitons as compared with nanocubes, and the emission wavelength blue-shifts as the NPLs get thinner. The emission color of CsPbBr₃ NPLs is tunable over the range of 400–510 nm by only varying their thickness, without changing their halide composition. The CsPbBr₃ NPLs can be transformed into CsPbI₃ NPLs through anion exchange, and thus their emission properties move to the region of ≈530–700 nm wavelength. Overall, the emission color of perovskite NPLs is tunable across the entire visible range only with pure CsPbBr₃ and CsPbI₃ compositions by controlling their thickness.^[31] Manna's group reported the LARP approach for the synthesis of CsPbBr₃ NPLs at room temperature using acetone as an antisolvent.^[30] They were able to tune the thickness of NPLs from 3 to 5 MLs with monolayer precision by controlling the amount of HBr added to the reaction medium and compared their optical properties with nanocubes and bulk thin films (Figure 7c-i).^[30]

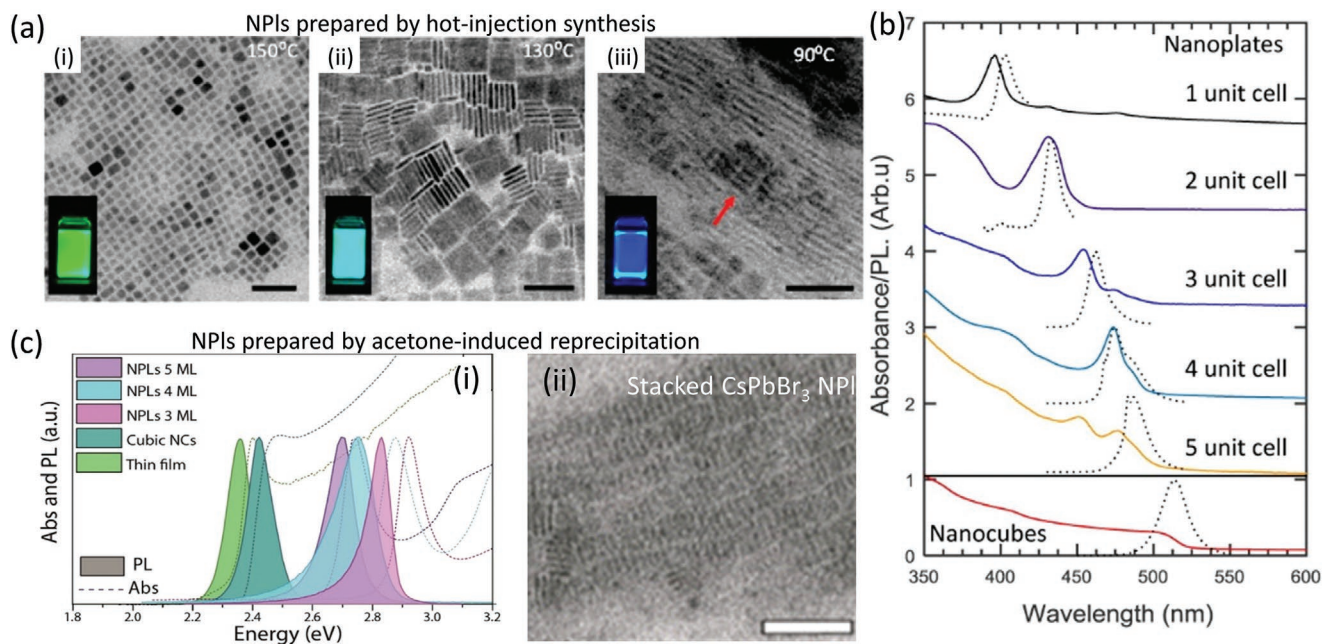


Figure 7. a) TEM images of CsPbBr₃ NCs prepared by hot-injection synthesis at different reaction temperatures (150 °C (i), 130 °C (ii), and 90 °C (iii)). b) Absorption (solid lines) and PL (dotted lines) spectra of nanocubes and NPLs of 5 different thicknesses (1–5 unit cells). a, b) Reproduced with permission.^[31] Copyright 2015, American Chemical Society. c) Absorption (dotted line) and PL (solid line) spectra for thin film, colloidal cubic NCs (green) and colloidal NPL of different thickness ($n = 3, 4,$ and 5) CsPbBr₃ perovskite (i), and TEM image of CsPbBr₃ NPLs prepared by acetone-induced reprecipitation (ii). Reproduced with permission.^[30] Copyright 2016, American Chemical Society.

The CsPbBr₃ NPLs exhibit excellent monodispersity regarding their thickness and often tend to form vertically aligned side-by-side stacks on the TEM grid (Figure 7c-ii). Such self-assembled stacked-NPLs transform into nanowires under high-power UV-light illumination.^[115] They proposed that the increase of HBr concentration promotes the protonation of OLA, leading to the formation of oleylammonium cations that compete with Cs⁺ for lattice sites and promotes the formation of layered structures. Therefore, the increase in HBr concentration leads to a decrease in NPL thickness. This is similar to the growth mechanism proposed for hybrid perovskite NPLs, in which the increase in the concentration of long-chain ammonium cation leads to a decrease in their thickness.^[28] As shown in Figure 7c-i, the nanocubes exhibit blue-shifted emission compared to bulk thin films, while the PL emission further shifts toward the higher energy side as the morphology changes from nanocubes to NPLs. In addition, one can clearly see the sharp excitonic features in the absorption spectra of NPLs due to strong quantum confinement effects.

The LARP approach for CsPbBr₃ NPLs was further modified by Tong et al.^[29] to make it easier, DMF-free and to achieve excellent thickness control from $n = 2$ to 6 with monolayer precision (Figure 8). In their approach, acetone induces the precipitation of precursors into perovskites in the presence of OLA and OA ligands (Figure 8a). It is worth mentioning washing with acetone induces defects on the surface of NPLs, which then requires postsynthetic surface passivation to obtain highly luminescent NPLs. Later, they found that the precursors, under specific concentrations, spontaneously crystallize into perovskite NPLs in nonpolar solvents without the addition of acetone.^[56] They demonstrated that the thickness of the NPLs

is tunable by varying the ratio between Cs⁺ to Pb²⁺ precursors.^[29,56] As shown in Figure 8c, the decrease in the ratio Cs/Pb results in blue-emissive colloidal NCs, suggesting the formation of CsPbBr₃ NPLs. The TEM images of the corresponding colloidal solutions revealed that the thickness of NPLs decreases with decreasing the Cs/Pb ratio (Figure 8d–f). The decrease in Cs⁺ content leads to an obvious increase in the ratio of ligand to Cs⁺, and this is somewhat similar to the increase of long-chain ammonium cation (ligand) to methylammonium (MA⁺) cation, which leads to a decrease in the thickness of hybrid perovskite NPL.^[116] The NPLs prepared by this approach exhibit narrow and single PL peaks, suggesting that the colloidal solutions consist of NPLs with a single thickness (Figure 8g). In addition, it was found that the exciton binding energy for $n = 2$ NPLs is an order of magnitude higher than that of nanocubes.^[29]

Like the synthesis of hybrid perovskites, the concentration of the acid-base ligand pair (OLA-OA) plays an important role in the morphology of the resultant inorganic perovskite NCs.^[33,74] For example, Almeida et al. found that the increase in the concentration of OA during hot injection leads to the formation of pure CsPbBr₃ NPLs.^[33] They proposed that the increase in the ratio of oleylammonium to Cs⁺ cations leading to the anisotropic growth by preventing the growth in certain facets. However, it is still unclear on the symmetry breaking and facet selective growth of NPLs in the presence of excess oleylammonium cation, otherwise leading to isotropic nanocubes. Furthermore, they demonstrated the synthesis of monolayer perovskites by completing eliminating Cs⁺ ions in the reaction medium.

Apart from reaction temperature and ligand concentration, the chain length of ligands, type of solvent, and any additional metal ions in the precursor solution all significantly influence

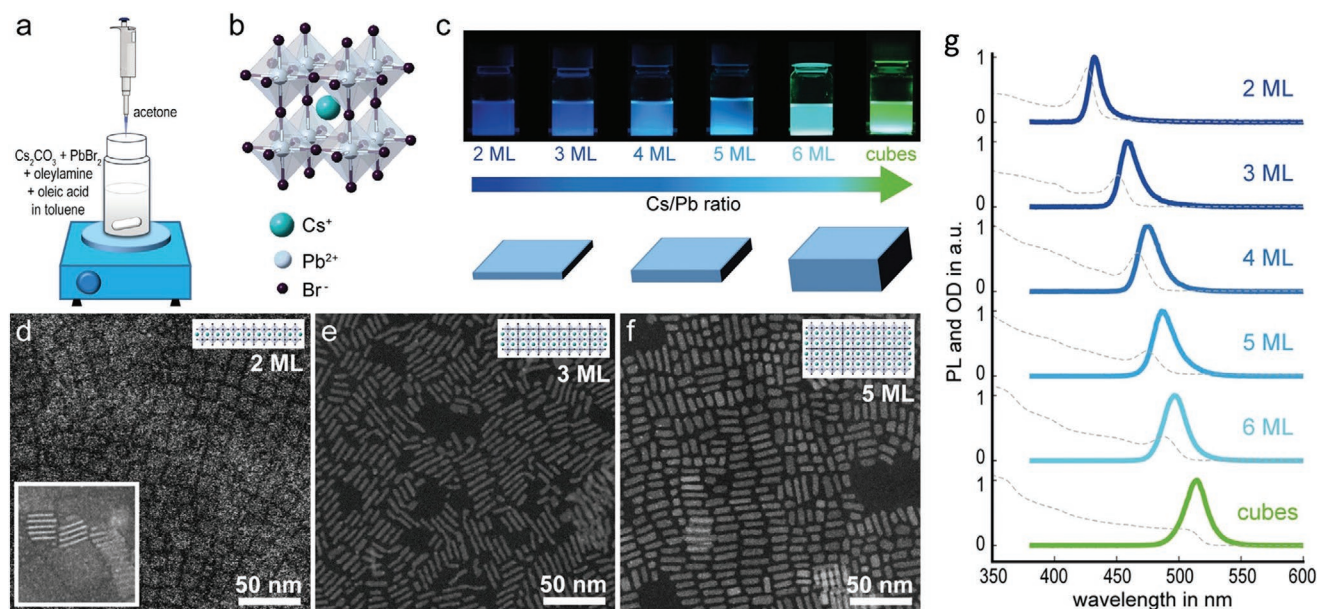


Figure 8. a) Schematic illustration for the synthesis of thickness-controllable CsPbBr₃ NPLs. b) Cubic crystal structure of perovskite NCs. c) Colloidal solutions of CsPbBr₃ NPLs of different thicknesses under UV light illumination. The thickness of the NPLs decreases with decreasing the Cs/Pb ratio in the precursors. d–f) HAAD-STEM images of 2 ML, 3 ML and 5 ML CsPbBr₃ NPLs. The inset in d is the HAAD-STEM image of vertically stacked NPLs enabling the thickness determination. g) Absorption (dotted line) and PL (solid line) spectra of CsPbBr₃ nanocubes and NPLs of different thicknesses (2–6 ML). Reproduced with permission.^[29] Copyright 2018, American Chemical Society.

the size and shape of halide perovskite NCs.^[14,47,75,83] Pan et al. found that the use of short-chain amine ligands in hot-injection synthesis yields NPLs under both high and low reaction temperatures, while the use of short-chain carboxylic acids yields larger nanocubes.^[75] The NMR and IR studies on purified perovskite NCs revealed the presence of both alkylammonium and carboxylate. It was also proposed that the ammonium cation binds to the NC surface while the carboxylic acid neutralizes the charge.^[15] Recently, a similar growth mechanism was proposed by Bonato et al. for the formation of CsPbX₃ NPLs assisted by the presence of Sn⁴⁺ cations.^[47] They proposed that the Sn⁴⁺ (Lewis acid) promotes the protonation rate of OLA by affecting the acid–base equilibrium of the reaction system and thus the oleylammonium cations help the anisotropic growth of NPLs. Despite decent progress in the thickness-controlled synthesis of CsPbBr₃ NCs, the exact surface chemistry and the atomic crystal structure is still unclear and a more in-depth study is required. In this regard, Bertolotti et al. investigated the crystal structure and surface chemistry of 6 ML-thick CsPbBr₃ NPLs by combining atomically resolved electron microscopy with synchrotron X-ray scattering measurements (Figure 9).^[59] The 6 ML-thick NPLs were synthesized by the hot-injection method at 130 °C and using two-fold concentrated precursors compared to those in nanocube synthesis. As shown in Figure 9a, the NPLs exhibit excellent monodispersity with an average thickness of 3.5 nm and cyan emission ($\lambda_{\text{max}} = 492$ nm). High-resolution TEM (HRTEM) characterization of the NPLs reveals their single-crystalline nature, with a lattice spacing of 5.8 Å. This lattice spacing (or d-spacing) represents both the cubic cell axial lengths as well as Pb–Pb distances in the orthorhombic structure, as illustrated in Figure 9c,d. Therefore, one cannot determine the exact crystal structure from the

d-spacing obtained from the HRTEM image, however, it gives an important input for first-principles calculations. In addition, the octahedral tilting in the orthorhombic structure (Figure 9d) is below the general resolution limit of HRTEM, meaning it is difficult to differentiate the cubic and orthorhombic phases by HRTEM images. The geometrical relationship between the cubic (a_k) and orthorhombic (a_{orth} , b_{orth} , and c_{orth}) unit cell axes and the pseudocubic versus orthorhombic faces are illustrated in Figure 9e, and this was used for the analysis of X-ray data obtained from synchrotron measurements (see ref. [59] for more details). The conventional XRD measurements performed on NPL films and the synchrotron wide-angle total scattering experiments on colloidal suspensions suggest that they exhibit an orthorhombic structure, very similar to that of conventional nanocubes.^[59] A recent study by Manna's group suggests that 2 ML thick NPLs also adapt orthorhombic crystal structure.^[104] Furthermore, it was proposed that the NPL surface terminates with CsBr with half of the Br and Cs positions vacant.^[59] These vacancies can significantly hamper the optical properties of NPLs, however, they can be repaired (or passivated) by different ways to recover their properties, as discussed in the following section.^[15]

2.4. Synthesis of Doped and Surface Treated Halide Perovskite Nanoplatelets

2.4.1. Surface Passivated Halide Perovskite Nanoplatelets

Despite significant progress in the thickness-controlled synthesis with monolayer precision, pristine perovskite NPLs usually suffer from low PLQY and colloidal instability as compared

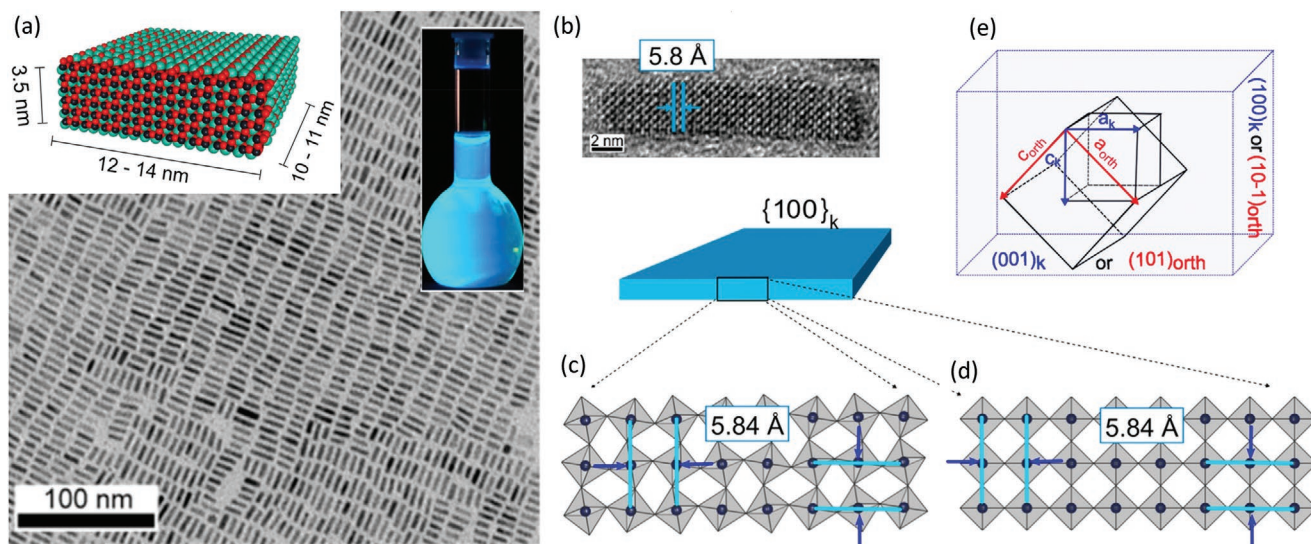


Figure 9. a) TEM image of 6 ML-thick CsPbBr₃ NPLs. The insets are the schematic illustration of the NPL (left) and the colloidal solution emitting cyan-blue under UV-light irradiation. b) HRTEM image of the 6 ML thick CsPbBr₃ NPLs with a lattice constant of 5.8 Å. Schematic illustration of 3 ML-thick CsPbBr₃ NPLs in the c) orthorhombic and d) cubic arrangements. In both arrangements, the lattice constant is expected to be 5.8 Å. e) Schematic illustration showing the geometrical relationship between the cubic (a_k) and orthorhombic (a_{orth} , b_{orth} , and c_{orth}) unit cell axes and the pseudocubic and orthorhombic faces. Reproduced with permission.^[59] Copyright 2019, American Chemical Society.

with nanocubes.^[9,14,72,105] Although near-unity PLQY is easily achievable for perovskite nanocubes under optimized conditions,^[118–120] it has been often observed that the PL efficiency decreases for NPLs with decreasing thickness and therefore wide bandgaps.^[28,29,71] In principle, 2D NPLs are expected to exhibit high PLQY due to the enhanced radiative recombination caused by the confinement of charge carriers. However, the high density of surface defects caused by the high surface-to-volume ratio of NPLs results in their low PLQY. The surface defects in lead halide perovskites are generally related to the X and Pb vacancies, as well as the A-site vacancies caused by the detachment of ligands during the purification process (Figure 10a,c,d). In principle, filling these vacancies can significantly suppress the nonradiative recombination of charge carriers and thus enhance the PL efficiency of NCs. The passivation methods initially developed for perovskite nanocubes to achieve near-unity PLQY has been extended to NPLs to increase their PLQY.^[15,29,53,119,121] These methods include in situ passivation during synthesis or post-synthetic passivation of surface vacancies (Figure 10a,c,d).^[15,29,53,117,122,123] For instance, Bohn et al. demonstrated a drastic improvement in the PL of CsPbBr₃ NPLs by post-synthetic treatment with a solution consisting of metal halides complexed with OLA and OA ligands (Figure 10a,b).^[29] After comparing several metal halides, they found that the maximum PL enhancement was obtained with PbBr₂-ligand, suggesting that both the Pb and Br vacancies are responsible for the lower PLQY of CsPbBr₃ NPLs. In addition, the post-synthetic treatment of NPL of different thickness with PbBr₂ shows that the PLQY enhancement factor increases as the thickness of the NPLs decrease (Figure 10b).^[29] This suggests that the density of halide vacancies increases with decreasing NPL thickness because of the increased surface area-to-volume ratio. The refilling of vacancies and recovery of PLQY lead to an increase in the PL lifetime due to the removal

of the trap-mediated nonradiative channel. Thus the PL decay of the passivated NPLs became monoexponential, whereas the nonpassivated NPLs had a nonmonoexponential decay.^[29] In a similar work, Wu et al. reported an in situ passivation method for PbBr₆⁴⁻ octahedra at the nucleation stage introducing excess Br⁻ in the reaction medium to obtain trap-free CsPbBr₃ NPLs with near-unity PLQY (Figure 10c).^[53] Additionally, they demonstrated the fabrication of CsPbBr₃ NPL-based blue LEDs with an external quantum efficiency (EQE) of 0.124% and an emission line width of ≈ 12 nm.^[53] Very recently, Lin et al.^[117] reported a similar in situ passivation strategy by introducing potassium oleate and excess PbBr₂ in the reaction medium to obtain CsPbBr₃ NPLs with a PLQY of 87% (Figure 10d). They proposed that potassium bromide (KBr) passivates the Br vacancies on the NPL surface and thus improves photo and thermal stabilities by suppressing halide ion migration. Besides metal halides, ligand molecules could also be used for in situ passivation of perovskite NPLs. For instance, Huang et al. reported the preparation of CsPbBr₃ NPLs with near-unity PLQY by in situ passivation using (3-aminopropyl)triethoxysilane (APTES) ligand, which also acts as a cross-linker.^[122] The resulting NPLs exhibited greater stability in polar solvents, such as water and DMF. This study suggests that APTES could be a potential ligand for solving the stability problems associated with perovskite NCs. However, it is important to study the effect of the ligand on the inter-particle charge transfer properties before using these materials in optoelectronic devices.

2.4.2. Metal Ion-Doped Halide Perovskite Nanoplatelets

Besides passivation, metal cation doping into perovskite NC lattices has been greatly exploited to induce new optical features and properties, as well as to improve their stability.^[14,124–126]

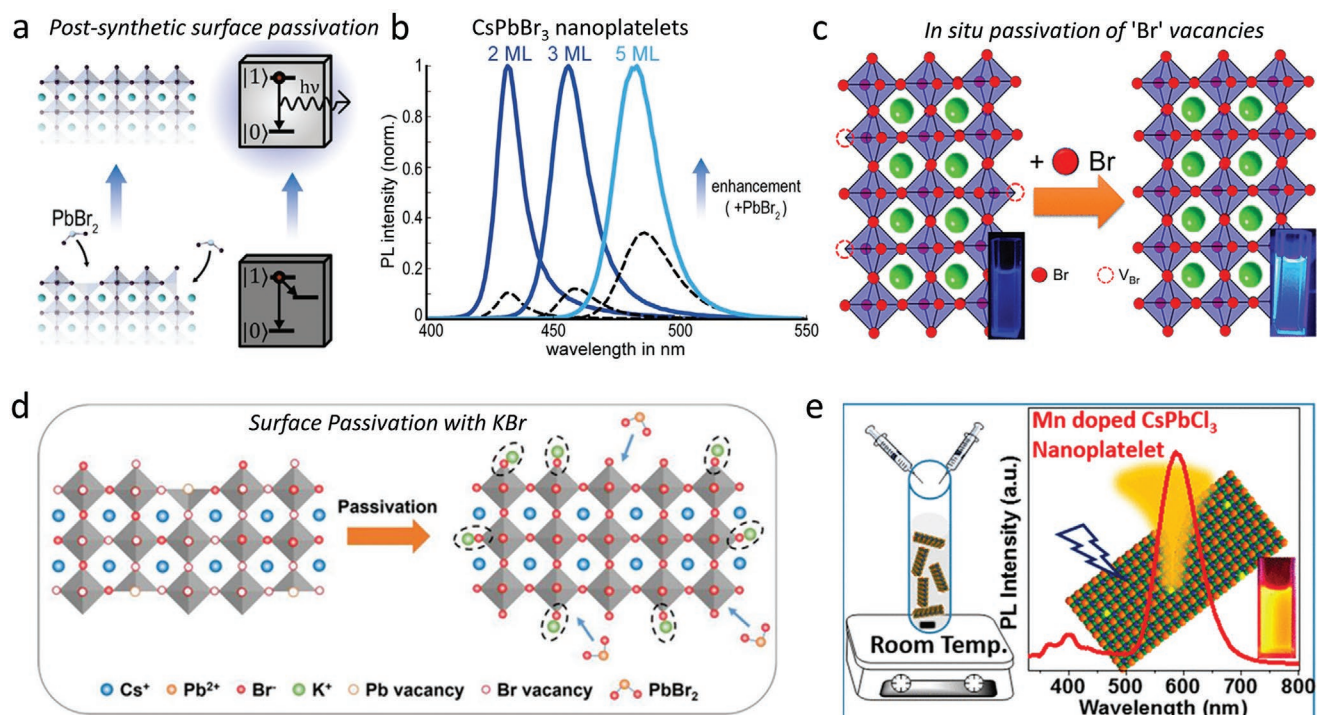


Figure 10. a) Schematic illustration showing the passivation of Br and Pb vacancies on perovskite NC surface by treatment with PbBr_2 -ligand solution. b) PL spectra of pristine and PbBr_2 treated CsPbBr_3 NPLs of different thicknesses. The spectra are normalized to compare the magnitude of the enhancement in the three samples. Reproduced with permission.^[29] Copyright 2018, American Chemical Society. c) Schematic illustration showing the in situ passivation of Br vacancies by addition of excess Br^- in the reaction medium to form intact PbBr_6^{4-} octahedra of CsPbBr_3 NPLs. Reproduced with permission.^[53] Copyright 2018, American Chemical Society. d) Schematic representation of the KBr-enriched passivation of CsPbBr_3 NPLs by K-oleate and excess PbBr_2 to the perovskite precursor solution. Reproduced with permission.^[17] Copyright 2021, John Wiley & Sons. e) Schematic illustration of the synthesis of Mn^{2+} -doped CsPbCl_3 NPLs by acetone induced reprecipitation (left), and the corresponding PL spectra showing yellow-orange emission (right). Reproduced with permission.^[10] Copyright 2017, American Chemical Society.

Among various metal ion dopants, Mn^{2+} has received special attention due to its interesting interactions with excitons of semiconductor hosts.^[14,127–129] It is well known that the semiconductor host efficiently transfers its excitonic energy to Mn^{2+} dopants, thus leading to an intense orange emission from a spin-forbidden ${}^4\text{T}_1\text{--}{}^6\text{A}_1$ Mn d–d transition.^[14,128] Mn^{2+} doping was first investigated in perovskite nanocubes^[130,131] and later extended to NPLs as well.^[110,132–137] Especially, Mn^{2+} -doped strongly quantum-confined NPLs are expected to exhibit interesting magneto-optical properties due to enhanced interactions between charge carriers with Mn^{2+} dopants caused by the confinement of charge carriers.^[138] The reported studies on Mn^{2+} -doped perovskite NCs with different halide compositions suggest that the high bandgap chloride-based perovskites are most suitable for efficient transfer of excitonic energy to Mn^{2+} dopants.^[130,131] Inspired by these early studies, Mir et al. first reported the synthesis of Mn^{2+} -doped CsPbCl_3 quasi-2D NPLs at room temperature by the acetone-induced reprecipitation approach (Figure 10e).^[110] The EPR spectra of doped NPLs strongly suggest that the Mn^{2+} dopants substitutionally occupy the Pb^{2+} sites in the perovskite crystal lattice. The prepared Mn^{2+} -doped CsPbCl_3 NPLs exhibit orange emission with 20% PLQY at 0.8% dopant concentration. However, the orange emission significantly decreased for Mn^{2+} -doped CsPbBr_3 NPLs obtained from Mn^{2+} -doped CsPbCl_3 NPLs by postsynthetic anion exchange reaction.

The PLQY of doped NPLs strongly depends on the concentration of the dopant in the host lattice. Several studies suggest that the PLQY increases with increasing Mn^{2+} dopant concentration up to some extent, while excess dopant concentration quenches the PL due to dopant annihilation. In theory, all the Pb^{2+} of perovskite lattice can be replaced with Mn^{2+} to obtain an AMnX_3 lattice. For example, Li et al. showed that the lateral size of the Mn^{2+} -doped CsPbCl_3 NPLs and the concentration of dopants increases by solvothermal treatment of pre-synthesized Mn^{2+} -doped small CsPbCl_3 NPLs.^[135] In their work, the Mn^{2+} -doped CsPbCl_3 NPLs were prepared by hot-injection synthesis, and the excitonic emission at 400 nm suggested that the NPLs were quite thick and exhibited bulk-like optical properties.^[135] They observed the formation of the CsMnCl_3 phase by X-ray diffraction and an increase of PLQY from 2% to 21% after the solvothermal treatment. Very recently, a PLQY of over 50% has been reported for Mn^{2+} -doped CsPbCl_3 NPLs prepared with an Mn-to-Pb feed ratio of 7:3, and their use as color converters in the fabrication of warm white LEDs was demonstrated.^[134] It might be difficult to have accurate control over the dopant concentration in the direct synthesis of doped NCs. Moreover, it is still unclear about the dopant sites in the perovskite lattice. Electron paramagnetic resonance studies on Mn^{2+} -doped CsPbCl_3 NPLs suggest the incorporation of dopants in the lattice. However, the amount of dopant in the semiconductor crystal lattice is relatively easily controllable through

post-synthesis cation exchange using the corresponding metal salt precursors.^[14] This approach has been used to dope Mn²⁺ ions into CsPbBr₃ NPLs by treating them with MnBr₂ precursors.^[132] Interestingly, although CsPbBr₃ nanocubes (size ≈ 10–12 nm) do not give orange emission after doping with Mn²⁺, strongly quantum-confined Mn²⁺-doped CsPbBr₃ NPLs produce intense orange emission. This suggests that the higher bandgap of 2D or quasi-2D CsPbBr₃ NPLs favors the transfer of exciton energy to the Mn²⁺ dopants. In fact, Son and co-workers initially observed this in CsPbBr₃ NPLs prepared by direct hot-injection synthesis.^[137] Recently, a study by Babu et al. suggested that both energy and charge transfer from the CsPbBr₃ NPLs to Mn²⁺ dopants results in the orange emission. Furthermore, an interesting feature of Mn²⁺-doped CsPbBr₃ NPLs is their PL peaks centered simultaneously in both the blue (excitonic emission) and orange (dopant emission) regions and could produce white light upon mixing them with green emissive CsPbBr₃ nanocubes. It is worth mentioning that it is not possible to achieve white emission by mixing Mn²⁺-doped CsPbCl₃ NPLs with CsPbBr₃ nanocubes due to spontaneous halide exchange. This emphasizes the advantages of using quantum confinement to tune the emission wavelength, by allowing blue (CsPbBr₃ NPLs), green (CsPbBr₃ nanocubes), and orange (Mn²⁺-doped CsPbBr₃ NPLs) emission to all be simultaneously achieved with the same perovskite composition that avoids halide exchange. Curiously, Zhao et al. were even able to observe white emission from Mn²⁺-doped CsPbBr₃ NPLs with a PLQY over 60% without the addition of green emissive CsPbBr₃ nanocubes.^[132] Surprisingly, they observed an additional PL peak at 500 nm upon treating NPLs with a higher amount of MnBr₂ precursor solution. In this case, the doped NPLs were

prepared by cation ion exchange using MnBr₂ precursor and this could produce some CsPbBr₃ nanocubes as a side product. We believe that this interesting system needs further in-depth investigation for a better understanding of the origin of white emission from the Mn²⁺-doped CsPbBr₃ NPLs.

2.5. Synthesis of Lead-Free Perovskite Nanoplatelets

Lead-free colloidal halide perovskite NCs have drawn wide attention as alternatives to lead-based counterparts.^[14,139–141] Significant efforts are being devoted to replacing Pb with other less toxic metal ions. Among all, Sn, Bi, and Sb are potential alternatives to Pb. Most reported studies on Pb-free perovskites have been focused on either the bulk material or nanocubes, while the synthesis of colloidal NPLs has been rarely reported because of the challenges associated with their poor stability. Tisdale's group initially extended the LARP approach to the synthesis of *n* = 1 and 2 tin-based (L₂[FASnI₃]_{*n*-1}SnI₄) hybrid perovskite NPLs (see **Figure 11** for synthesis method).^[25] The uniform NPLs were prepared by dissolving precursors (Li, SnX₂, and FAI) in DMF with a molar ratio of 2:1:0 or 10:2:1 for *n* = 1 or *n* = 2 NPLs, respectively. The NPLs were crystallized immediately after the addition of precursor solution into 10 mL toluene at room temperature. The peak absorption onset and emission energies for *n* = 1 and *n* = 2 NPLs are 2.05/1.97 and 1.83/1.80 eV, respectively (see Figure 4c). It is important to prepare all the precursors under inert conditions to obtain relatively stable Sn-based perovskite NPLs, otherwise, they immediately turn into non-emissive materials. Yang's group demonstrated the synthesis of stable CsSnI₃ NPLs (4–5 ML thick) under Sn-rich

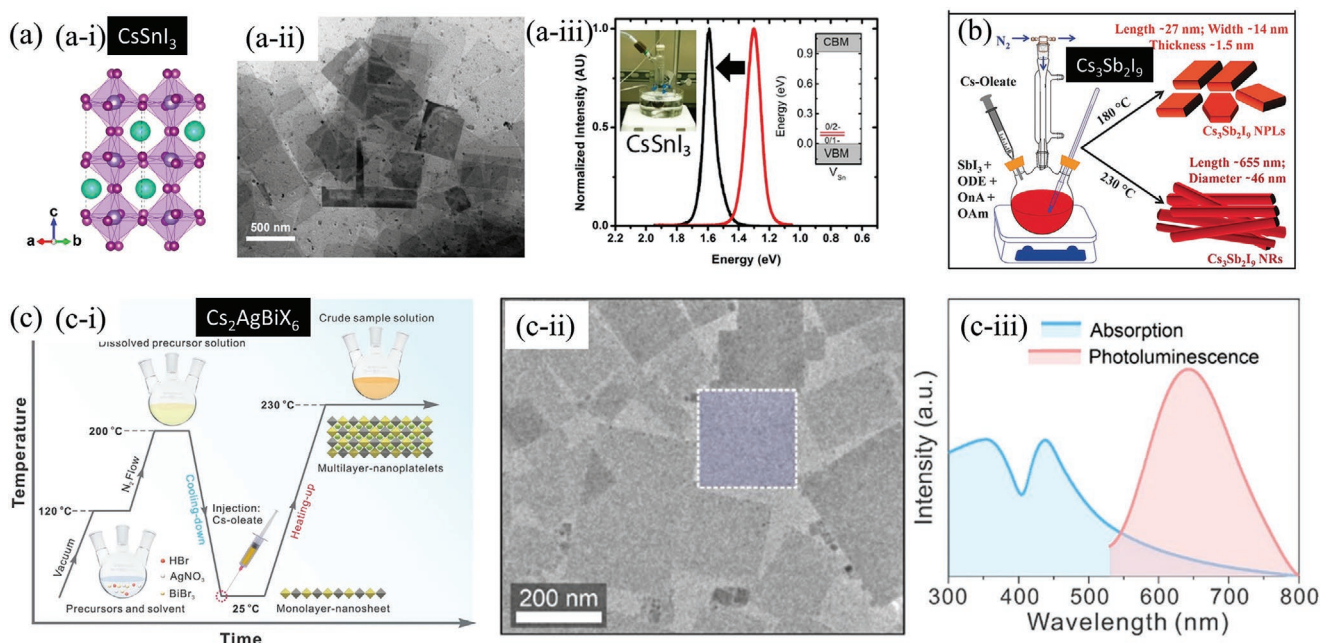


Figure 11. a) Orthorhombic crystal structure (i), TEM image (ii), and corresponding PL spectra of CsSnI₃ NPLs (black line) with respect to its bulk PL (red line) (iii). The colors green, gray, and purple in (i) correspond to Cs, Sn, and I atoms, respectively. Reproduced with permission.^[101] Copyright 2018, American Chemical Society. b) Schematic illustration of the shape-controlled synthesis for Cs₃Sb₂I₉ NPLs. Reproduced with permission.^[102] Copyright 2017, John Wiley & Sons. c) Schematic representation of the synthetic procedure (i), corresponding TEM image (ii), and UV-vis absorption and PL spectra (iii) of Pb-free Cs₂AgBiBr₆ double perovskite NPLs. Reproduced with permission.^[100] Copyright 2021, American Chemical Society.

conditions (Figure 11a).^[101] The theoretical studies revealed that the Sn-rich conditions can help to minimize defect density due to higher formation energies of defects under these conditions. The CsSnI₃ NPLs exhibit a significant blue shift compared to their bulk counterpart, suggesting that these NPLs are strongly quantum-confined (Figure 11a-iii). Besides, Pb-free NPLs of perovskite derivatives have also been reported. For example, Nag's group demonstrated the synthesis of 2D Cs₃Sb₂I₉ NPLs by the hot-injection synthesis method (Figure 11b).^[102] The as-synthesized nanoplatelets exhibit an average length of ≈27 nm, a breadth of ≈14 nm, and a thickness of ≈1.5 nm. The thickness of Cs₃Sb₂I₉ NPLs is small enough to bring about the quantum confinement effect, leading to a blue shift in the optical gap.^[102] In addition, Cs₃Sb₂I₉ NPLs are sensitive to the electron beam and could be degraded into hollow structures under the irradiation of the electron beam within a few seconds. Later, Lian et al.^[98] extended the hot-injection synthesis to Cs₃Bi₂Br₉ NPLs with a length of ≈60–250 nm and a thickness of ≈9 nm. The layered feature of Cs₃Bi₂Br₉ crystalline structure promoted the formation of the NPLs. Compared with Cs₃Bi₂Br₉ NCs, the large blue-shift and the extremely sharp first exciton peak in the absorption spectrum of Cs₃Bi₂Br₉ NPLs are attributed to the large exciton binding energy and quantum confinement in the 2D nanoplatelets. Additionally, the Cs₃Bi₂Br₉ NPLs showed narrow PL (FWHM ≈ 39 nm) compared to that of Cs₃Bi₂Br₉ NCs (FWHM ≈ 48 nm). Anion exchange could also be applied to effectively adjust the composition of the Cs₃Bi₂Br₉ NPLs. Benefiting from the passivation with BiOBr and ligands, Cs₃Bi₂Br₉ NPLs exhibit excellent stability under air and light illumination, facilitating further investigation on their photovoltaic and optoelectronic applications.

Very recently, Liu et al.^[100] and Huang et al.^[99] simultaneously reported the synthesis of Cs₂AgBiX₆ double perovskite NPLs using the hot-injection synthesis approach. The schematic illustration of the synthesis of Cs₂AgBiX₆ (X = Cl, Br, I) NPLs reported by Liu et al.^[100] is shown in Figure 11c-i. The precursors were first dissolved at 200 °C and then Cs-oleate was injected at room-temperature to obtain monolayer NPLs, followed by annealing at 230 °C to obtain thick NPLs. The prepared Cs₂AgBiBr₆ NPLs showed a rectangular morphology with an average edge length of 180 ± 130 nm and a thickness of 3.6–6.0 nm (Figure 11c-ii). In addition, the lateral dimension of the NPLs could be adjusted from ≈330 ± 230 to 630 ± 380 nm by adding different amounts of octylamine in addition to OLA. As shown in Figure 11c-iii, the Cs₂AgBiBr₆ NPLs exhibit two peaks (355 nm (3.5 eV) and 438 nm (2.84 eV)) in the absorption spectrum and a broad weak PL emission centered at ≈640 nm (≈1.94 eV) with the FWHM of 143 nm (427 meV), which are consistent with those of the Cs₂AgBiBr₆ NCs (Figure 11c-iii). This suggests that these NPLs exhibit bulk-like optical properties. However, they found that the monolayer double perovskite NPLs exhibit a significant blue-shift in the PL emission. Therefore, thorough experimental and theoretical studies are needed for a better understanding of quantum-confinement effects in double perovskite NPLs. Furthermore, it was found that the as-prepared Cs₂AgBiBr₆ NPLs exhibit better performance for CO₂ photoreduction compared to their nanocube counterpart, demonstrating its potential for photocatalytic applications.^[100]

3. Optoelectronic Properties

3.1. Optical Properties

3.1.1. Linear Optical Properties

The development of 2D layered perovskites for thin-film applications has been limited by the challenges over controlling the phase purity and microstructure.^[142,143] On the other hand, it has been shown that these challenges can be addressed through the colloidal synthesis of NPLs.^[81,144,145] This makes colloidal perovskite NPLs more appealing as a controllable platform for examining their intrinsic optical properties. The transition from thicker nanocrystals to thin NPLs leads to a dramatic change in the optical properties, as shown in Figures 1e and 12d,e.^[9,44] Despite the lateral dimensions being comparable to those of conventional bulk perovskite flakes, their reduced thickness causes the quantum confinement effects.^[72,146,147] Under a simple effective mass approximation, the confined gap is inversely proportional to the square of the dimensions.^[148,149] Therefore, the reduction in the vertical dimension of perovskite NPLs increases the confined energy and hence the width of band gap.^[150,151] Moreover, the exciton binding energy, E_b , is influenced by the dimensions of the system, as shown by Equation 1.

$$E_b = \left(\frac{2}{\alpha - 1} \right)^2 E_e \text{ with } \alpha = 3 - \gamma e^{-\frac{L_w}{2a_0}} \quad (1)$$

where α is the dimensional parameter of the system, a_0 is the Bohr radius of the exciton, L_w is the width of quantum well, γ is the empirical correction factor, and E_e is the effective Rydberg constant.^[152–154] This classical model predicts that the reduced dimension effect enhances the exciton binding energy of perovskite NPLs.^[28,41] The comparative study on a model system with no dielectric mismatch between organic and inorganic layers reveals that the exciton binding energy would be enhanced by four times from 29 meV (3D system) to 116 meV (2D system).^[155,156] In addition to quantum confinement, the perovskite NPLs exhibit strong dielectric confinement. With a significant dielectric mismatch between the perovskite layer and surrounding medium, the perovskite NPLs are treated as 2D quantum wells with dielectric confinement effect.^[41,151,156,157] In bulk perovskites, the Coulomb interaction between electron and hole is effectively screened due to the high dielectric nature of perovskite. This is commonly called the dielectric screening effect. On the other hand, the Coulomb interaction between electron and hole in perovskite NPLs experiences a low dielectric constant environment as the electric field of Coulomb force is extended into the space outside of perovskite. As the perovskite NPLs become thinner, the electric fields from Coulomb interaction become more exposed to the surrounding low dielectric constant environment. Therefore, dielectric screening becomes less effective in perovskite NPLs, resulting in stronger interactions between electrons and holes, thus increasing the exciton binding energy (≈200–500 meV for NPLs versus 5–60 meV for bulk 2D layered perovskites and unconfined NCs),^[18] as well as

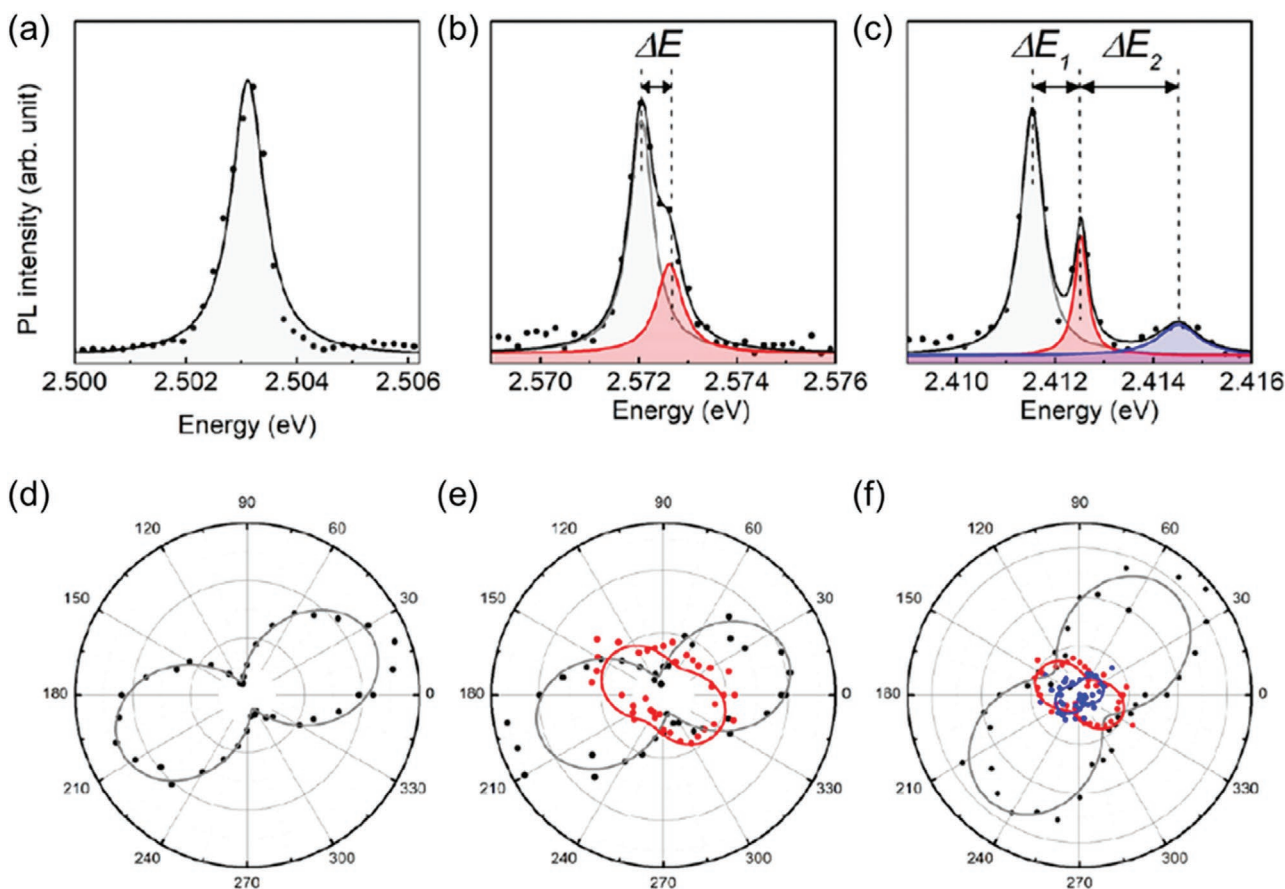


Figure 12. Excitonic fine structure of the CsPbBr₃ nanoplatelets. PL spectra of the single nanoplatelets with a) one peak, b) two peaks, and c) three peaks as well as the corresponding linear polarization properties (d–f). In (b,c), the splittings are labeled ΔE , ΔE_1 , and ΔE_2 and are deduced from the fittings to be 0.71, 0.57, and 1.84 meV, respectively. Reproduced with permission.^[116] Copyright 2020, American Chemical Society.

the excitonic absorption coefficient.^[68,70,158,159] The enhancement in exciton binding energy (ΔE_b) can be quantified by the following relation (Equation 2):^[160,161]

$$\Delta E_b \approx 2 \left(\frac{\epsilon_1 - \epsilon_2}{\epsilon_1 + \epsilon_2} \right) \left(\frac{q^2}{\epsilon_1 \epsilon_0 d} \right) I \quad (2)$$

where ϵ_0 is the vacuum permittivity, q is the fundamental charge, I is an ideality factor close to unity and d is the thickness of the inorganic framework, and ϵ_1 and ϵ_2 are the dielectric constants of the inorganic and the organic sublattices, respectively. As a consequence of both quantum and dielectric confinement effects, the absorption spectrum of colloidal NPLs exhibit sharp and strong excitonic peaks, along with blue-shifted bandgaps compared to their bulk counterparts.^[70,151] Accompanying these changes in optical absorption properties, an increase in the photoluminescence quantum yield and radiative decay rate in perovskite NPLs are also theoretically predicted. Radiative decay rate and the oscillator strength are linearly proportional to one another according to both Einstein relations and Fermi's Golden rule.^[162–164] Thus, the increase in oscillator strength of NPLs stemming from quantum and dielectric confinement effects result in induced radiative decay

rate for perovskite NPLs. The increased radiative decay rate further enhances the photoluminescence quantum yield (Φ) via the relation $\kappa_r / (\kappa_r + \kappa_{nr})$.^[165]

Linear optical properties at the single-particle level have been extensively studied for colloidal cubic nanocrystals,^[14,27,166–168] but less attention has been received for NPLs. Huo et al. demonstrated that a single CsPbBr₃ nanoplatelet shows no blinking effect and exhibits highly pure single-photon emission with $g^2(0) = 0.1$ at a temperature of 5 K.^[116] Furthermore, by measuring PL spectra from multiple single nanoplatelets with PL peak above 2.4 eV, they showed that the CsPbBr₃ NPLs have multiple PL peaks as illustrated in Figure 12a–c. Some showed one peak, while some show two or three peaks. The energy differences are labeled as ΔE , ΔE_1 and ΔE_2 , with numerical values of 0.71, 0.57, and 1.84 meV, respectively. Figure 12d–f illustrates the polar plots of the polarization dependence of the intensity of each peak present in the corresponding spectra in Figure 12a–c. The lateral anisotropic morphology induced an almost 80% polarization of the single peak emission in Figure 12a. This angle-dependent polarization is also reported in perovskite nanostructures including NPLs.^[14] In the cases of nanoplatelets exhibiting multiple emission peaks (Figure 12b,c), the

polarizations of the two lower energy peaks (shaded in red and blue in Figure 12b,c) are almost orthogonal to each other (Figure 12f), whereas the higher energy peak is almost co-polarized as the lower energy peak. The observed polarization dependence of the emission peaks strongly indicates that they arise from the exciton fine structure.^[116] These findings provide an extra degree of freedom to manipulate the electronic and optical properties of perovskite NPL-based materials and devices.

3.1.2. Nonlinear Optical Properties

Nonlinear optical devices include high-speed optical switches, modulators, lasers, and other nonlinear photonic devices. The first step to successfully developing perovskite NPLs for these devices is to achieve an in-depth understanding of the nonlinear optical property of perovskite NPLs.^[169–172] The general relationship between light and materials can be described through Equation 3.^[173,174]

$$p(t) = \epsilon_0 (\chi^{(1)} E(t) + \chi^{(2)} E^2(t) + \chi^{(3)} E^3(t) + \dots + \chi^{(n)} E^n(t)) \quad (3)$$

where $p(t)$ is the macroscopic polarizability, ϵ_0 is the vacuum permittivity, $\chi^{(n)}$ is the n th order nonlinear susceptibility, and $E(t)$ is the electric field strength of the incident light. Whereas the first term (i.e., $\chi^{(1)} E(t)$) describes the linear optical effect, the remaining high-order terms account for the nonlinear optical response of the materials. In general, the properties of the material are determined by the linear term and the higher order terms become negligible. On the other hand, when the electric field is strong enough (i.e., under strong illumination), the higher order terms are no longer negligible. The strong electric field alters the propagation of light in the material and various nonlinear optical processes take place. Furthermore, it is expected that the strong dielectric and quantum confinement of NPLs along the thickness axis facilitates not only linear but also nonlinear optical properties.^[172] Despite their potential importance, there have only been a handful of reports on the nonlinear optical properties of colloidal NPLs. It is therefore worth discussing these recent reports in this review.

Multiphoton Absorption Properties: One-photon absorption generally has a small penetration depth due to the high absorption coefficient of the perovskite.^[169,175,176] On the other hand, multiphoton absorption possesses much deeper penetration owing to the longer incident wavelength (e.g., infrared excitation).^[177,178] Therefore, the materials with high multiphoton absorption cross sections have advantages over linear optics and find applications in various nonlinear optical detection techniques such as single molecule detections and multi-photon high contrast bio imaging. Very recently, a few interesting studies on the multiphoton absorption process of perovskite NPLs were reported. In 2019, Zhao et al. compared the one-photon and two-photon absorption cross sections of CsPbBr_{2.7}I_{0.3} and CsPbI₃ nanocrystals (i.e., both nanocubes and nanoplatelets).^[179] Two-photon absorption cross section is usually quoted in the units of Goeppert-Mayer, GM, where 1 GM is 10⁻⁵⁰ cm⁴ s photon⁻¹. Interestingly, CsPbBr_{2.7}I_{0.3} NPLs exhibit much higher two-photon cross section (346 GM nm⁻³) than

their nanocube counterparts (86 GM nm⁻³ for CsPbBr_{2.7}I_{0.3} and 127 GM nm⁻³ for CsPbI₃), revealing the influence of dimensionality on the multiphoton absorption processes. On the other hand, Roy et al. later reported the opposite trend in the nonlinear refraction coefficients of CsPbBr₃ and CsPbBr_{1.5}I_{1.5} perovskite nanocrystals (i.e., nanocube and NPL colloids).^[180] By carrying out time-resolved beam-deflection measurements, they found giant thermo-optical nonlinear refraction coefficients that were significantly higher for the nanocube than for NPLs (Figure 13a). They further revealed the influence of composition on the nonlinear optical properties, thus the mixed halide perovskite, CsPbBr_{1.5}I_{1.5}, has lower nonlinear refraction coefficients than the single halide perovskite, CsPbBr₃. The nonlinear refraction properties are attributed to the thermal lensing effect upon above-bandgap excitation by continuous-wave (cw) lasers. Briefly summarizing, the main findings of these two studies discussed: changing from nanocubes to NPLs lead to enhanced nonlinear absorption cross sections, whereas the same dimensional changes lead to reduced nonlinear refraction coefficients. Likewise, structural characteristics, such as dimension, size, and shape dictate various nonlinear optical properties of NPLs differently. As we expect that many different parameters, such as sample composition, fabrication conditions and sample quality, might dictate the nonlinear optical properties of NPLs, further studies are necessary to shed further light on these effects to achieve excellent nonlinear responses.

Plasmon-Exciton Polariton: One of the most intriguing nonlinear phenomena to occur in the strong light-matter coupling regime is plasmon-exciton polariton formation. Briefly speaking, a plasmon is a bosonic quasiparticle resulting from the quantization of plasma oscillations, i.e., collective oscillations of free electrons.^[181–183] Another quasiparticle formed as a consequence of strong light-matter interaction is the polariton. When light, i.e., electromagnetic field, propagates in a medium and its frequency is close to the resonance frequency of the medium, the electromagnetic field polarizes the medium near the resonant frequency.^[184] The polarization of the propagation medium can influence the propagating electromagnetic field. When this light-matter interaction between “bare” photon and “bare” medium excitation is strong enough, a new quasiparticle, called a polariton, is formed. The formation of polariton can be explained by using the dispersion relation which describes the allowed frequency, ω , within the material in dependence on the wave vector κ , in the form of $\omega(\kappa)$. Using Maxwell equations, the dispersion relation of polariton can be expressed as follows (Equation 4).^[184,185]

$$\kappa^2 = \frac{\omega^2}{c^2} \epsilon(\omega) \quad (4)$$

where c is the velocity of photon in vacuum, $\epsilon(\omega)$ is the dielectric function of the material. In the absence of the coupling, the dispersion relations of a bare photon (i.e., $\omega = c\kappa$) and bare medium excitation (e.g., $\omega = \omega_0$ for exciton) are dictated by the wave equation and their dispersion curves cross one another. On the other hand, in the presence of strong light-matter coupling, the mixing of photon and medium excitation occurs at the crossing point resulting in the formation of new normal modes, the upper and lower polaritons. As those polariton branches are split by the Rabi energy, $\hbar\Omega$, near the resonance

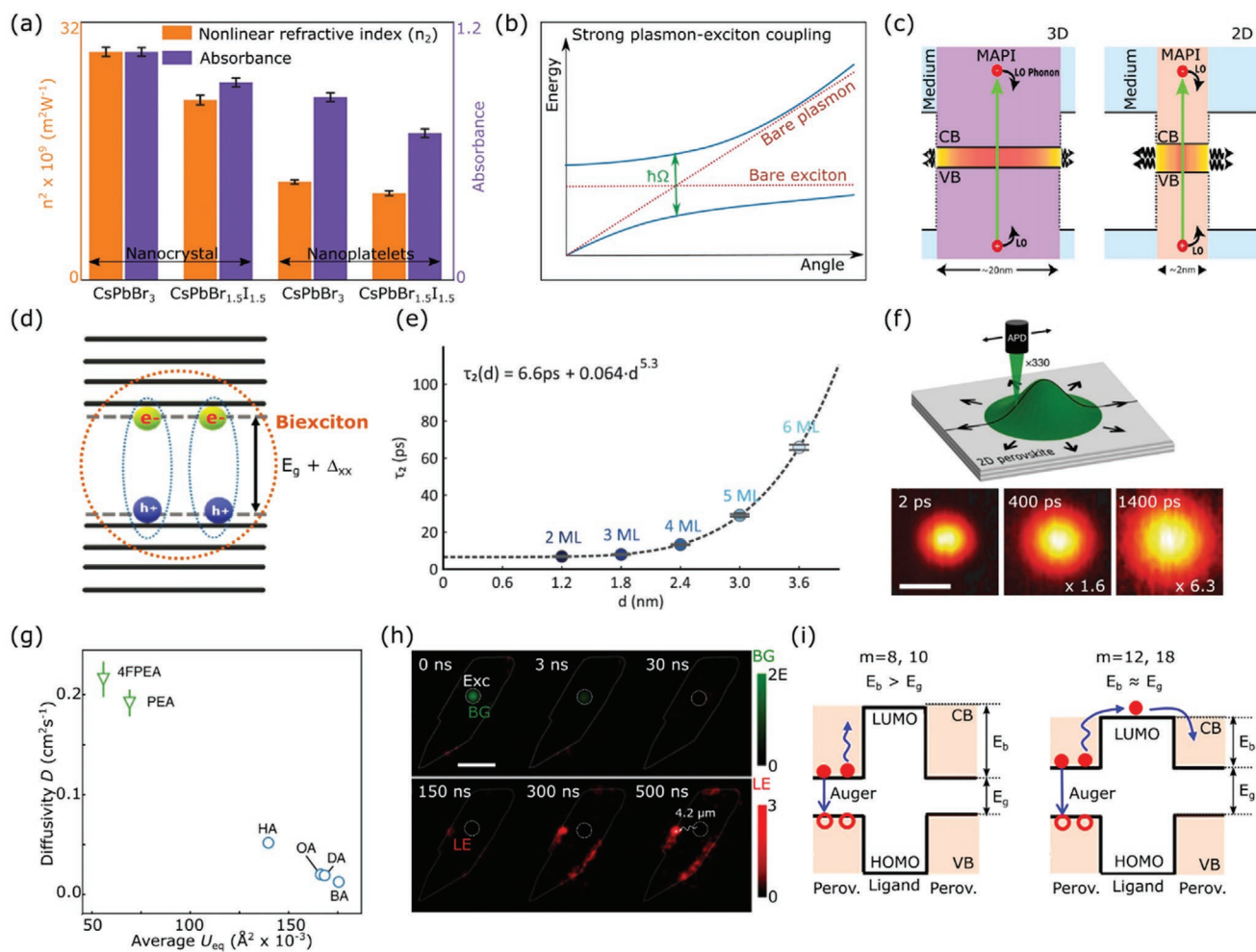


Figure 13. a) Comparison of nonlinear refraction coefficient, n_2 and absorbance upon pump excitation of 403 nm. Reproduced with permission.^[180] Copyright 2020, American Chemical Society. b) Schematic dispersion curves for plasmon-exciton mixed states formed with the exciton of perovskite nanoplatelets and surface plasmon polaritons in the strong coupling regime. Reproduced with permission.^[196] Copyright 2020, Royal Society of Chemistry. c) Schematic diagram of carrier cooling process in thick (quasi-3D) and thin (2D) NPLs. After photoexcitation, the carriers cool down via the emission of LO phonons. Both screening effects and larger surface-to-volume ratios explain why carrier cooling is faster in 2D NPLs and it has no carrier density dependence. Reproduced under CC-BY license.^[70] Copyright 2018, American Chemical Society. d) Schematic for biexciton formation. The bandgap is renormalized due to the biexcitonic induced stark effect. e) The extracted lifetime is plotted as a function of NPL thickness, showing a power-law dependence of $\tau_2 \propto d^5$. Reproduced with permission.^[123] Copyright 2020, American Chemical Society. f) Schematic illustration of time-resolved photoluminescence microscopy and the representative photoluminescence snapshots at several time positions showing diffusion motion of exciton. g) Diffusivity D as a function of average atomic displacement U_{eq} for different organic spacers: 4-fluoro-phenethylammonium (4FPEA), phenethylammonium (PEA), hexylammonium (HA), octylammonium (OA), decylammonium (DA), butylammonium (BA). Reproduced under CC-BY license.^[231] Copyright 2020, The Author(s). Published by Springer Nature. h) A set of photoluminescence intensity images at different delay times after excitation (White dashed circle), showing the evolution of bandgap (BG, green) and low energy (LE, red) photoluminescence signals. The scale bar is 5 μm . Reproduced with permission.^[234] Copyright 2020, American Chemical Society. i) Energy alignment in $(\text{C}_m\text{H}_{2m+1}\text{NH}_3)_2\text{PbI}_4$ perovskites with different ligand alkyl lengths and the proposed Auger process in the quantum wells. E_g is the bandgap energy of the quantum well and E_b is the electron energy barrier formed by the ligand. An electron transfer between the neighboring quantum wells over the LUMO level of ligands is energetically allowed through a many-body Auger recombination in $m = 12$ and 18 ($E_b \approx E_g$) perovskites but not in $m = 8$ and 10 ($E_b > E_g$) perovskites. Reproduced with permission.^[238] Copyright 2018, American Chemical Society.

frequency, the avoided crossing or anticrossing feature of the dispersion curve is a strong indication of polariton formation.^[184,186,187] Therefore, the formation of a polariton is experimentally confirmed with momentum resolved spectroscopy techniques such as angle-resolved reflection, photoluminescence, and photoemission measurements.^[188–191] When the Rabi energy exceeds the dissipation rates of both photons and plasmons, the system is said to enter the so-called strong coupling regime.^[192,193] At this condition, the incident light can couple with the coherent delocalized electron oscillations on metal

surfaces, i.e., surface plasmon, to form surface plasmon polaritons, which are also known as localized surface plasmons. The surface plasmon polariton then generates an evanescent field on the metal surface. When semiconducting materials with excitons are placed in the vicinity of the evanescent field, strong coupling between plasmons and excitons can occur, and new quasiparticles called plasmon-exciton polaritons (or plexitons) are formed.^[178,194,195] Again, the formation of this new quasiparticle can be experimentally confirmed with the appearance of an anti-crossing dispersion, since the coherent and reversible

energy exchange between plasmons and excitons leads to the splitting of the excited state, i.e., Rabi splitting, and produce the new hybrid modes (Figure 13b).^[196,197]

Guvenc et al. studied the strong plasmon-exciton coupling in colloidal halide perovskite nanocrystals with various morphologies and compositions.^[196] The colloidal halide perovskite nanocrystals (i.e., CsPbBr_xI_{3-x} NPLs, CsPbI₃ NPLs, CsPbI₃ nanowires) were placed on a flat silver metal film functionalized with 16-mercaptohexadecanoic acid. Angle-resolved reflectivity measurements exhibit polariton dispersion curves with a clear anti-crossing feature indicative of the mixed plasmon-exciton states. The maximum Rabi splitting energy of 90 meV was observed for CsPbI₃ NPLs while Rabi splitting energy was decreased with reducing dimensionality or mixing halide composition (ca. 70 meV for CsPbI₃ nanowires or 55 meV for CsPbBr_xI_{3-x} NPLs). Su et al. explored the possibility of achieving room temperature polariton lasing by examining a microcavity consisting of CsPbCl₃ NPL embedded in the bottom and top distributed Bragg reflector (DBR) mirrors.^[197] The lower polariton dispersion features observed in both angle-resolved reflectivity and photoluminescence spectra unambiguously indicate the presence of strong exciton-photon coupling. Interestingly, power-dependent angle-resolved photoluminescence spectra further provide clear experimental evidence for polariton condensation and polariton lasing at room temperature. These studies showed that perovskite nanocrystals, particularly NPLs, not only are very promising candidates for studying plasmon-exciton interaction but also can find various applications in polariton lasers, light-emitting diodes and surface-enhanced spectroscopies.

3.2. Carrier/Exciton Dynamics

3.2.1. Carrier Dynamics

Relaxation Dynamics and Exciton Behavior: Since carrier dynamics play a central role in a wide range of optoelectronic devices, it is important to understand the charge-carrier dynamics in perovskite NPLs, particularly compared to their bulk 3D counterparts. A comparison between 3ML MAPbI₃ NPLs ($d \approx 2$ nm) and quasi-3D perovskites ($d \geq 15$ nm) reveal significantly different photoinduced carrier dynamics (Figure 13c).^[70] In this study carried out by Hintermayr et al., thicker NPLs are referred to as quasi-3D NPLs due to their bulk-like optical properties. In quasi-3D perovskite, nonthermal electron-hole distributions are instantaneously generated upon above-band gap excitation. This initial nonthermal distribution then becomes thermalized via carrier-carrier and carrier-phonon scattering to the Fermi-Dirac distribution of carriers within several sub-picoseconds.^[156,198] The carrier temperature at this stage is higher than the lattice temperature, and the carriers are therefore commonly referred to as hot carriers. While subsequent carrier cooling takes place via phonon emission, mainly through Fröhlich interactions with longitudinal optical (LO) phonons, this process slows down for high carrier densities due to the reabsorption of phonons, and this is referred to as the phonon bottleneck effect.^[158,199] In 2D perovskite

NPLs, the initial nonthermal distribution of carriers and the subsequent thermalization process are very similar to their 3D counterparts. However, the carrier cooling process in 2D NPLs has been found to be much faster and independent of the excitation density. Owing to the thin nature of perovskite NPLs, the emitted optical phonon and subsequently the created acoustic phonons are more likely to transfer their energy into the colder surroundings, resulting in rapid heat dissipation and a lower chance of hot phonon reabsorption (Figure 13c). Furthermore, the Fröhlich interactions (coupling between carriers and longitudinal optical phonons)^[200,201] in 2D systems have been found to be independent of the carrier density. In 3D systems, although dielectric screening over all 3 principal axes weakens Fröhlich interactions, the scattering of carriers by longitudinal optical phonons is still responsible for the early-time (sub-picosecond) cooling process at low excitation densities. At high excitation densities, the screening of Fröhlich interactions becomes stronger, resulting in less efficient cooling processes. In 2D systems, the Fröhlich interaction is reduced by a factor

$$\frac{\epsilon_1 + \epsilon_2}{2}$$

with respect to vacuum, where ϵ_1 and ϵ_2 are the dielectric constants of the environment (e.g., ligands) on each side of the 2D layer.^[201] Despite this, Fröhlich interactions in 2D NPLs are still stronger than those in their 3D counterparts due to the reduced dielectric screening from the out-of-plane direction. In addition, the increase in excited carrier density only screens the long-range coupling between carriers and phonons along the in-plane and the Fröhlich interaction in out-of-plane direction through low-dielectric surrounding remains unaffected. Consequently, perovskite NPLs exhibit carrier density-independent behavior and an efficient carrier cooling process. Besides, 2D NPLs and quasi-3D perovskites also have different excitonic behaviors. By directly exciting into the excitonic state, a cold exciton in the 1s excitonic state is created for both 2D NPLs and quasi-3D perovskites. As the thermal energy at room temperature (25 meV) is sufficient to overcome Coulombic interactions between electrons and holes in 3D perovskite (since the exciton binding energy is only 5 to 29 meV at room temperature), the cold exciton in the 3D perovskite scatters off to the continuum state and dissociates into free electrons and holes.^[199,202] On the other hand, the cold exciton in 2D NPLs hardly dissociates due to large exciton binding energy (i.e., 200–500 meV) and stays in the 1s excitonic state until it decays via monomolecular recombination.^[68,70,158,159] We note here that it is a unique feature of semiconductor quantum wells. The semiconductor quantum dots exhibit 3D quantum confinement which leads to atomic-like discrete energy levels. The increased interlevel spacing stemming from 3D quantum confinement in QDs prevents effective carrier-LO phonon coupling.^[203,204] On the other hand, semiconductor nanoplatelets represent a class of quantum wells, having quantum confinement only along one dimension, and with a large lateral size (nonconfined dimension). Accordingly, the energy levels of nanoplatelets are not completely discrete and the interlevel spacing is not as large as in quantum dots. As the interlevel spacing in bulk, 2D perovskites are not large enough to suppress carrier-LO phonon coupling, dielectric quantum confinement plays a dominant role in those low-dimensional semiconductors and enhances carrier-LO phonon coupling.^[205]

Biexciton and Exciton–Exciton Annihilation: An interesting multiparticle phenomenon in perovskite nanocrystals is biexciton formation.^[156,206–208] Whether it is hot or cold excitons, the attractive interaction between pairs of excitons and the concomitant biexciton-induced Stark effect induces a red shift in the bleaching peak (Figure 13d).^[208,209] Generally, the excitonic Stark effect describes the energy shift of the lowest exciton band caused by the built-in electric field between the electron and hole through Coulombic interactions.^[210,211] Consequently, the red-side shoulder of the ground state bleach peak and the PL spectra become spectral signatures for biexciton formation. Vale et al. showed that biexcitons form in CsPbBr₃ NPLs when an average exciton occupancy per particle $\langle N_x \rangle$ is greater than 1.^[212] More interestingly, Shukla et al. observed the spectral signature of the biexciton in CsPbBr₃ NPLs even under weak illumination with a low associated carrier density where $\langle N_x \rangle$ was smaller than 1.^[208] This is an interesting optical behavior that comes from the enhanced exciton absorption coefficient in 2D NPLs. The probe beam can create the band-edge exciton in perovskite NPLs while the pump beam generates either hot or cold excitons. As a result, probe-induced biexcitons are formed in perovskite NPLs.

Other interesting optical phenomena of perovskite NPLs that originate from the high exciton absorption coefficient are multiexciton processes, such as exciton–exciton annihilation (EEA) or Auger recombination (AR).^[206,208,212,213] Briefly speaking, EEA is a two-particle process, where an exciton recombines non-radiatively to the ground state and transfers its energy to a second exciton.^[214] On the other hand, AR is the three-body interaction where an electron and hole recombine together, accompanied by energy and momentum transfer to a third particle, which could be either an electron or hole.^[158] We note here that while strictly speaking AR is different from EEA, it is difficult to experimentally differentiate whether excitons or free carriers are involved in this many-body process.

A recent study on a series of perovskite NPLs with different compositions (i.e., MAPbI₃, FAPbI₃, and CsPbI₃) showed there to be fluence-dependent AR processes.^[206] Under moderate fluences, the AR process is diffusion-limited and has a typical lifetime of several tens to hundreds of picoseconds. On the other hand, intense excitation creates multiple excitons in perovskite NPLs within an area only a few times larger than the exciton Bohr radius.^[212] Accordingly, the AR process is no longer diffusion-limited but shows an intrinsic AR lifetime of less than 10 ps. The thickness dependence of AR in a series of CsPbBr₃ NPLs was studied by Gramlich et al.^[213] By observing AR lifetimes in perovskite NPLs with different thicknesses, they found that thicker NPLs have longer AR lifetimes from 7 to 60 ps for 2 to 6 monolayers (Figure 13e). This size-dependent AR behavior was further observed in perovskite NPLs with different lateral sizes. Perovskite NPLs with an edge length of 14 nm were found to have shorter AR lifetimes than NPLs with 35 nm edge lengths. Based on this observation, they established the thickness-dependent power law for NPLs to have an exponent of 5.3 (i.e., $\tau_2 \propto d^{5.3}$). This thickness-dependent power law for perovskite NPLs significantly deviates from the universal volume scale law for nanocrystals (i.e., $\tau_2 \propto V$, V is the volume of the nanocrystal).^[215–217] This volume scale law for nanocrystals is attributed to three major effects: 1) confinement-induced

state mixing, 2) carrier–carrier Coulomb coupling and 3) surface effects, and each of these three effects follows a $1/d$ dependence. The use of the volume scale law has been reasonably successful for estimating Auger lifetime in 0D nanocrystals, i.e., quantum dots. In 0D nanocrystals, the generated excitons are 3D-confined and interact with each other without diffusion or collision processes. On the other hand, quantum confinement in 1D and 2D nanocrystals, such as nanowires or NPLs, is not uniform along all principal axes. For example, in NPLs, quantum confinement occurs along the thickness axis, while the lateral area is nonconfined. Excitons in 2D systems diffuse over the unconfined lateral area and recombine via binary collision. Consequently, the Auger lifetime in NPLs depends on the binary collision frequency for forming biexciton complex and hence become area (d^2) dependent.^[218] Quantum confinement still occurs along the thickness axis in 2D NPLs. The abrupt confinement potential breaks strict momentum conservation and enhances the AR process.^[217–219] In other words, the degree of quantum confinement dictates the probability of Auger recombination occurring. Therefore, the AR process in 2D NPLs can be induced by quantum confinement along the thickness axis. A recent work by Gramlich et al. reveals that weakly confined (lateral) and strongly confined (vertical) dimensions play different roles in AR processes and need to be considered independently.^[213] We note that perovskite NPLs can be ideal systems to test how structural parameters, such as lateral size and dimensionality, affect AR and EEA processes, since these parameters can be tuned independently.

3.2.2. Transport Dynamics

Beyond nonradiative recombination, charge-carrier mobility plays a critical role on device performance, and it is important to understand the factors influencing mobility.^[220–223] The past decade of intensive studies has shown that both intrinsic and extrinsic factors limit charge-carrier mobilities in 3D perovskites.^[224–226] While intrinsic electron–phonon coupling, namely Fröhlich interactions, limit the charge-carrier mobilities to below that which would be expected from the electronic band curvature, extrinsic factors, such as charge carrier scattering by grain boundaries, dopants, defects, and energetic disorder, further lower charge-carrier mobilities. In fact, the charge carrier mobility values in thin films are typically found to be tens of $\text{cm}^2 (\text{V}^{-1} \text{s}^{-1})$. While this is below the values achievable in single crystals, and substantially below the values expected from the band curvature, it is still sufficient to give rise to charge-carrier diffusion lengths in the micrometer range in 3D perovskites (Table 3).^[227] On the other hand, the in-plane carrier mobilities in reduced-dimensionality perovskite lie in the range of 10^{-2} to $1 \text{ cm}^2 (\text{V}^{-1} \text{s}^{-1})$. Strictly speaking, not all 2D perovskites are perovskite NPLs. However, we can still learn from 2D and quasi-2D perovskites, particularly single-phase 2D homologous perovskites, to understand carrier diffusion dynamics in perovskite NPLs.

Milot et al. scrutinized carrier transport in a series of 2D perovskites and suggested that both excitons and traps play a decisive role.^[228] The effective charge-carrier diffusion mobility ($\phi\mu$) is determined by the mobility (μ) and the photon-to-charge

Table 3. Charge carrier and exciton diffusivities, determined experimentally at room temperature.

Materials	Architecture	Electron, hole, exciton	Mobility [$\text{cm}^2(\text{V s})^{-1}$]	Diffusivity [$\text{cm}^2 \text{s}^{-1}$]	Method	Refs.
Composition	<i>N</i>					
(MA)PbI ₃	Bulk	Film	Electron, hole	35		THzC
		Single crystal	Electron, hole	60		
(BA) ₂ (MA) _{<i>n</i>-1} Pb _{<i>n</i>3<i>n</i>+1}	1	Single crystal	Exciton		0.058 ± 0.005	Tr-PLM [230]
	2				0.067 ± 0.007	
	3				0.121 ± 0.02	
(BA) ₂ (MA) _{<i>n</i>-1} Pb _{<i>n</i>3<i>n</i>+1}	1	Single crystal	Exciton		0.06 ± 0.03	TAM [225]
	2				0.07 ± 0.03	
	3				0.15 ± 0.04	
	4				0.25 ± 0.06	
	5				0.34 ± 0.03	
(BA) ₂ PbI ₄	1	Single crystal	Exciton		0.013	Tr-PLM [231]
(BA) ₂ (MA) ₂ Pb ₃ I ₁₀	3	Single crystal	Hole	0.000032 ^{a)}		SCLC ^{c)} [239]
				0.0096 ^{b)}		
(BA) ₂ (MA) ₂ Pb ₃ I ₁₀	3	Single crystal	Hole	0.00015 ^{a)}		SCLC ^{c)} [240]
			Electron	1.2 ^{b)}		
(PEA) ₂ (MA) _{<i>n</i>-1} Pb _{<i>n</i>3<i>n</i>+1}	1	Single crystal	Exciton		0.648 ± 0.05	Tr-PLM [230]
	2				0.157 ± 0.005	
	3				0.189 ± 0.008	
(PEA) ₂ (MA) _{<i>n</i>-1} Pb _{<i>n</i>3<i>n</i>+1}	2	Single crystal	Electron, hole		0.081 ± 0.031	Tr-PLM [234]
	3				0.115 ± 0.03	
	4				0.405 ± 0.2	
(PEA) ₂ (MA) ₂ Pb ₃ I ₁₀	3	Single crystal	Hole	0.000012 ^{a)}		SCLC ^{c)} [239]
				0.044 ^{b)}		
PEA ₂ PbI ₄	1	Single crystal	Exciton		0.192	Tr-PLM [231]
(PEA) ₂ PbI ₄	1	Single crystal	Exciton	250	2.1 ^{d)}	Tr-PLM [232]
	1	Single crystal		40	1 ± 0.4	
(mF-PEA) ₂ PbI ₄	1	Single crystal	Exciton		1.91	Tr-PLM [230]
(ALA) ₂ (MA) ₂ Pb ₃ I ₁₀	3	Single crystal	Hole	0.000024 ^{a)}		SCLC ^{c)} [239]
				0.013 ^{b)}		

^{a)}Out-of-plane motion; ^{b)}In-plane motion; ^{c)}Space charge limited current method; ^{d)}100 K.

branching ratio (ϕ). Unlike 3D perovskites, where the photon-to-charge branching ratio is generally assumed to be unity, the enhanced quantum confinement and the corresponding high exciton binding energy in 2D perovskites increase the probability of exciton formation.^[227] In accordance with the reduced value of ϕ , the effective diffusion mobility decreases significantly. In contrast, the replacement of the A-site cation with organic spacers or surface functionalization with organic ligands can passivate the traps at the surface of the perovskite layer, reducing Shockley-Read-Hall recombination and therefore increase in charge carrier mobility. Interestingly, Weidman et al. highlighted another factor that can dictate the effectiveness of trap states in thin NPLs.^[9] The formation of large polarons, facilitated by the rotational freedom and permanent dipole moment of the A-site cation, screens the interaction of charges with defects and phonons.^[229] This polaronic effect is attributed to low defect/phonon scattering rates in 3D perovskites despite

the high defect density. On the other hand, charges in the thin nanoplatelets are less effectively screened due to incomplete polaron formation. The effect of incomplete polaron formation outweighs the benefits from the passivation effect of the spacer and ligand in 2D perovskites. Instead, the interaction with traps is effective in quantum confined 2D perovskites and concomitantly decreases charge carrier mobility.

In-Plane Transport: Under a simple effective mass approximation, the confined gap is inversely proportional to the square of the dimensions of the 3D region (l_x , l_y , and l_z).^[148,149] Since perovskite NPLs have $l_z \ll l_x, l_y$, the energy gap is controlled by the lowest dimension and charges/excitons become quantum confined in only one direction, z . In addition, due to the significant difference in dielectric constant between perovskite and organic spacer, perovskite nanoplatelets exhibit a 2D quantum well structure. Therefore, charge carriers and excitons in perovskite NPLs are free to propagate in the x and y -directions, but not in

the *z*-direction. In other words, the transport of charge carriers and excitons in 2D NPLs are generally in-plane.^[230] Over the last couple of years, several groups have carried out time-resolved microscopy studies on the 2D perovskite flakes. Both transient absorption microscopy (TAM) and transient photoluminescence microscopy (tr-PLM) are sensitive more to the lateral motion of carriers than vertical motion (Figure 13f).^[225,230–234] These studies successfully imaged the in-plane motion of charge carriers/excitons and reported the diffusivities for a series of 2D perovskite, including NPLs.

A systematic study to unravel the dependence of exciton diffusion on quantum well thickness was carried out by Deng et al. using TAM on $(\text{BA})_2(\text{MA})_{n-1}\text{Pb}_n\text{I}_{3n+1}$, with *n* ranging from 1 to 5.^[225] As evidenced by blue shifts in the absorption and photoluminescence spectra, the quantum confinement along the out-of-plane direction becomes enhanced as the value of *n* was decreased. The exciton diffusivities were found to decrease from 0.34 to 0.06 cm² s⁻¹ as the quantum well thickness was decreased (Table 3). The reduced diffusion constants originate from the high defect density, more frequent scattering events, and concomitantly increased scattering rates for 2D perovskite with smaller *n*, since the diffusion constant in the band transport picture is proportional to the momentum relaxation time (τ_p).^[235] Later, Seitz et al. studied the role of the organic spacer on exciton diffusion dynamics in a series of single-crystalline perovskite flakes (*n* = 1) by performing tr-PLM measurements.^[231] They showed the positive correlation between the diffusivity and the lattice softness for 2D perovskite nanoplatelets with a wide range of organic spacers (4-fluoro-phenethylammonium (4FPEA), PEA, hexylammonium (HA), octylammonium (OA), decylammonium (DA), BA) (Figure 13g). Aromatic spacers such as 4FPEA and PEA form extensive networks due to rich pi-electrons and their space-filling nature whereas aliphatic spacers like HA, OA, DA, and BA are conformationally flexible. The strong network of aromatic spacers contributes to the enhanced lattice rigidity. The stiffening of the lattice reduces exciton-phonon coupling, leading to an increase in the diffusivity of 2D nanoplatelets. Xiao et al. further revealed another role of organic spacers on the diffusion dynamics of excitons in layered perovskites.^[230] Mitigation of the out-of-plane distortion of octahedra that arises by introducing organic spacer with strong interaction strength between the cation results in drastically induced the diffusivity of excitons, providing a record exciton diffusivity in layered perovskite of 1.91 cm² s⁻¹.

While the above-mentioned studies were focused on exciton dynamics, Zhao et al. showed long-range charge-carrier transport of over 2 to 5 μm in exfoliated $(\text{PEA})_2(\text{MA})_{n-1}\text{Pb}_n\text{I}_{3n+1}$ perovskite (*n* = 2, 3, and 4) single crystals.^[234] Upon local excitation at the center of the crystal, bandgap emission (BE) appears within the excitation spot at early times but disappears after a few nanoseconds. In sharp contrast, local emission (LE) was observed only at the edge of the perovskite crystal, a few micrometers away from the excitation spot over several hundreds of nanoseconds (Figure 13h). Based on this intriguing observation, they proposed a trap-mediated long-range charge carrier transport mechanism. That is, excitons generated following photoexcitation dissociate into long-lived and nonluminescent charges, e.g., free carriers. As time evolves, a trap-mediated long-distance carrier propagates over several micro-

eters. Once the carriers reach the edge site, the electrons and holes undergo radiative recombination. Luminescence occurs at the edge sites because these sites exhibit photophysical properties similar to those of 3D perovskites, owing to the loss of the spacer ligands.^[236,237] This interesting observation implies that although charge carriers in perovskite nanoplatelets propagate with similar diffusivities as excitons, they are the long-lived species and consequently exhibit long diffusion lengths exceeding several micrometers, which are comparable to the diffusion length of charge carriers in 3D perovskites.

Out-of-Plane Transport: The out-of-plane carrier transport in the layered perovskites is significantly less efficient than the in-plane carrier transport as carriers are confined along the out-of-plane direction and the organic spacer is less conductive. In fact, the charge mobility along the out-of-plane direction of 2D perovskite single crystals is on the order of 10⁻⁴ cm² V⁻¹ s⁻¹, which is nearly four orders of magnitude smaller than the in-plane mobility.^[239,240]

Owing to the anisotropic transport properties in perovskite NPLs, fine control over the preferred orientation and morphology are required for their applications in devices, i.e., gap-type (electrodes are horizontally separated by space) or sandwich-type (electrodes are vertically separated by perovskite layers).^[239] Details about how to control the preferred orientation can be found in early literature.^[241,242] In the meantime, there have been efforts to extract carriers from 2D perovskite quantum wells.^[46,243–245] One promising strategy to achieve efficient charge extraction out of 2D plane is adsorbing or attaching molecular acceptor/donor to perovskite surface. Li et al. studied the interfacial charge transfer dynamics of colloidal CsPbBr₃ NPLs at the presence of benzoquinone (BQ) or phenothiazine (PTZ).^[243] Due to the strong electronic coupling between perovskite and the adsorbed moiety, the excitons in the perovskite undergo efficient charge separation at the interface and the electron (hole) transfers to the adsorbed BQ (PTZ). The electron (hole) transfer time (i.e., 248 ps for electron and 670 ps for hole) to BQ (PTZ) is found to be similar to that in CsPbBr₃ quantum dots. On the contrary, the charge-separated state of NPLs is much longer-lived than those of quantum dots. Although what the cause is such a long-lived state is rather unclear, it is an important observation because suggests that the colloidal NPLs are promising materials for photocatalysis and solar cell applications due to the long-lived states. Similarly, to overcome the high exciton binding energy and extract the electrons from NPLs, Gélvez-Rueda and co-workers have attached conjugated organic chromophores (perylene diimide, PDI) to CsPbBr₃ NPLs, as shown in **Figure 14**.^[244] Figure 14a,b demonstrated the time-resolved PL spectrum for the NPLs without and with PDI respectively. The PL decay in the NPLs lives beyond 1800 ps with pristine NPLs (Figure 14a). After attaching the PDI chromophores, the shape of the fluorescence spectrum remains the same but the lifetime is strongly reduced to ≈16 ps (Figure 14b). This suggests that the excitons in the NPLs decay rapidly by electron transfer to the electron-accepting PDIs. Furthermore, they demonstrated that when pumping with a 400 nm laser, the charge transfer (Electron transfer, ET) from NPLs to PDI proceeds with a time constant (τ_{ET}) of 12.6 ps, followed by a decay from this charge separation state (CS) to ground state (GS) with a charge recombination time constant

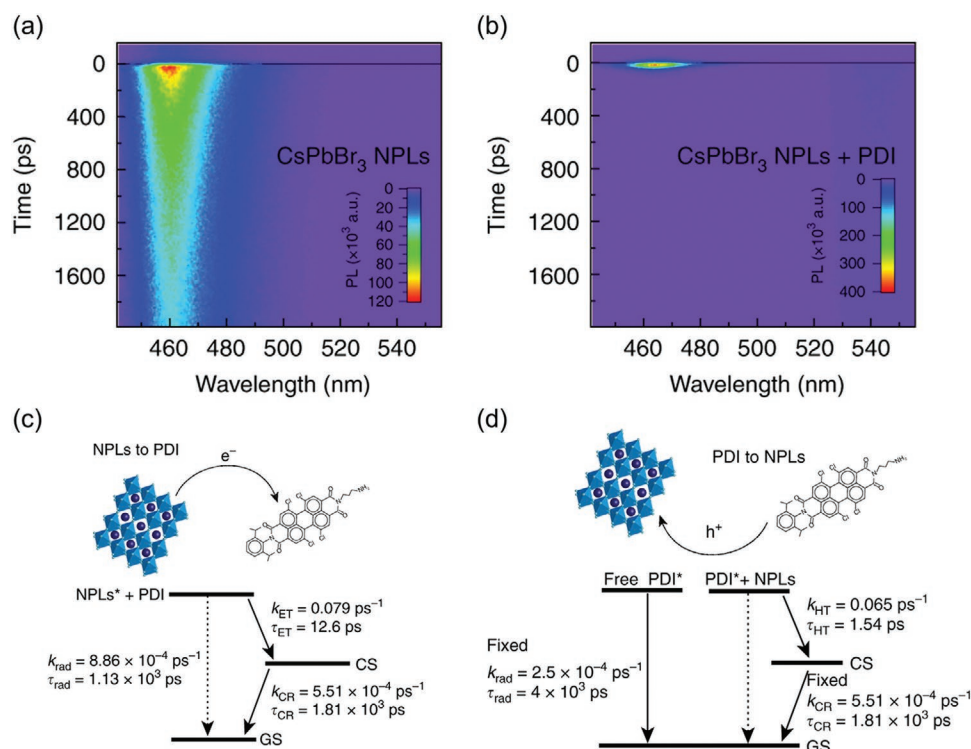


Figure 14. Picosecond photoluminescence measurements on photoexcitation at 400 nm. a) Photoluminescence (PL) of CsPbBr₃ NPLs as a function of time and wavelength. b) PL of CsPbBr₃ NPLs + perylene diimide chromophores (PDI) hybrid as a function of time and wavelength. c) Electron transfer (ET) from CsPbBr₃ nanoplatelets to PDI chromophores upon exciting at 400 nm. Kinetic model used for the target global analysis for electron transfer (ET) from NPLs to the PDI molecules in CsPbBr₃ NPLs + PDI hybrid, fitting is performed based on 400 nm pump transient absorption measurement. d) Hole transfer (HT) from PDI chromophores to CsPbBr₃ nanoplatelets upon exciting at 510 nm. The kinetic model used for the target global analysis for hole transfer (HT) from PDI chromophores to NPLs in CsPbBr₃ NPLs + PDI hybrid. The ratio of attached PDI versus PDI in solution was fitted to be 4:6. Reproduced under CC BY license.^[244] Copyright 2020, The Author(s). Published by Springer Nature.

(τ_{CR}) of 1800 ps (electron transfer and charge decay model is shown in Figure 14c). In contrast, when exciting with a 510 nm laser, hole transfer (HT) from PDI to NPLs is observed. The corresponding time constant for the hole transfer (τ_{HT}) is 1.54 ps and charge recombination (τ_{CR}) is 1800 ps respectively. This demonstrated that by selectively exciting the NPLs-chromophores composites, strongly binding electrons or holes can also be selectively extracted or injected into the NPLs, which could then influence the photoconductive of the films.^[244]

While the mechanism of out-of-plane motion has been rarely reported, Yin et al. recently reported an interesting observation on charge transfer between quantum wells that overcome the energetic barrier formed by the insulating ligands.^[245] Inspired by the previous work of Traore et al., which showed the relationship between the energy barrier for electrons (i.e., the energy difference between the LUMO of organic ligands and conduction band edge of the perovskite well) and bandgap energy upon the variation of ligand lengths, they scrutinized the series of (C_mH_{2m+1}NH₃)₂PbI₄ 2D layered perovskite single crystals with $m = 8, 10, 12,$ and 18 .^[238] In the case of $m = 12$ and 18 , the energy barrier becomes close to the bandgap energy. The AR of excitons can pump the electron into another exciton and the electron energetically jumps to the lowest unoccupied molecular orbital (LUMO) level of the ligands and subsequently transfer to the adjacent quantum wells (Figure 13i). On the other hand, in the case of $m = 8$ and 10 , the Auger process cannot pro-

vide enough energy to overcome the energy barrier with the ligands, resulting in no transfer between quantum wells. This intriguing observation on the Auger-assisted electron transfer mechanism will provide a new way to design layered 2D perovskites including colloidal nanoplatelets with improved inter-layer charge mobility and optically tunable QCSE, which are essential to advance their further application in photoelectronic and optical modulation devices.

4. Colloidal Perovskite Nanoplatelet Light-Emitting Diodes

4.1. Compositional and Dimensional Engineering

Perovskite-based light-emitting diodes (PeLEDs) have gained tremendous attention since they were first reported by Tan et al.^[223] PeLEDs could lead to the next generation of low-cost and high-performance LEDs for display, lighting, and optical communication applications.^[246–248] Although green and near-infrared PeLEDs have achieved external quantum efficiencies (EQEs) higher than 20%,^[249–251] there are still challenges with fabricating spectrally stable and highly efficient pure red and blue PeLEDs, particularly for devices that emit with Commission Internationale de l'éclairage (CIE) coordinates approaching the Rec. 2020 specified red (0.708, 0.292) and blue (0.131, 0.046)

colors that are required for ultrahigh-definition displays (in addition to the green emitters that are easier to achieve).^[252] In this section, different methods of preparing pure red and blue perovskite emitters will be discussed, with particular emphasis on utilizing perovskite NPLs as a route to achieving high PLQY and spectrally stable LEDs. These are compared to bulk 3D perovskite thin films and perovskite nanocubes.

4.1.1. Compositional Engineering with Bulk 3D and Weakly Confined Nanocrystals

One method to fabricate pure-red and blue perovskite emitters is through compositional engineering, by mixing bromide and iodide together for red emitters,^[249,253,254] or bromide and chloride for blue emitters.^[254–256] Bulk 3D perovskite blue emitters with a mix of Br and Cl were first achieved by Kumawat et al. in 2015.^[255] They successfully fabricated $\text{MAPbBr}_{3-x}\text{Cl}_x$ based blue PeLEDs with an emission peak center at 482 nm, a brightness of 2 cd m⁻² and a low EQE of 0.0001% when the Cl to Br atomic ratio was 1.92:1.08. One of the challenges of producing high-performance bulk Br–Cl mixed perovskite blue emitters is the high levels of nonradiative recombination. The reported efficiencies in other early works on blue PeLEDs based on bulk 3D perovskite were also low. For example, Yuan et al. reported 2.01% EQE for sky-blue emitters in 2017 and Wang et al. reported 0.062% for pure-blue emitters in 2019.^[257–259] Many efforts have been made to improve bulk blue PeLEDs, such as through doping or defect passivation.^{[256,260,261][262]} Often defect passivation, particularly of surfaces, is achieved using long-chain organic ligands. Similarly, in LHP NCs, the surfaces are effectively passivated with coordinating ligands, as well as through many other strategies, as discussed in the synthesis section. As a result, LHP NCs have achieved near-unity PLQY, making them highly promising for PeLED applications.^[15,263,264] For example, Chiba et al. illustrated that by mixing bromide and iodide anions, a red PeLED emitting at 649 nm can be achieved with an EQE of 21.3% and CIE coordinates of (0.72, 0.28).^[249]

However, the almost unavoidable drawback of blue-shifting the emission of perovskites by mixing halides is the spectral instability associated with halide migration under the application of an electric field. A redshift in the position of PL or electroluminescence (EL) peak and a broadening of the peak FWHM are commonly observed under illumination or bias.^[265] For instance, Li et al. observed a redshift in the EL spectrum of red $\text{CsPbBr}_{0.75}\text{I}_{2.25}$ and blue $\text{CsPbBr}_{1.5}\text{Cl}_{1.5}$ NC PeLEDs over time at a constant operating voltage of 3.5 V.^[254] The origin of the spectral instability is attributed to anion segregation in the mixed halide perovskite emitters.^[253,266] The halide segregation is highly dependent on factors such as chemical potential gradient, thermal gradient, applied electric field, and the photon flux and frequency of the incident light. Three well-established models have been put forward in the literature to account for phase-separation: 1) a thermodynamic model that is related to surface halide defect density; 2) a model in which polaron-induced lattice strain provides the driving force for halide anion migration; 3) a model in which charge-carrier gradients and localized electric fields trigger the movement of halides.^[267] Knight and Herz^[266] reviewed methods to mediate the anion

segregation effect in halide perovskite films, such as stoichiometric A-site and B-site engineering, halide defects and distribution management and crystallinity control.^[266] Although compositional engineering was the initial strategy to blue-shift the bandgap and emission wavelength of perovskite emitters, it also led to higher densities of deep defect states, which compromise the PLQY of the film, and ultimately device performance and stability. While many groups have worked on addressing these limitations by controlling defect density, an alternative approach is starting to use dimensional engineering for controlling the bandgap.

4.1.2. Dimensional Engineering: Quasi-2D versus Colloidal Nanoplatelets

In contrast to compositional engineering, low dimensional perovskites provide an alternative route to achieve spectrally stable devices with desirable color emission coordinates. As discussed in earlier sections, low-dimensional perovskites include quasi-2D perovskites,^[268–272] strongly quantum confined quantum dots,^[273] and colloidal perovskite NPLs. The key difference between quasi-2D and colloidal perovskite NPLs is the types of insulating layers used, i.e., spacers or ligands. While spacers separate inorganic layers or lead-halide octahedra (thus determining the *n*-values of quasi-2D perovskites), ligands passivate surfaces and determine the size of NPLs, i.e., thickness and lateral dimensions. Therefore, the adequate use of different organic compounds during synthesis will give the desired optical properties for colloidal perovskite NPLs. The progress of quasi-2D perovskites in PeLEDs can be found in other reviews.^[274,275] Despite the advantages of using large organic molecules, such as improving PLQY and stability, quasi-2D perovskites have several disadvantages. For example, as discussed in Section 3, charge transport in quasi-2D perovskite films becomes anisotropic and highly restricted in the out-of-plane direction, due to the insulating nature of the large organic cation spacers. Changes in the spacer would lead to changes in the optical properties, such as bandgaps and exciton binding energies. Also, the spacer cations tend to decompose under high applied biases or long operation times in PeLEDs, which is detrimental to the device stability.^[276] On the other hand, colloidal perovskite NPLs contain well-defined ligands on the surface, in which charge transport properties can be controlled by tuning the length of the ligands without compromising on the size of the NPLs.^[24,277–279]

Since NPLs can achieve blue or red emission with a single halide composition, they do not suffer from the phase separation issue faced by mixed halide perovskites, this is conducive toward achieving spectrally stable emission that does not broaden or red-shift over time, several challenges need to be overcome first.^[84,105,112,115,280] For example, Wang et al. observed that CsPbBr_3 NPLs aggregate to form a bulk phase under exposure from low UV irradiation (20 mW cm⁻²).^[112] The merging of NPLs under UV-irradiation leads to a red-shift in the emission spectrum, from 436 nm (3 monolayers) to, 466 nm (6 monolayers), 484 nm (9 monolayers) and 521 nm (bulk) gradually. The trigger of the merging is attributed to the desorption of liable surface ligands and hence leading to

self-assembly of the NPLs like a lamellar stacking.^[115,112] Apart from photon-induced phase transformation, NPLs can undergo rapid aggregation when excess thermal energy is supplied.^[280] Dang et al.^[280] reported that colloidal CsPbBr₃ NPLs would first undergo surface ligand detachment and merge to form nanobelts, then the nanobelts would join with the neighboring nanobelts to form extended nanosheets, resulting in the PL red-shifting over time (22 d) from 460 to 515 nm. This merging process can accelerate if external thermal energy is supplied. For example, the time taken for the PL to red-shift to 515 nm is only 40 min at 110 °C.^[280] Joule heating would be present during LED device operation, and this can therefore accelerate NPL agglomeration. To mitigate photon-induced and thermally-induced aggregation, ligands that can be tightly bound to the surface of the NPLs can be used. For example, Shamsi et al. replaced the OLA ligands with short hexylphosphonate ligands (C₆H₁₅O₃P) which are more tightly bound to the surface.^[84] As a result, the NPLs can be preserved for months with the same PL peak position. Therefore, exploring alternative ligands would be a possible method to further improve the PL/EL stability for NPLs based LEDs.

4.2. Strategies to Improve Colloidal Perovskite Nanoplatelets LED Performance

The progress of colloidal perovskite NPL LEDs is illustrated in **Table 4** and **Figure 15a**. The EQE of pure-green-emitting bromide-based perovskite NPLs (with >7 monolayers) has increased from 0.48% in 2016^[283] to 23.6% in 2020.^[284] For blue PeLEDs (465–485 nm emission wavelength), the efficiency has improved from <0.1%^[29] to 1.42%.^[282] So far, the most commonly used structure for perovskite NPL LEDs is ITO/PEDOT:PSS/NPL/TPBi/electrodes. **Figure 16** provides insights into the strategies for improving NPL PeLED performance. The EQE of LED devices is influenced by four main factors: 1) the percentage of radiative recombination among all recombination processes in the emitter layer (PLQY); 2) the probability of balanced charge injection (f_{balance}); 3) the chance of effective electron–hole coupling ($f_{\text{e-h}}$); and 4) the fraction of photons generated that are emitted out of the device ($f_{\text{outcoupling}}$).^[285] The influence of each factor on the performance of NPL PeLEDs is discussed below.

Table 4. Performance list colloidal nanoplatelets PeLEDs.

Year	Key advance	EL peak [nm]	EQE [%]	FWHM [nm]	Turn-on voltage [V] ^{b)}	Refs.
2016	MAPbBr ₃ NPLs; first report of hybrid organic–inorganic halide perovskite NPLs LEDs	529	0.48	20	3.8	[283]
2016	MAPbBr ₃ NPLs (CBP) ^{a)} -perovskite NPLs (<i>n</i> = 3) composite film	456	0.23	20	3.5	[316]
2016	MAPbBr ₃ NPLs (CBP)-perovskite NPLs (<i>n</i> = 7) composite film	530	2.31	20	3.5	[316]
2017	CsPbBr ₃ NPLs controlled thickness <i>n</i> = 12–16	514	10.4	17	2.8	[317]
2017	CsPb ₂ Br ₅ NPLs perovskite inspired Material	520	NA	20	3	[318]
2017	FAPbBr ₃ NPLs PMMA-perovskite thin film composite	530	3.04	22.6	2.75	[281]
2018	CsPbBr ₃ NPLs large scale production	480	0.1	35	3	[319]
2018	CsPbBr ₃ NPLs PbBr ₂ passivation	464	0.057	20	3.8	[29]
2018	CsPbBr ₃ NPLs in situ passivation with HBr	463	0.124	12	3.5	[53]
2019	CsPbBr ₃ NPLs Poly-TPD band alignment (blue)	464	0.3	16	4	[123]
2019	CsPbBr ₃ NPLs Poly TPD band alignment (sky-blue)	489	0.55	26	4	[123]
2019	CsPbBr ₃ NPLs DDAB-ligand treatment	469	1.42	40	3.6	[282]
2019	FAPbBr ₃ NPLs FA-based NPLss	532	3.53	NA	NA	[95]
2020	FAPbBr ₃ NPLs TOPO-NPLs for deep-blue emission	439	0.14	14	3.6	[96]
2020	CsPbBr ₃ NPLs transition dipole moment orientation control	518	23.6	16	3	[284]
2021	CsPbBr ₃ NPLs PEI modified (increasing luminescence(cd m ⁻²))	465	0.8	19.5	2.6	[320]
2021	K-Br passivated CsPbBr ₃ NPLs white LED with CsPbBr ₃ and CsPbBr _{1.5} I _{1.5} as green and red phosphor	White	–	–	NA	[117]

^{a)}CBP is 4,4'-bis[9-dicarbazolyl]-2,2'-biphenyl; ^{b)}Turn-on voltage is obtained from the current-voltage curve.

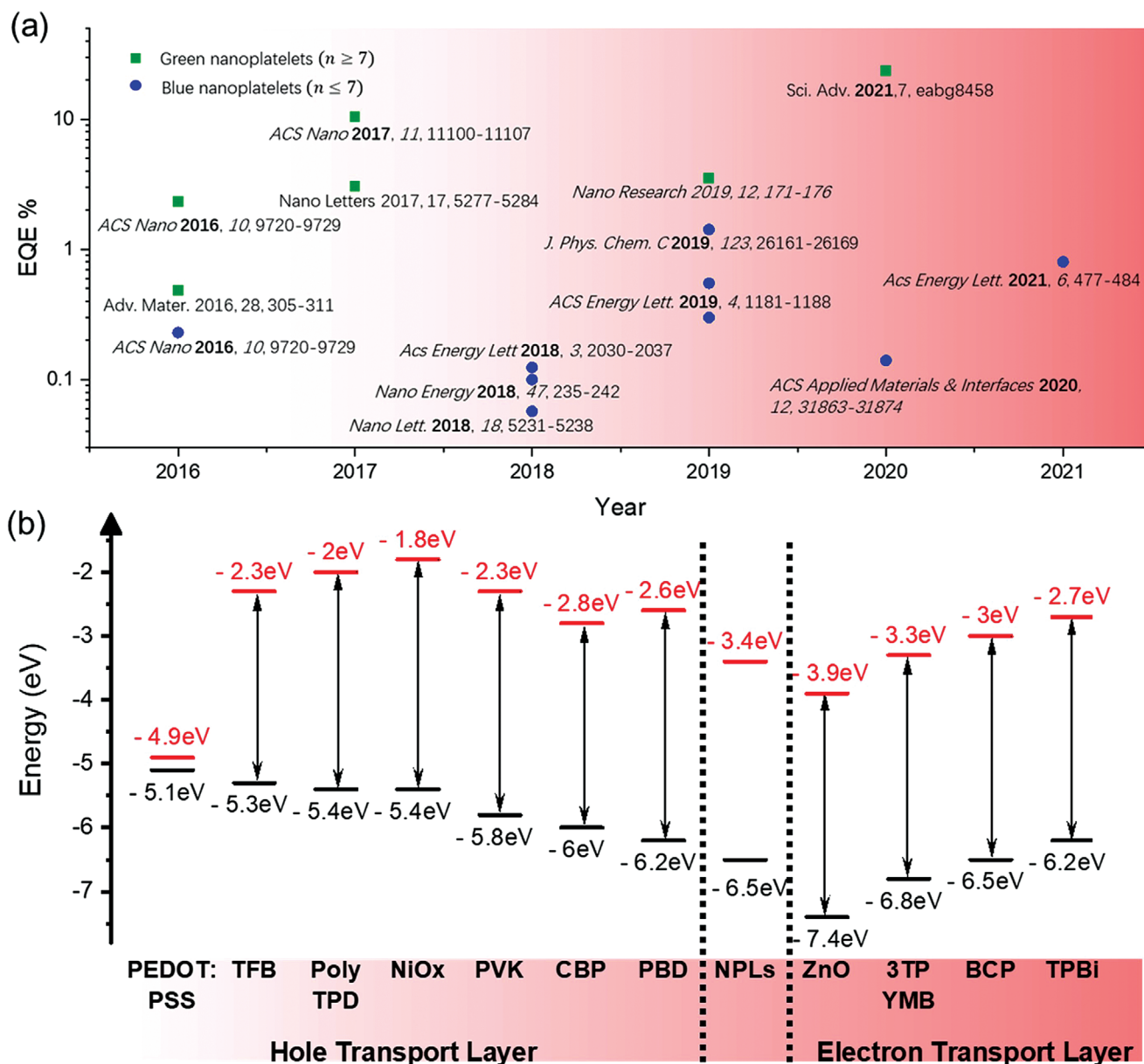


Figure 15. Perovskite nanoplatelet (NPI) light-emitting diodes (LEDs). a) Development of perovskite NPI LEDs over time. b) Valence and conduction band extrema (or LUMO and HOMO levels for organic materials) of the reported hole and electron transport layer in perovskite nanoplatelet LEDs. Band positions of transport layers^[286] and perovskite NPLs (-3.4 to -6.5 eV)^[96] obtained from the literature. The NPLs band position depends on the number of monolayers, the graphic value is based on the monolayer of Br-based NPLs.

4.2.1. Internal Quantum Efficiency

One of the most important parameters for LEDs is the internal quantum efficiency or PLQY of the emitter film. It is well accepted that in a strongly quantum-confined nanoplatelet system, the PLQY depends on the competition between first-order exciton radiative recombination (k_{exciton}) and the first-order exciton trap-assisted recombination (k_{trap}) at low fluence (when carrier density, N , is small enough, usually below 10^{16} cm^{-3} or low current density, for example below 10 mA cm^{-2}) (Equation 5).^[15,247,286,287]

$$\text{PLQY} = \frac{k_{\text{exciton}} + N \cdot k_2}{k_{\text{exciton}} + k_{\text{trap}} + N \cdot k_2 + N^2 \cdot k_3} \quad (5)$$

Therefore, under the normal LED operating regime (carrier density 10^{10} – 10^{16} cm^{-3}),^[288] the trap-assisted exciton recombination rate, k_{trap} , is the factor that needs to be minimized to improve PLQY. Earlier in synthesis Section 2, it was discussed how perovskite NPLs can achieve near-unity PLQY through effective defect passivation.^[53] Previous works have highlighted the influence of defect passivation on PeLED device performance.^[15,53,117,263,289] Primary and quaternary amine,

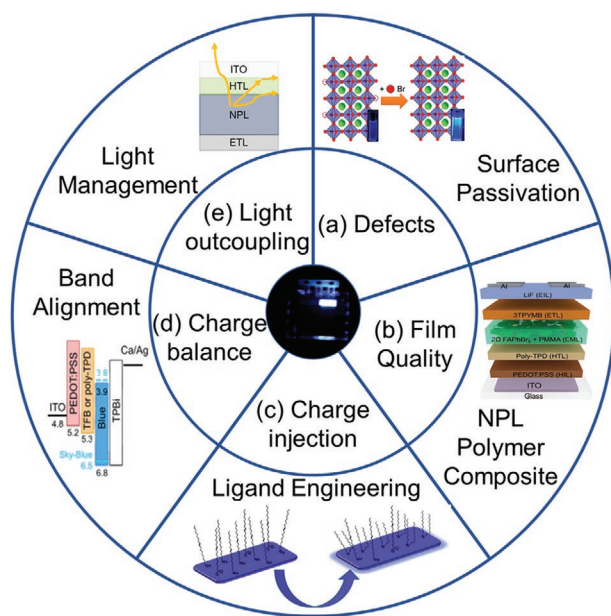


Figure 16. Factors limiting PeLED performance and strategies for overcoming these factors in NPLs PeLEDs. a) Defect passivation method: Reproduced with permission.^[53] Copyright 2018, American Chemical Society. b) Film morphology modification: Improve film morphology by making 2D FAPbBr₃ perovskite-PMMA composite film. Reproduced with permission.^[281] Copyright 2017, American Chemical Society. c) Ligand exchange method: Insert schematic illustration of the post-synthetic surface ligand exchange treatment of CsPbBr₃ NPLs. Reproduced with permission.^[282] Copyright 2019, American Chemical Society. d) Band-alignment and interfacial engineering method: Band structure of perovskite LED devices with blue or sky-blue emitters (left) without or (right) with a polymer interlayer. Reproduced under CC-BY license.^[123] Copyright 2019, American Chemical Society. e) Maximizing light outcoupling efficiency.

phosphonic and sulfonic acid, zwitterions, and inorganic salts have been found to be effective for passivating surface defects in perovskite nanocrystals.^[14,15,290–292]

For nanoplatelets, it is useful to identify the dominant type of surface traps and passivate them with appropriate ligands. To identify the surface traps present, Bertolotti et al. investigated the surface termination of CsPbBr₃ NPLs using X-ray total scattering techniques, based on the Debye scattering equation (DSE) approach.^[59] The DSE model is considered as one of the most accurate expressions to model the diffraction pattern from nanoparticle systems. The method illustrates a comprehensive characterization of the nanosized materials and full XRD pattern reconstruction, both in terms of Bragg peaks and diffuse scattering, which intrinsically arise from the detailed atomistic model definition of NPLs, developed in the real space^[293] (Equation 6).

$$I(Q) = \sum_N \sum_N f_i(Q) f_j^*(Q) \frac{\sin(Qr_{ij})}{Qr_{ij}} \quad (6)$$

where $Q = 4\pi\sin(\Theta)/\lambda$, the wavevector transfer modulus (Θ is half the scattering angle and λ the radiation wavelength), f the atomic scattering factor and r_{ij} the magnitude of the distance between any two of the N atoms composing an atomistic aggre-

gate.^[294] Based on DSE analysis of 6 monolayer CsPbBr₃ NPLs (one monolayer being ≈ 0.59 nm thick), Bertolotti et al. claimed that the NPLs exhibit an orthorhombic structure with (100) pseudocubic facets, which correspond to two (010) and four (101) planes of the orthorhombic CsPbBr₃ lattice ($Pnma$ space group). The basal facets of the N are of the (101) family, whereas two remaining (101) planes and both (010) planes make for side NPLs facets. Hence, it is suggested that CsBr-terminated surfaces are preferentially exposed, with almost half Cs sites and a half Br sites vacant.^[59] It indicates that vacancy defects would be one of the dominant non-radiative recombination pathways which reduce the PLQY.

Previous theoretical calculations have shown that the formation energy required to create vacancies CsPbBr₃ nanocrystal system is in the range of 1.4–2.3 eV, depending on the position of the vacancy in the lattice for the perovskite nanocrystal system.^[295] Brinck et al. found from computations that the defect formation energy for a charged or neutral Br vacancy tends to be lower than the defect formation energy for a Cs vacancy or a Pb vacancy (calculated defect formation energies in CsPbBr₃ NCs can be found in **Figure 17**).^[295] Br vacancies are therefore more common. Hence, the passivation of Br-based NPLs has focused on eliminating or minimizing halide vacancies to improve their performance in PeLEDs.^[29,53] For example, Wu et al. proposed an in situ passivation method by adding excess Br⁻ (HBr) to form an interconnected Pb-Br octahedral framework before nucleation which could significantly reduce the density of bromide vacancies in the NPLs (Figure 16a).^[53] As a result, the PLQY of the NPLs increased from 18% (pristine NPLs) to 96% (passivated NPLs), and the average carrier lifetime measured by transient absorption increased from 3.96 ns to 6.46 ns with a pump intensity of 1.25 $\mu\text{J cm}^{-2}$ (2s.f.).

Apart from passivating the bulk material, passivating defects at interfaces between the perovskite layers and charge-injecting layers is also important. For example, Hoyer et al. reported by adding an extra poly-TPD layer between the conventional PEDOT:PSS hole-injection layer and CsPbBr₃ NPLs emitter, the EQE of the blue PeLED could be improved from 0.007% to 0.3% (shown in Figure 16d).^[123] Poly-TPD was shown through PLQY and time-resolved photoluminescence measurements to reduce nonradiative recombination at the hole-injecting interface. Other organic passivating layers and strategies that have been effective in perovskite solar cells (e.g., PTAA) could also be applied to NPL LEDs.^[296,297] For instance, an emerging idea in the perovskite photovoltaics scene that could also be translated to the PeLED field is to use self-assembled monolayers (SAMs) to passivate the bottom interface beneath the solution-processed emitter.^[298]

Apart from suppressing trap-assisted recombination through defect passivation, reducing Auger recombination during device operation is another important factor that needs to be considered. When the injected current density is large (typically larger than 1–10 mA cm⁻² or carrier density is larger than 10¹⁶ cm⁻³), LEDs will suffer from significant efficiency roll-off when the injected charge carrier density is high (**Figure 18**). The origin of the efficiency roll-off in colloidal NPLs systems has not yet been studied. For quantum-confined systems, such as quasi-2D perovskite thin films (Figure 18a,b) and 2D NPLs (Figure 17c), an explanation that has been put forward is Auger recombination,

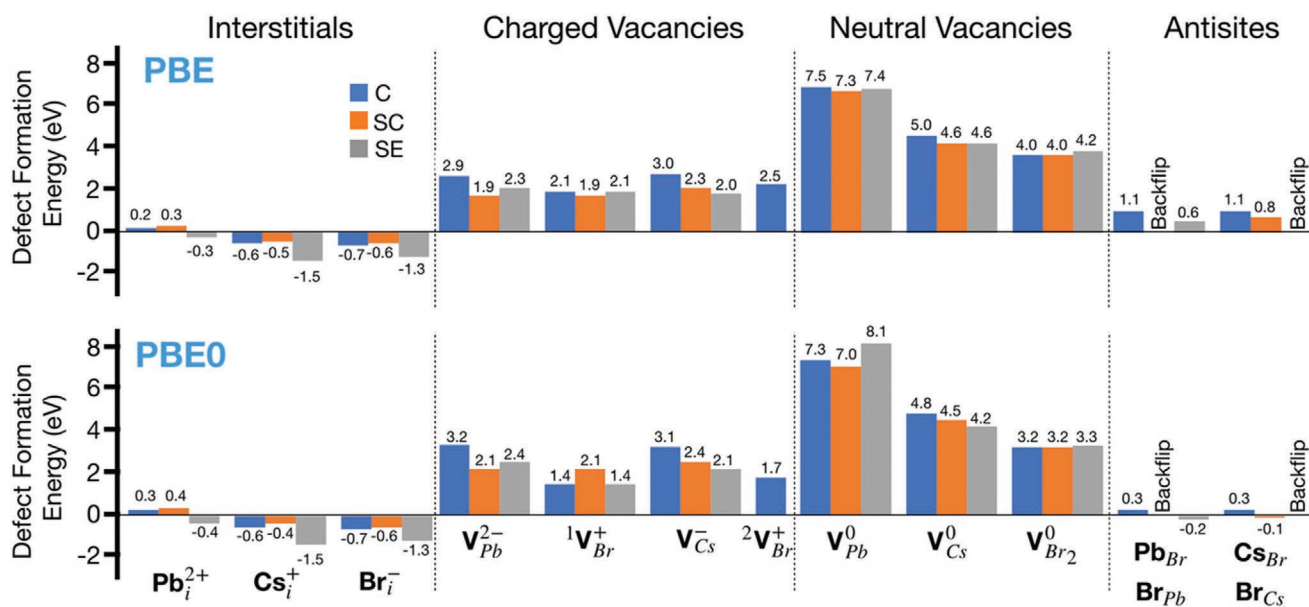


Figure 17. Defect formation energies (DFEs) associated with interstitial, charged, neutral vacancies, and antisite substitutions listed in electronvolts. The DFEs are computed following geometry optimizations carried out at the DFT/PBE0 level of theory. Backflip means that the antisite displacement goes back to its initial non-defective configuration. Note that here we report only the defect name without the counterion. C, SC, and SE are defects at core/surface, surface-center/surface and surface-edge/surface, respectively. Reproduced with permission under CC-BY-NC-ND license.^[295] Copyright 2019, American Chemical Society.

which is also a three-body non-radiative recombination pathway that lowers the PLQY (refer to Section 3).^[287,299,300] Another cause would be exciton-exciton annihilation, as discussed earlier in the carrier dynamics section. When increasing the excitation carrier density, radiative bimolecular recombination gradually dominates over the monomolecular process, so the PLQY would increase initially with the current density as shown in Figure 18b for a quasi-2D system. At higher carrier densities, three-body Auger recombination becomes dominant, resulting in decreases in PLQY (Figure 18a). It is also noticed that in a quasi-2D or colloidal 2D system, the k_{exciton} is proportional to the exciton binding energy E_b in quantum wells.^[287] For instance, Philbin et al. illustrated that Auger recombination lifetimes depend nearly linearly on the lateral area and somewhat more strongly on the thickness of the nanoplatelets.^[301] Therefore, developing a facile approach to manage Auger recombination would be critical to reducing efficiency roll-off in 2D perovskite LEDs.

4.2.2. Charge Injection and Charge Balance

Charge injection and charge balance are also critical factors for device performance. It strongly depends on the film quality of the NPL emissive layer. Incomplete film coverage (pinholes) would lead to current leakage, charge imbalance, and carrier quenching at interfaces.^[302] Kumar et al. mixed FAPbBr₃ NPLs with PMMA solution to improve the film quality (Figure 16b).^[281] By adding PMMA, the emitting film became more uniform, and the root-mean-square roughness decreased from 7.91 to 0.63 nm. Furthermore, the presence of PMMA molecules around the FAPbBr₃ NPLs altered the surrounding

dielectric constant, leading to an increase in the exciton binding energy (increased from 149.3 to 161.3 meV) through dielectric confinement.^[303] The increase in exciton binding energy led to an increase in the PLQY (from 88% (solution) to 92% (composite film)) because the more tightly bonded excitons could undergo monomolecular radiative recombination rather than dissociating into free carriers which are more easily trapped by defects. As the result of improved film coverage and PLQY, the device EQE increased from 1.14% (0 wt% PMMA) to 3.04% (8 wt% PMMA).^[281]

Another challenge for effective and balanced charge injection in NPL PeLEDs arises from the long-chain ligands (usually oleylamine and oleic acid) that are present at the surface of NPLs. These long-chain ligands are needed in order to control the growth of the nanoplatelets, prevent agglomeration and passivate surfaces. On the other hand, these ligands limit charge injection. An appropriate ligand management method is needed to balance the need for high PLQY versus efficient charge injection.^[279,304] Kumar et al. demonstrated that by replacing long-chain ligands (16 carbons, hexadecylamine) with shorter ligands (6 carbons, hexylamine) during the synthesis, the current density under the same injection voltage and carrier lifetime increased.^[279] This indicated that a shorter chain ligand can improve charge injection, the turn-on voltage at an operating current density of 1 mA cm⁻² decreased from 4.32 V with hexadecylamine to 3 V with hexylamine. As a result, the luminance (in cd m⁻²) of the PeLED increased when using shorter chain ligands, for instance, the luminance increased from 2.46 cd m⁻² for hexadecylamine (16 carbons), to 3322 cd m⁻² for decylamine (10 carbons) and 9555 cd m⁻² for hexylamine (6 carbons). Zhang et al. performed postsynthesis ligand engineering by exchanging long-chain OLA and OA ligands with shorter

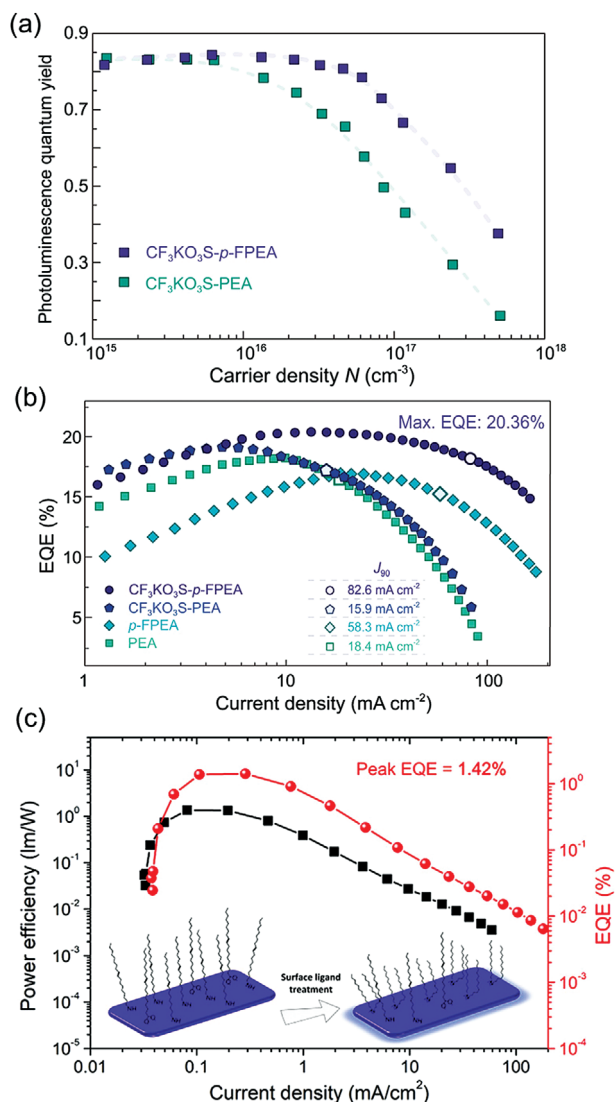


Figure 18. Demonstration of efficiency roll-off in blue PeLEDs. a) Film's PLQYs as a function of carrier density for $\text{CF}_3\text{KO}_3\text{S-PEA}$ and $\text{CF}_3\text{KO}_3\text{S-p-FPEA}$ quasi-2D films. b) Current density-dependent EQE curve for different quasi-2D PeLEDs. Reproduced under CC BY license.^[287] Copyright 2021, The Author(s). Published by Springer Nature. c) External quantum efficiency–current density curve of the treated CsPbBr_3 NPL-based LED. Reproduced with permission.^[282] Copyright 2019, American Chemical Society.

dimethylammonium bromide (DDAB) ligands (Figure 16c).^[282] After ligand treatment, the CsPbBr_3 NPL PLQY increased from 45.1% to 69.4%, as the DDAB ligands not only partially replaced the original ligands but also passivated surface defects. The shorter DDA^+ ligands also decreased NPLs spacing and led to a more delocalized wave function, contributing to decreased turn-on voltages from 6.4 to 3.6V, since the better balanced charges can be more easily injected into the NPLs, leading to the EQE increasing from 0.02% to 0.56%.^[282] Developing suitable and exchangeable ligands is still quite challenging for perovskite NPLs.^[14,24] Chen et al. reviewed feasible ligands that can exchange with the liable ligands for perovskite nanocrystals, including short-chain acid and amine ligands, and com-

plex ligands such as perylene diimide.^[24] However, no studies yet have been done on how the ligand exchange process would affect the size, shape, and optical properties of the NPLs.

Interfacial engineering is another important area to improve charge injection and balance, as well as reducing interfacial PL quenching.^{[123][305]} For a commonly used PeLED structure (ITO/PEDOT:PSS/NPLs/TPBi/LiF/Al), the energy discrepancy between the work function of the anode (usually LiF/Al, -2.9 eV) and the LUMO of the electron injecting layer (TPBi, -2.7 eV) (Figure 15b) is negligible. There is almost no energy barrier for electron injection from the cathode into the conduction band minimum (CBM) of the perovskite NPLs (around -3 eV). However, on the anode side, there is a significant energy barrier between the transparent ITO (work function -4.7eV) and the perovskite valence band maximum (VBM) (around -6 to -7 eV). The large energy difference makes it more difficult for hole injection, resulting in higher electron current densities, with electrons accumulating at the hole injection interface with the emitter. One solution would be to introduce a multilayer HTL with cascade-type energy levels. For blue PeLEDs, researchers now tend to use the first hole transport layer that has high hole mobility and can form a quasi-Ohmic contact with the ITOs, such as NiO_x and PEDOT:PSS. Then a second hole transport layer with deeper HOMO is used to form cascade-type energy levels to improve hole injection and charge balance, for example, poly-TPDs (Poly[N,N'-bis(4-butylphenyl)-N,N'-bis(phenyl)-benzidine]), TFB (Poly(9,9-dioctylfluorene-alt-N-(4-sec-butylphenyl)-diphenylamine)) and PVK (poly(9-vinylcarbazole)).^[306,307] However, the role of these layers is still unclear, whether they form an energy cascade to facilitate charge injection or passivating interfacial defects to reduce PL quenching, or that they improve the surface roughness and uniformity of the top perovskite layers.

4.2.3. Formation of Electron–Hole Pairs (Excitons)

Electroluminescence is generated when injected electrons and holes are effectively correlated to each other and radiatively recombine, such as through the formation of excitons.^[15,308] The exciton binding energy (E_b) then becomes an important parameter to determine the equilibrium population of excitons (n_x) and unbound carriers (holes (n_h) and electrons (n_e)).^[308] The formation of excitons from free electrons and holes, and the reverse process (i.e., dissociation into free charges), can be seen as a chemical reaction between these three species. The equilibrium populations of these species depend on their overall concentration. With increased optical (or electrical) excitation, the pairing of electrons and holes to form bound neutral states becomes more favored and excitons thus become the dominant species. Conversely, at low injection levels, unbound electrons and holes are unlikely to meet and to give rise to excitons, which therefore are the minority species. The Saha equation (Equation 7) is normally used to describe the equilibrium between free electrons/holes and excitons:

$$n_e n_h = n_x n_{\text{equilibrium}} \quad (7)$$

$$n_{\text{equilibrium}} = \left(\frac{\mu_x k_B T}{2\pi h^2} \right)^{\frac{3}{2}} e^{-\frac{E_b}{k_B T}} \quad (8)$$

In Equations 7 and 8, n_x , n_h and n_e are the exciton, hole, and electron populations, respectively, $n_{\text{equilibrium}}$ is the equilibrium constant, which is determined by temperature (T) and the exciton binding energy (E_b), μ_x is the reduced exciton mass. $n_{\text{equilibrium}}$ is typically on the order of 10^{17} , 10^{16} , and 10^{16} cm^{-3} for bulk MAPbI_3 , MAPbBr_3 , and MAPbCl_3 , respectively.^[308] Typically, for a 2D exciton-dominant system, the emitted light intensity should have a linear relationship with moderate carrier injection intensity (injected carrier density 10^{16} – 10^{19} cm^{-3}) since the exciton is the dominant species for light emission in NPLs.^[309] However, there is still a lack of fundamental studies about how excitons and free carriers are generated during the operation of NPL-based LED devices.

4.2.4. Outcoupling

Typically, the perovskite layers have a much larger refractive index (n , typically 2.1–2.6) than the surrounding materials, for example, the glass substrate ($n = 1.5$), ITO ($n = 1.8$), commonly used organic transport layers (e.g., TPBi) ($n = 1.73$) and air ($n = 1$).^[286,310] Light will only propagate from a higher-refractive-index material (i.e., perovskites) to a lower-refractive-index material (i.e., air) when the incident angle is larger than the critical angle. As a result, the majority of electroluminescence from PeLEDs would undergo Fresnel reflection and waveguiding within the glass substrate. The light loss mechanisms include parasitic absorption by adjacent layers, longitudinal oscillation of electrons at metal interfaces (surface plasmon polariton), waveguide mode which traps the light between ETL, HTL layers, and ITO glasses.^[310] Zhang et al. conducted a detailed review on light outcoupling management in PeLEDs,^[310] here we would like to discuss the intrinsic light outcoupling in perovskite NPLs.

The large discrepancy between the intrinsic perovskite light outcoupling efficiency and the organic counterparts is due

to the random orientation of the transition dipole moments (TDMs) in perovskite NPLs.^[311] Currently, there is a lack of methods to align the TDMs in perovskites, in contrast to organic emitters. In organic emitters, the alignment of TDMs can be tailored by designing the molecular structure, which can influence the intermolecular interactions, including van der Waals (vdW) and electrostatic forces, and thermodynamically determine the molecular configuration and conformation of the emitters. The orientation of the molecules can be also be tuned through the processing.^[312] However, these methods are far more difficult to apply with perovskite emitters. It is worth noting that the TDMs that are horizontally aligned with respect to the electrode interface are favored for light outcoupling while the vertically aligned TDMs largely contribute to energy losses due to waveguiding.^[313] Therefore, to increase outcoupling, maximizing the horizontally oriented TDMs is preferred. Jurow et al. reported a method to change the orientation of the average TDMs by reducing the dimensions of the nanocrystals and depositing them face down onto a substrate by spin coating at 1500 rpm in toluene on glass substrates to a create monolayer of NPLs.^[311] The percentage of horizontal TDMs can be measured in the setup shown in **Figure 19a**. Recently, Cui et al.^[314] and Kumar et al.^[315] illustrated that self-assembled 2D perovskite NPLs could exhibit a higher outcoupling efficiency as the orientation of TDMs are well aligned in the spin-coated NPLs films. For example, Cui et al. estimated the ratio of horizontal TDMs, Θ_H , in their anisotropic NPLs films is 84% based on the angle-dependent PL measurement, which provides an ensemble measurement of the intensity of p-polarized emission against the detection angle.^[314] The Θ_H value in NPLs film (84%) is larger than the Θ_H value in isotropic emitters (67%), and it leads to an increase in simulated device outcoupling efficiency from 23.4% (isotropic emitters) to 31.1% (anisotropic emitters). As a result, they achieved a green PeLED with an EQE of 23.6%. Similar results were also achieved by Kumar's group, with a Θ_H value of 72% (Figure 19b) in the optimized mixed cation NPLs, and a device efficiency of 24.2%.^[315] These pioneering works provide excellent guidance for measuring and orienting the TDMs in low dimensional halide perovskites.

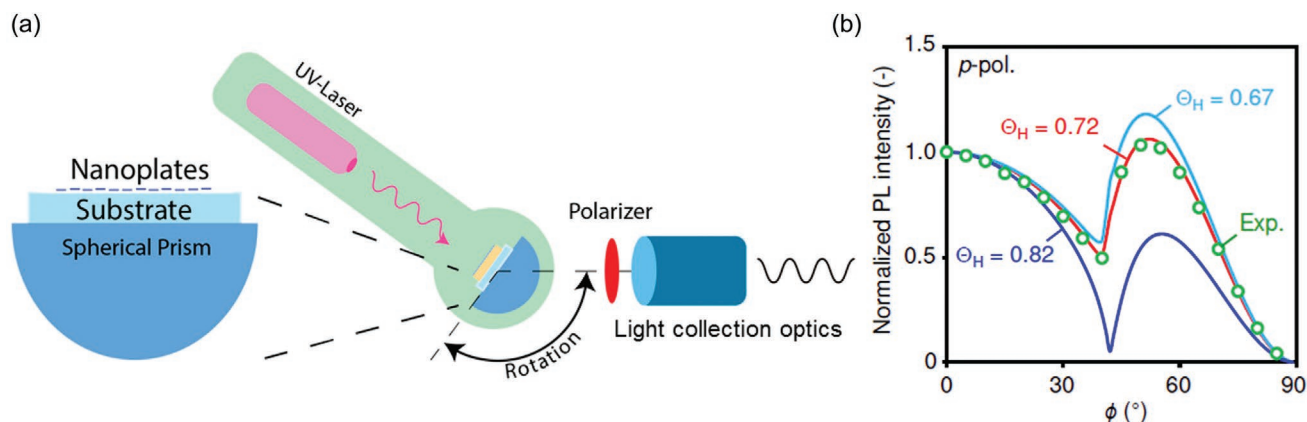


Figure 19. Quantify horizontal TDMs in perovskite films. a) Schematic of a film of perovskite nanoplates on a spherical prism to analyze the emitted light and calculate the average orientation factor (Θ_H) of the material at each wavelength. Reproduced with permission.^[311] Copyright 2019, American Chemical Society. b) Experimental and calculated thin-film p-polarized PL intensity as a function of viewing angle Φ , using the thin-film horizontal dipole ratio Θ_H as the control parameter. Reproduced under CC BY 4.0 license.^[315] Copyright 2021, The Author(s). Published by Research Square.

5. Future Prospects

5.1. Synthesis

Despite great progress in the thickness-controlled synthesis of halide perovskite NPLs, it is still challenging to achieve monodisperse NPLs with a single PL peak for all possible thicknesses. Generally, the PL spectra of NPLs contain one or more small shoulder peaks arising from different thicknesses, and it is extremely difficult to separate them into individual thicknesses. In addition, most of the reported studies are focused on bromide-based lead perovskite NPLs with different A-site cations, while iodide perovskite NPLs have rarely been investigated. It is a great challenge for researchers to obtain iodide-based perovskite NPLs with controllable thicknesses. For instance, Huang et al.^[56] demonstrated the shape and thickness tunability of FAPbI₃ NPLs by varying the ratio of Cs to Pb in the precursor solution. However, the level of thickness control demonstrated was still far from what has been achieved with bromide-based perovskites.^[29,31,63,81] In fact, in Table 2, one can see that the lead halide perovskite NPLs with different A-site cations and thicknesses still need to be explored. On the other hand, thickness-controlled Pb-free perovskite NPLs and their properties have been rarely reported due to the difficulties associated with their synthesis. Therefore, there is great room for researchers in this direction. For example, the change in the dimensionality of Cs₂AgBiBr₆ double perovskites from 3D (bulk) to 2D (1 ML) is expected to transform the nature of its bandgap from indirect to direct,^[321] however, colloidal monolayer double perovskites have not yet been reported. Furthermore, controlling the lateral dimensions of perovskite NPLs is challenging. Although it has been shown that the lateral size of CsPbBr₃ is tunable up to a few micrometers by varying the ratio of short-chain (octanoic acid and octylamine) to long-chain ligands (OLA and OA), the exact mechanism is still unclear and has not been extended to perovskite NPLs of other compositions. A thorough understanding of the anisotropic growth of perovskite NPLs is lacking in the literature. It is unclear how isotropic nucleation leads to anisotropic growth in the end. It has been shown that a reduction in the reaction temperature, an increase in the length of the ligands used in synthesis and an increase of the A-site to B-site cation ratio in the precursor solution generally favors NPL formation. For instance, Manna et al. proposed that the increase of concentration of the alkylammonium cation under acidic conditions or decrease of Cs⁺ concentration in the reaction medium leads to the formation of NPLs. However, it is rather unclear how the ammonium cations favor the growth of some facets over others. It could be most likely related to the differences in the energy of the facets and this the ligands bind strongly to certain facets while the other facets grow freely, leading to anisotropic NPLs. In the case of CdSe NPLs, Riedinger et al. showed that the intrinsic instability in growth kinetics leads to highly anisotropic shapes, and this could also apply to perovskite NPLs. Recently, Burlakov et al. proposed that the ligands nucleate faster than the atoms in precursor molecules on relatively wide crystal facets, thus leading to NPL formation.^[322] However, we strongly believe that more in-depth theoretical and experimental studies are required to understand the growth mechanisms of perovskite NPLs. Another important

challenge in perovskite NPL synthesis is to obtain colloidal solutions with long-term stability. The thin NPLs often tend to transform into thick plates or degrade into non-fluorescent phases over time. In addition, they are very sensitive to external stress factors, such as light and heat, and often transform into larger nanosheets or bulk perovskites.^[115,280] The stability of NPLs can be improved by proper ligand choice (such as (3-aminopropyl)trimethoxysilan and bulky ligands) or through the surface coatings (such as SiO₂ and polymers).^[84,122] For example, Shamsi et al. demonstrated the synthesis of CsPbBr₃ NPLs with improved stability using hexylphosphonate ligands. We believe that the surface coating strategies such as SiO₂ coating, polymer or MOF encapsulation applied to nanocubes could also be extended to NPLs to improve their colloidal stability. However, the surface coatings can be detrimental for charge carrier transport between NPLs and thus effects the performance of the corresponding devices. An approach to overcome this problem is through surface functionalization of NPLs with conjugated organic chromophores.^[244]

5.2. Optical Properties and Carrier Dynamics

Research into perovskite NPLs is still at an early stage, and their linear/nonlinear optoelectronic properties have not yet been fully explored. From the fundamental point of view, perovskite NPLs provide a unique and ideal platform for testing their optoelectronic properties, since both confined and unconfined dimensions coexist. Therefore, despite recent interesting studies on perovskite NPLs, more rigorous and systematic studies on the role of dimensionality (thickness and lateral size) on the electronic properties of perovskite NPLs are still required. For instance, the study on anisotropic exciton or charge diffusion dynamics in perovskite NPLs with different lateral aspect ratios has not been carried out, although this study can provide a way to improve light outcoupling and boost efficiencies, as compared to the isotropic device (e.g., based on perovskite nanocubes). Furthermore, investigations into the relative ratio of excitons versus charge generation in thickness-controlled perovskite NPLs will tell us what the optimal thicknesses are for LED or photovoltaic applications since the radiative recombination of excitons usually occurs in competition to nonradiative processes (i.e., exciton dissociation and subsequent charge diffusion). Beyond the study on individual perovskite NPLs, the investigation on the assembled perovskite NPLs (e.g., the studies into the mechanism for the spontaneous self-assembly of perovskite NPLs into cuboid crystals, and concomitant changes in the electronic properties) can open a new avenue of utilizing perovskite NPLs in advanced lighting and display applications.^[323]

5.3. Colloidal Perovskite Nanoplatelet LEDs

Despite the early successful development of NPL PeLEDs through effective surface passivation methods, there is still much room for improving their EQEs to over 20%, which has been achieved with perovskite nanocrystals and quasi-2D films. With perovskite NPLs, it is still difficult to achieve ligand

exchange postsynthesis, and further efforts in this area are needed because this will allow carrier injection and balance to be more effectively tuned, and decouple the liable ligands needed for synthesis (OAm and OA ligands) with those for devices (short-chain ligands with higher conductivity). Alternatively, forming NPLs with core-shell structures to passivate surface defects while allowing facile charge injection has been considered for nanocrystals, but not yet for nanoplatelets. Appropriate ligand engineering could also lead to improved control over the thickness of the emissive layer, which is currently difficult to achieve. Optical simulations are also needed to determine the optimal thickness of the NPLs layer to maximize outcoupling. Concomitantly, further development is needed for the hole and electron injection layers, particularly to achieve improved alignment with the deep VBM of NPLs. Whilst early works have reported methods for controlling the orientation of NPL made from II to VI semiconductors, full control of the alignment of TDMs in perovskites has not yet been achieved. More studies are needed to fully understand how TDMs are oriented in perovskite NPLs and their effects on polarized emission and outcoupling efficiency in a planar device structure.

The operational stability of perovskite NPLs in LEDs is another key factor that needs to be improved for these devices to be considered for commercialization. Although perovskite NPLs have advantages over mixed halide perovskite emitters for achieving stable electroluminescence spectra, they still suffer from severe efficiency roll-off due to Auger recombination and exciton-exciton annihilation. How these high-order nonradiative recombination pathways can be suppressed in NPL LEDs would be a future challenge to further improve device performance.

Overall, perovskite NPLs offer a rich area of research, with many new opportunities both at the fundamental level (e.g., to understand the role of different levels of confinement across different dimensions) and at the applications level (e.g., achieving spectrally stable PeLEDs). While there are many promising and interesting recent investigations into this class of semiconductors, it is evident that our understanding of these materials is at an early stage, and there are many challenges that need to be overcome before the practical benefits of perovskite NPLs could be realized. We hope the discussions made in this Review could stimulate and shape future work into this area.

Acknowledgements

C.O.-M., J.Y., and J.S. contributed equally to the work. L.P. acknowledges the support from the Spanish Ministerio de Ciencia e Innovación through Ramón y Cajal grant (RYC2018-026103-I) and the Spanish State Research Agency (Grant No. PID2020-117371RA-I00), the grant from the Xunta de Galicia (ED431F2021/05). Funding from Xunta de Galicia/FEDER (grant GRC ED431C2020/09) is gratefully acknowledged. R.L.Z.H. acknowledges support from the Royal Academy of Engineering under the Research Fellowships scheme (no.: RF\201718\1701). J.S. acknowledges support from the DGIST Start-up Fund Program of the Ministry of Science and ICT (2021070009). The authors acknowledge the Universidade de Vigo/CISUG for open access funding.

Note: In the originally published review, Figure 5A was incorrectly cited in Section 2.2, paragraph beginning "Although the synthesis and optical properties of MAPbX₃ perovskite NPLs..." That citation was corrected to Figure 6a on March 10, 2022, after initial publication online.

Conflict of Interest

The authors declare no conflict of interest.

Keywords

2D perovskites, light-emitting devices, perovskite nanocrystals, perovskite nanoplatelets, perovskite nanosheets, quantum confinement

Received: September 7, 2021

Revised: November 9, 2021

Published online: January 28, 2022

- [1] Y. Chen, Y. Sun, J. Peng, J. Tang, K. Zheng, Z. Liang, *Adv. Mater.* **2018**, *30*, 1703487.
- [2] C. Huo, B. Cai, Z. Yuan, B. Ma, H. Zeng, *Small Methods* **2017**, *1*, 1600018.
- [3] M. Nasilowski, B. Mahler, E. Lhuillier, S. Ithurria, B. Dubertret, *Chem. Rev.* **2016**, *116*, 10934.
- [4] J. S. Son, J. H. Yu, S. G. Kwon, J. Lee, J. Joo, T. Hyeon, *Adv. Mater.* **2011**, *23*, 3214.
- [5] E. Lhuillier, S. Pedetti, S. Ithurria, B. Nadal, H. Heuclin, B. Dubertret, *Acc. Chem. Res.* **2015**, *48*, 22.
- [6] C. Tan, X. Cao, X.-J. Wu, Q. He, J. Yang, X. Zhang, J. Chen, W. Zhao, S. Han, G.-H. Nam, M. Sindoro, H. Zhang, *Chem. Rev.* **2017**, *117*, 6225.
- [7] S. Ithurria, M. D. Tessier, B. Mahler, R. P. S. M. Lobo, B. Dubertret, A. L. Efros, *Nat. Mater.* **2011**, *10*, 936.
- [8] Z. Chen, B. Nadal, B. Mahler, H. Aubin, B. Dubertret, *Adv. Funct. Mater.* **2014**, *24*, 295.
- [9] M. C. Weidman, A. J. Goodman, W. A. Tisdale, *Chem. Mater.* **2017**, *29*, 5019.
- [10] J. Zhang, Y. Sun, S. Ye, J. Song, J. Qu, *Chem. Mater.* **2020**, *32*, 9490.
- [11] J. Yu, R. Chen, *InfoMat* **2020**, *2*, 905.
- [12] A. Sharma, M. Sharma, K. Gungor, M. Olutas, D. Dede, H. V. Demir, *Adv. Opt. Mater.* **2019**, *7*, 1900831.
- [13] C. Bouet, M. D. Tessier, S. Ithurria, B. Mahler, B. Nadal, B. Dubertret, *Chem. Mater.* **2013**, *25*, 1262.
- [14] A. Dey, J. Ye, A. De, E. Debroye, S. K. Ha, E. Bladt, A. S. Kshirsagar, Z. Wang, J. Yin, Y. Wang, L. N. Quan, F. Yan, M. Gao, X. Li, J. Shamsi, T. Debnath, M. Cao, M. A. Scheel, S. Kumar, J. A. Steele, M. Gerhard, L. Chouhan, K. Xu, X.-g. Wu, Y. Li, Y. Zhang, A. Dutta, C. Han, I. Vincon, A. L. Rogach, et al., *ACS Nano* **2021**, *15*, 10775.
- [15] J. Ye, M. M. Byrnavand, C. O. Martínez, R. L. Z. Hoye, M. Saliba, L. Polavarapu, *Angew. Chem., Int. Ed.* **2021**, *60*, 21636.
- [16] L. Protesescu, S. Yakunin, M. I. Bodnarchuk, F. Krieg, R. Caputo, C. H. Hendon, R. X. Yang, A. Walsh, M. V. Kovalenko, *Nano Lett.* **2015**, *15*, 3692.
- [17] X. Li, Y. Wu, S. Zhang, B. Cai, Y. Gu, J. Song, H. Zeng, *Adv. Funct. Mater.* **2016**, *26*, 2435.
- [18] J. Shamsi, A. S. Urban, M. Imran, L. De Trizio, L. Manna, *Chem. Rev.* **2019**, *119*, 3296.
- [19] M. V. Kovalenko, L. Protesescu, M. I. Bodnarchuk, *Science* **2017**, *358*, 745.
- [20] A. Swarnkar, A. R. Marshall, E. M. Sanehira, B. D. Chernomordik, D. T. Moore, J. A. Christians, T. Chakrabarti, J. M. Luther, *Science* **2016**, *354*, 92.
- [21] S. Ghimire, C. Klinke, *Nanoscale* **2021**, *13*, 12394.
- [22] L. C. Schmidt, A. Pertegás, S. González-Carrero, O. Malinkiewicz, S. Agouram, G. Mínguez Espallargas, H. J. Bolink, R. E. Galian, J. Pérez-Prieto, *J. Am. Chem. Soc.* **2014**, *136*, 850.

- [23] J. Song, J. Li, X. Li, L. Xu, Y. Dong, H. Zeng, *Adv. Mater.* **2015**, *27*, 7162.
- [24] K. Hills-Kimball, H. Yang, T. Cai, J. Wang, O. Chen, *Adv. Sci.* **2021**, *8*, 2100214.
- [25] M. C. Weidman, M. Seitz, S. D. Stranks, W. A. Tisdale, *ACS Nano* **2016**, *10*, 7830.
- [26] Y. Tong, E. Bladt, M. F. Aygüler, A. Manzi, K. Z. Milowska, V. A. Hintermayr, P. Docampo, S. Bals, A. S. Urban, L. Polavarapu, J. Feldmann, *Angew. Chem., Int. Ed.* **2016**, *55*, 13887.
- [27] J. Ramade, L. M. Andriambariarijaona, V. Steinmetz, N. Goubet, L. Legrand, T. Barisien, F. Bernardot, C. Testelin, E. Lhuillier, A. Bramati, M. Chamarro, *Nanoscale* **2018**, *10*, 6393.
- [28] J. A. Sichert, Y. Tong, N. Mutz, M. Vollmer, S. Fischer, K. Z. Milowska, R. García Cortadella, B. Nickel, C. Cardenas-Daw, J. K. Stolarczyk, A. S. Urban, J. Feldmann, *Nano Lett.* **2015**, *15*, 6521.
- [29] B. J. Bohn, Y. Tong, M. Gramlich, M. L. Lai, M. Döblinger, K. Wang, R. L. Z. Hoyer, P. Müller-Buschbaum, S. D. Stranks, A. S. Urban, L. Polavarapu, J. Feldmann, *Nano Lett.* **2018**, *18*, 5231.
- [30] Q. A. Akkerman, S. G. Motti, A. R. Srimath Kandada, E. Mosconi, V. D'Innocenzo, G. Bertoni, S. Marras, B. A. Kamino, L. Miranda, F. De Angelis, A. Petrozza, M. Prato, L. Manna, *J. Am. Chem. Soc.* **2016**, *138*, 1010.
- [31] Y. Bekenstein, B. A. Koscher, S. W. Eaton, P. Yang, A. P. Alivisatos, *J. Am. Chem. Soc.* **2015**, *137*, 16008.
- [32] Y. Tong, F. Ehrat, W. Vanderlinden, C. Cardenas-Daw, J. K. Stolarczyk, L. Polavarapu, A. S. Urban, *ACS Nano* **2016**, *10*, 10936.
- [33] G. Almeida, L. Goldoni, Q. Akkerman, Z. Dang, A. H. Khan, S. Marras, I. Moreels, L. Manna, *ACS Nano* **2018**, *12*, 1704.
- [34] Y. He, L. Matei, H. J. Jung, K. M. McCall, M. Chen, C. C. Stoumpos, Z. Liu, J. A. Peters, D. Y. Chung, B. W. Wessels, M. R. Wasielewski, V. P. Dravid, A. Burger, M. G. Kanatzidis, *Nat. Commun.* **2018**, *9*, 1609.
- [35] J. Peng, C. Q. Xia, Y. Xu, R. Li, L. Cui, J. K. Clegg, L. M. Herz, M. B. Johnston, Q. Lin, *Nat. Commun.* **2021**, *12*, 1531.
- [36] M. I. Saidaminov, M. A. Haque, J. Almutlaq, S. Sarmah, X.-H. Miao, R. Begum, A. A. Zhumekenov, I. Dursun, N. Cho, B. Murali, O. F. Mohammed, T. Wu, O. M. Bakr, *Adv. Opt. Mater.* **2017**, *5*, 1600704.
- [37] S. G. Motti, F. Krieg, A. J. Ramadan, J. B. Patel, H. J. Snaith, M. V. Kovalenko, M. B. Johnston, L. M. Herz, *Adv. Funct. Mater.* **2020**, *30*, 1909904.
- [38] Z. Hu, Z. Liu, Y. Bian, D. Liu, X. Tang, W. Hu, Z. Zang, M. Zhou, L. Sun, J. Tang, Y. Li, J. Du, Y. Leng, *Adv. Opt. Mater.* **2017**, *5*, 1700419.
- [39] S. K. Ha, W. A. Tisdale, *J. Visualized Exp.* **2019**, *152*, e60114.
- [40] S. Bhaumik, S. A. Veldhuis, Y. F. Ng, M. Li, S. K. Muduli, T. C. Sum, B. Damodaran, S. Mhaisalkar, N. Mathews, *Chem. Commun.* **2016**, *52*, 7118.
- [41] Q. Wang, X.-D. Liu, Y.-H. Qiu, K. Chen, L. Zhou, Q.-Q. Wang, *AIP Adv.* **2018**, *8*, 025108.
- [42] X. Wu, M. T. Trinh, D. Niesner, H. Zhu, Z. Norman, J. S. Owen, O. Yaffe, B. J. Kudisch, X. Y. Zhu, *J. Am. Chem. Soc.* **2015**, *137*, 2089.
- [43] C. C. Stoumpos, D. H. Cao, D. J. Clark, J. Young, J. M. Rondinelli, J. I. Jang, J. T. Hupp, M. G. Kanatzidis, *Chem. Mater.* **2016**, *28*, 2852.
- [44] C. J. Dahlan, N. R. Venkatesan, P. T. Corona, R. M. Kennard, L. Mao, N. C. Smith, J. Zhang, R. Seshadri, M. E. Helgeson, M. L. Chabinyc, *ACS Nano* **2020**, *14*, 11294.
- [45] J.-C. Blancon, H. Tsai, W. Nie, C. C. Stoumpos, L. Pedesseau, C. Katan, M. Kepenekian, C. M. M. Soe, K. Appavoo, M. Y. Sfeir, S. Tretiak, P. M. Ajayan, M. G. Kanatzidis, J. Even, J. J. Crochet, A. D. Mohite, *Science* **2017**, *355*, 1288.
- [46] K. Marjit, G. Ghosh, S. Ghosh, S. Sain, A. Ghosh, A. Patra, *J. Phys. Chem. C* **2021**, *125*, 12214.
- [47] L. G. Bonato, R. F. Moral, G. Nagamine, A. Alo, J. C. Germino, D. S. da Silva, D. B. Almeida, L. F. Zagonel, F. Galembeck, L. A. Padilha, A. F. Nogueira, *Angew. Chem., Int. Ed.* **2020**, *59*, 11501.
- [48] G. H. Ahmed, J. Yin, R. Bose, L. Sinatra, E. Alarousu, E. Yengel, N. M. AlYami, M. I. Saidaminov, Y. Zhang, M. N. Hedhili, O. M. Bakr, J.-L. Brédas, O. F. Mohammed, *Chem. Mater.* **2017**, *29*, 4393.
- [49] S. Kumar, J. Jagielski, S. Yakunin, P. Rice, Y. C. Chiu, M. C. Wang, G. Nedelcu, Y. Kim, S. C. Lin, E. J. G. Santos, M. V. Kovalenko, C. J. Shih, *ACS Nano* **2016**, *10*, 9720.
- [50] M. P. Hautzinger, D. Pan, A. K. Pigg, Y. Fu, D. J. Morrow, M. Leng, M.-Y. Kuo, N. Spitha, D. P. Lafayette, D. D. Kohler, J. C. Wright, S. Jin, *ACS Energy Lett.* **2020**, *5*, 1430.
- [51] R. M. Maceiczky, K. Dümbgen, I. Lignos, L. Protesescu, M. V. Kovalenko, A. J. deMello, *Chem. Mater.* **2017**, *29*, 8433.
- [52] L. Protesescu, S. Yakunin, S. Kumar, J. Bär, F. Bertolotti, N. Masciocchi, A. Guagliardi, M. Grotevent, I. Shorubalko, M. I. Bodnarchuk, C.-J. Shih, M. V. Kovalenko, *ACS Nano* **2017**, *11*, 3119.
- [53] Y. Wu, C. Wei, X. Li, Y. Li, S. Qiu, W. Shen, B. Cai, Z. Sun, D. Yang, Z. Deng, H. Zeng, *ACS Energy Lett.* **2018**, *3*, 2030.
- [54] O. Vyborny, S. Yakunin, M. V. Kovalenko, *Nanoscale* **2016**, *8*, 6278.
- [55] D. Yu, F. Cao, Y. Gao, Y. Xiong, H. Zeng, *Adv. Funct. Mater.* **2018**, *28*, 1800248.
- [56] H. Huang, Y. Li, Y. Tong, E.-P. Yao, M. W. Feil, A. F. Richter, M. Döblinger, A. L. Rogach, J. Feldmann, L. Polavarapu, *Angew. Chem., Int. Ed.* **2019**, *58*, 16558.
- [57] J. Zhao, S. Cao, Z. Li, N. Ma, *Chem. Mater.* **2018**, *30*, 6737.
- [58] W. Paritmongkol, N. S. Dahod, A. Stollmann, N. N. Mao, C. Setzens, S. L. Zheng, W. A. Tisdale, *Chem. Mater.* **2019**, *31*, 5592.
- [59] F. Bertolotti, G. Nedelcu, A. Vivani, A. Cervellino, N. Masciocchi, A. Guagliardi, M. V. Kovalenko, *ACS Nano* **2019**, *13*, 14294.
- [60] M. A. Uddin, J. D. Glover, S. M. Park, J. T. Pham, K. R. Graham, *Chem. Mater.* **2020**, *32*, 5217.
- [61] L. Protesescu, S. Yakunin, M. I. Bodnarchuk, F. Bertolotti, N. Masciocchi, A. Guagliardi, M. V. Kovalenko, *J. Am. Chem. Soc.* **2016**, *138*, 14202.
- [62] Y. N. Zhang, C. J. Thomas, A. Guillaussier, D. M. Smilgies, B. A. Korgel, *J. Phys. Chem. C* **2019**, *123*, 17555.
- [63] I. Levchuk, A. Osvet, X. Tang, M. Brandl, J. D. Perea, F. Hoegl, G. J. Matt, R. Hock, M. Batentschuk, C. J. Brabec, *Nano Lett.* **2017**, *17*, 2765.
- [64] R. B. Cevallos-Toledo, I. Rosa-Pardo, R. Arenal, V. Oestreicher, M. Fickert, G. Abellán, R. E. Galian, J. Pérez-Prieto, *Angew. Chem., Int. Ed.*, <https://doi.org/10.1002/anie.202113451>.
- [65] T. Ishihara, J. Takahashi, T. Goto, *Solid State Commun.* **1989**, *69*, 933.
- [66] D. B. Mitzi, C. A. Feild, W. T. A. Harrison, A. M. Guloy, *Nature* **1994**, *369*, 467.
- [67] X. Li, J. M. Hoffman, M. G. Kanatzidis, *Chem. Rev.* **2021**, *121*, 2230.
- [68] L. Dou, A. B. Wong, Y. Yu, M. Lai, N. Kornienko, S. W. Eaton, A. Fu, C. G. Bischak, J. Ma, T. Ding, N. S. Ginsberg, L.-W. Wang, A. P. Alivisatos, P. Yang, *Science* **2015**, *349*, 1518.
- [69] P. Tyagi, S. M. Arveson, W. A. Tisdale, *J. Phys. Chem. Lett.* **2015**, *6*, 1911.
- [70] V. A. Hintermayr, L. Polavarapu, A. S. Urban, J. Feldmann, *ACS Nano* **2018**, *12*, 10151.
- [71] V. A. Hintermayr, A. F. Richter, F. Ehrat, M. Döblinger, W. Vanderlinden, J. A. Sichert, Y. Tong, L. Polavarapu, J. Feldmann, A. S. Urban, *Adv. Mater.* **2016**, *28*, 9478.
- [72] L. Polavarapu, B. Nickel, J. Feldmann, A. S. Urban, *Adv. Energy Mater.* **2017**, *7*, 1700267.
- [73] C. Otero-Martínez, D. García-Lojo, I. Pastoriza-Santos, J. Pérez-Juste, L. Polavarapu, *Angew. Chem., Int. Ed.*, <https://doi.org/10.1002/anie.202109308>.
- [74] Z. Liang, S. Zhao, Z. Xu, B. Qiao, P. Song, D. Gao, X. Xu, *ACS Appl. Mater. Interfaces* **2016**, *8*, 28824.
- [75] A. Pan, B. He, X. Fan, Z. Liu, J. J. Urban, A. P. Alivisatos, L. He, Y. Liu, *ACS Nano* **2016**, *10*, 7943.
- [76] F. Zhang, H. Zhong, C. Chen, X.-g. Wu, X. Hu, H. Huang, J. Han, B. Zou, Y. Dong, *ACS Nano* **2015**, *9*, 4533.

- [77] L. Liu, S. Huang, L. Pan, L.-J. Shi, B. Zou, L. Deng, H. Zhong, *Angew. Chem., Int. Ed.* **2017**, *56*, 1780.
- [78] D. Chen, X. Chen, J. Li, X. Li, J. Zhong, *Dalton Trans.* **2018**, *47*, 9845.
- [79] W. Zhai, J. Lin, Q. Li, K. Zheng, Y. Huang, Y. Yao, X. He, L. Li, C. Yu, C. Liu, Y. Fang, Z. Liu, C. Tang, *Chem. Mater.* **2018**, *30*, 3714.
- [80] Q. Pan, H. Hu, Y. Zou, M. Chen, L. Wu, D. Yang, X. Yuan, J. Fan, B. Sun, Q. Zhang, *J. Mater. Chem. C* **2017**, *5*, 10947.
- [81] J. Shamsi, Z. Dang, P. Bianchini, C. Canale, F. Di Stasio, R. Brescia, M. Prato, L. Manna, *J. Am. Chem. Soc.* **2016**, *138*, 7240.
- [82] V. K. Ravi, A. Swarnkar, R. Chakraborty, A. Nag, *Nanotechnology* **2016**, *27*, 325708.
- [83] X. Zhang, X. Bai, H. Wu, X. Zhang, C. Sun, Y. Zhang, W. Zhang, W. Zheng, W. W. Yu, A. L. Rogach, *Angew. Chem., Int. Ed.* **2018**, *57*, 3337.
- [84] J. Shamsi, D. Kubicki, M. Anaya, Y. Liu, K. Ji, K. Frohna, C. P. Grey, R. H. Friend, S. D. Stranks, *ACS Energy Lett.* **2020**, *5*, 1900.
- [85] A. Chakraborty, S. Satija, U. Gangwar, S. Sapra, *Chem. Mater.* **2020**, *32*, 721.
- [86] A. Liu, C. Bi, X. Qu, J. Tian, *J. Phys. Chem. C* **2021**, *125*, 14204.
- [87] E. Socie, B. R. C. Vale, A. T. Terpstra, M. A. Schiavon, J.-E. Moser, *J. Phys. Chem. C* **2021**, *125*, 14317.
- [88] Q. Zeng, Y. Du, J. Jiang, Q. Yu, Y. Li, *J. Phys. Chem. Lett.* **2021**, *12*, 2668.
- [89] Z. Yuan, Y. Shu, Y. Xin, B. Ma, *Chem. Commun.* **2016**, *52*, 3887.
- [90] J. Cho, Y.-H. Choi, T. E. O'Loughlin, L. De Jesus, S. Banerjee, *Chem. Mater.* **2016**, *28*, 6909.
- [91] I. Levchuk, P. Herre, M. Brandl, A. Osvet, R. Hock, W. Peukert, P. Schweizer, E. Spiecker, M. Batentschuk, C. J. Brabec, *Chem. Commun.* **2017**, *53*, 244.
- [92] H. Zheng, W. Pan, W. Shen, *Nanotechnology* **2018**, *29*, 455601.
- [93] D. N. Minh, J. Kim, J. Hyon, J. H. Sim, H. H. Sowlih, C. Seo, J. Nam, S. Eom, S. Suk, S. Lee, E. Kim, Y. Kang, *Chem. Mater.* **2017**, *29*, 5713.
- [94] I. Lignos, L. Protesescu, D. B. Emiroglu, R. Maceiczky, S. Schneider, M. V. Kovalenko, A. J. deMello, *Nano Lett.* **2018**, *18*, 1246.
- [95] H. Fang, W. Deng, X. Zhang, X. Xu, M. Zhang, J. Jie, X. Zhang, *Nano Res.* **2019**, *12*, 171.
- [96] S. Peng, Z. Wen, T. Ye, X. Xiao, K. Wang, J. Xia, J. Sun, T. Zhang, G. Mei, H. Liu, B. Xu, X. Li, R. Chen, G. Xing, K. Wang, Z. Tang, *ACS Appl. Mater. Interfaces* **2020**, *12*, 31863.
- [97] A. Patra, S. Bera, D. Nasipuri, S. K. Dutta, N. Pradhan, *ACS Energy Lett.* **2021**, *6*, 2682.
- [98] L. Lian, G. Zhai, F. Cheng, Y. Xia, M. Zheng, J. Ke, M. Gao, H. Liu, D. Zhang, L. Li, J. Gao, J. Tang, J. Zhang, *CrystEngComm* **2018**, *20*, 7473.
- [99] J. Huang, S. Zou, J. Lin, Z. Liu, M. Qi, *Nano Res.* **2021**, *14*, 4079.
- [100] Z. Liu, H. Yang, J. Wang, Y. Yuan, K. Hills-Kimball, T. Cai, P. Wang, A. Tang, O. Chen, *Nano Lett.* **2021**, *21*, 1620.
- [101] A. B. Wong, Y. Bekenstein, J. Kang, C. S. Kley, D. Kim, N. A. Gibson, D. Zhang, Y. Yu, S. R. Leone, L.-W. Wang, A. P. Alivisatos, P. Yang, *Nano Lett.* **2018**, *18*, 2060.
- [102] J. Pal, S. Manna, A. Mondal, S. Das, K. V. Adarsh, A. Nag, *Angew. Chem., Int. Ed.* **2017**, *56*, 14187.
- [103] S. Gonzalez-Carrero, R. E. Galian, J. Pérez-Prieto, *J. Mater. Chem. A* **2015**, *3*, 9187.
- [104] B. D. Toso, S. C. Giannini, L. Manna, *ACS Nano*, <https://doi.org/10.1021/acsnano.1c08636>.
- [105] S. K. Ha, C. M. Mauck, W. A. Tisdale, *Chem. Mater.* **2019**, *31*, 2486.
- [106] G. M. Biesold, S. Liang, B. K. Wagner, Z. Kang, Z. Lin, *Nanoscale* **2021**, *13*, 13108.
- [107] Z. N. Georgieva, B. P. Bloom, S. Ghosh, D. H. Waldeck, *Adv. Mater.* **2018**, *30*, 1800097.
- [108] Y. Zhang, C. Wang, Z. Deng, *Chem. Commun.* **2018**, *54*, 4021.
- [109] H. Gao, W. Feng, H. Liu, S. Liu, Z. Wang, D. Yao, Y. Liu, D.-K. Teng, B. Yang, H. Zhang, *ACS Appl. Nano Mater.* **2020**, *3*, 4826.
- [110] W. J. Mir, M. Jagadeeswararao, S. Das, A. Nag, *ACS Energy Lett.* **2017**, *2*, 537.
- [111] A. Singldinger, M. Gramlich, C. Gruber, C. Lampe, A. S. Urban, *ACS Energy Lett.* **2020**, *5*, 1380.
- [112] Y. Wang, X. Li, S. Sreejith, F. Cao, Z. Wang, M. C. Stuparu, H. Zeng, H. Sun, *Adv. Mater.* **2016**, *28*, 10637.
- [113] M. Imran, P. Ijaz, D. Baranov, L. Goldoni, U. Petralanda, Q. Akkerman, A. L. Abdelhady, M. Prato, P. Bianchini, I. Infante, L. Manna, *Nano Lett.* **2018**, *18*, 7822.
- [114] Z.-J. Li, E. Hofman, A. H. Davis, M. M. Maye, W. Zheng, *Chem. Mater.* **2018**, *30*, 3854.
- [115] J. Shamsi, P. Rastogi, V. Caligiuri, A. L. Abdelhady, D. Spirito, L. Manna, R. Krahne, *ACS Nano* **2017**, *11*, 10206.
- [116] C. Huo, C. F. Fong, M.-R. Amara, Y. Huang, B. Chen, H. Zhang, L. Guo, H. Li, W. Huang, C. Diederichs, Q. Xiong, *Nano Lett.* **2020**, *20*, 3673.
- [117] H. Lin, Q. Wei, K. W. Ng, J.-Y. Dong, J.-L. Li, W.-W. Liu, S.-S. Yan, S. Chen, G.-C. Xing, X.-S. Tang, Z.-K. Tang, S.-P. Wang, *Small* **2021**, *17*, 2101359.
- [118] A. Dutta, R. K. Behera, P. Pal, S. Baitalik, N. Pradhan, *Angew. Chem., Int. Ed.* **2019**, *58*, 5552.
- [119] F. Di Stasio, S. Christodoulou, N. Huo, G. Konstantatos, *Chem. Mater.* **2017**, *29*, 7663.
- [120] R. Grisorio, D. Conelli, E. Fanizza, M. Striccoli, D. Altamura, C. Giannini, I. Allegretta, R. Terzano, M. Irimia-Vladu, N. Margiotta, G. P. Suranna, *Nanoscale Adv.* **2021**, *3*, 3918.
- [121] B. A. Koscher, J. K. Swabeck, N. D. Bronstein, A. P. Alivisatos, *J. Am. Chem. Soc.* **2017**, *139*, 6566.
- [122] H. Huang, W. Zhao, H. Yang, X. Zhang, J. Su, K. Hu, Z. Nie, Y. Li, J. Zhong, *J. Mater. Chem. C* **2021**, *9*, 5535.
- [123] R. L. Z. Hoye, M.-L. Lai, M. Anaya, Y. Tong, K. Gałkowski, T. Doherty, W. Li, T. N. Huq, S. Mackowski, L. Polavarapu, J. Feldmann, J. L. MacManus-Driscoll, R. H. Friend, A. S. Urban, S. D. Stranks, *ACS Energy Lett.* **2019**, *4*, 1181.
- [124] Y. Zhou, J. Chen, O. M. Bakr, H.-T. Sun, *Chem. Mater.* **2018**, *30*, 6589.
- [125] X. Zhang, L. Li, Z. Sun, J. Luo, *Chem. Soc. Rev.* **2019**, *48*, 517.
- [126] Q. Cao, A. Ilyas, S. Zhang, Z. Ju, F. Sun, T. Liu, Y. Yang, Y. Lu, X. Liu, R. Deng, *Nanoscale* **2021**, *13*, 11552.
- [127] S. Das Adhikari, S. K. Dutta, A. Dutta, A. K. Guria, N. Pradhan, *Angew. Chem., Int. Ed.* **2017**, *56*, 8746.
- [128] S. Paul, E. Bladt, A. F. Richter, M. Döblinger, Y. Tong, H. Huang, A. Dey, S. Bals, T. Debnath, L. Polavarapu, J. Feldmann, *Angew. Chem., Int. Ed.* **2020**, *59*, 6794.
- [129] N. Pradhan, S. Das Adhikari, A. Nag, D. D. Sarma, *Angew. Chem., Int. Ed.* **2017**, *56*, 7038.
- [130] W. Liu, Q. Lin, H. Li, K. Wu, I. Robel, J. M. Pietryga, V. I. Klimov, *J. Am. Chem. Soc.* **2016**, *138*, 14954.
- [131] D. Parobek, B. J. Roman, Y. Dong, H. Jin, E. Lee, M. Sheldon, D. H. Son, *Nano Lett.* **2016**, *16*, 7376.
- [132] Y. Zhao, C. Xie, X. Zhang, K. Matras-Postolek, P. Yang, *ACS Appl. Nano Mater.* **2021**, *4*, 6223.
- [133] S. Das Adhikari, A. Dutta, S. K. Dutta, N. Pradhan, *ACS Energy Lett.* **2018**, *3*, 1247.
- [134] Z. Chen, L. Dong, C. Zhou, B. Zhou, Z. Zheng, R. Chen, J. Zang, *CrystEngComm* **2021**, *23*, 793.
- [135] Z.-J. Li, E. Hofman, A. H. Davis, A. Khammang, J. T. Wright, B. Dzikowski, R. W. Meulenberg, W. Zheng, *Chem. Mater.* **2018**, *30*, 6400.
- [136] K. Justice Babu, G. Kaur, A. Shukla, A. Kaur, T. Goswami, N. Ghorai, H. N. Ghosh, *J. Phys. Chem. Lett.* **2021**, *12*, 302.
- [137] D. Parobek, Y. Dong, T. Qiao, D. H. Son, *Chem. Mater.* **2018**, *30*, 2939.
- [138] J. H. Yu, X. Liu, K. E. Kweon, J. Joo, J. Park, K.-T. Ko, D. W. Lee, S. Shen, K. Tivakornsasithorn, J. S. Son, J.-H. Park, Y.-W. Kim,

- G. S. Hwang, M. Dobrowolska, J. K. Furdyna, T. Hyeon, *Nat. Mater.* **2010**, 9, 47.
- [139] Y. Liu, A. Nag, L. Manna, Z. Xia, *Angew. Chem., Int. Ed.* **2021**, 60, 11592.
- [140] Y. Liu, X. Rong, M. Li, M. S. Molokeev, J. Zhao, Z. Xia, *Angew. Chem., Int. Ed.* **2020**, 59, 11634.
- [141] F. Locardi, M. Samoli, A. Martinelli, O. Erdem, D. V. Magalhaes, S. Bals, Z. Hens, *ACS Nano* **2021**, 15, 17729.
- [142] T. Niu, Q. Xue, H.-L. Yip, *Nanophotonics* **2020**, 10, 2069.
- [143] S. Bhattacharya, G. K. Chandra, P. Predeep, *Front. Nanotechnol.* **2021**, 3, 657948.
- [144] J. Jagielski, S. Kumar, W.-Y. Yu, C.-J. Shih, *J. Mater. Chem. C* **2017**, 5, 5610.
- [145] J. Wang, J. Dong, F. Lu, C. Sun, Q. Zhang, N. Wang, *J. Mater. Chem. A* **2019**, 7, 23563.
- [146] A. Brumberg, S. M. Harvey, J. P. Philbin, B. T. Diroll, B. Lee, S. A. Crooker, M. R. Wasielewski, E. Rabani, R. D. Schaller, *ACS Nano* **2019**, 13, 8589.
- [147] L. Brus, *J. Phys. Chem.* **1986**, 90, 2555.
- [148] R. T. Collins, P. M. Fauchet, M. A. Tischler, *Phys. Today* **1997**, 50, 24.
- [149] K. K. Nanda, S. N. Sahu, *Adv. Mater.* **2001**, 13, 280.
- [150] E. O. Chukwuocha, M. C. Onyeaju, T. S. T. Harry, *World J. Condens. Matter Phys.* **2012**, 02, 96.
- [151] D. Saporì, M. Kepenekian, L. Pedesseau, C. Katan, J. Even, *Nanoscale* **2016**, 8, 6369.
- [152] J. C. Blancon, A. V. Stier, H. Tsai, W. Nie, C. C. Stoumpos, B. Traoré, L. Pedesseau, M. Kepenekian, F. Katsutani, G. T. Noe, J. Kono, S. Tretiak, S. A. Crooker, C. Katan, M. G. Kanatzidis, J. J. Crochet, J. Even, A. D. Mohite, *Nat. Commun.* **2018**, 9, 2254.
- [153] X.-F. He, *Phys. Rev. B* **1991**, 43, 2063.
- [154] I. B. Koutselas, L. Ducasse, G. C. Papavassiliou, *J. Phys.: Condens. Matter* **1996**, 8, 5953.
- [155] S. Elleuch, T. Dammak, Y. Abid, A. Mlayah, H. Boughzala, *J. Lumin.* **2010**, 130, 531.
- [156] B. Saporov, D. B. Mitzi, *Chem. Rev.* **2016**, 116, 4558.
- [157] A. J. Shin, A. A. Hossain, S. M. Tenney, X. Tan, L. A. Tan, J. J. Foley, T. L. Atallah, J. R. Caram, *J. Phys. Chem. Lett.* **2021**, 12, 4958.
- [158] L. M. Herz, *Annu. Rev. Phys. Chem.* **2016**, 67, 65.
- [159] B. J. Bohn, T. Simon, M. Gramlich, A. F. Richter, L. Polavarapu, A. S. Urban, J. Feldmann, *ACS Photonics* **2018**, 5, 648.
- [160] M. S. de Holanda, R. F. Moral, P. E. Marchezi, F. C. Marques, A. F. Nogueira, *EcoMat* **2021**, 3, e12124.
- [161] H. Mathieu, P. Lefebvre, P. Christol, *Phys. Rev. B* **1992**, 46, 4092.
- [162] S. Feldmann, M. K. Gangishetty, I. Bravić, T. Neumann, B. Peng, T. Winkler, R. H. Friend, B. Monserrat, D. N. Congreve, F. Deschler, *J. Am. Chem. Soc.* **2021**, 143, 8647.
- [163] R. E. Francke, J. A. C. Gallas, H. P. Grieneisen, J. Schifino, B. P. Chakraborty, *J. Chem. Phys.* **1980**, 72, 1476.
- [164] H. Huang, A. S. Susha, S. V. Kershaw, T. F. Hung, A. L. Rogach, *Adv. Sci.* **2015**, 2, 1500194.
- [165] S. J. W. Vonk, M. B. Fridriksson, S. O. M. Hinterding, M. J. J. Mangnus, T. P. van Swieten, F. C. Grozema, F. T. Rabouw, W. van der Stam, *J. Phys. Chem. C* **2020**, 124, 8047.
- [166] H. Utzat, W. Sun, A. E. K. Kaplan, F. Krieg, M. Ginterseder, B. Spokoyiny, N. D. Klein, K. E. Shulenberger, C. F. Perkinson, M. V. Kovalenko, M. G. Bawendi, *Science* **2019**, 363, 1068.
- [167] D. K. Sharma, S. Hirata, M. Vacha, *Nat. Commun.* **2019**, 10, 4499.
- [168] P. C. Sercel, J. L. Lyons, D. Wickramaratne, R. Vaxenburg, N. Bernstein, A. L. Efros, *Nano Lett.* **2019**, 19, 4068.
- [169] Z. C. R. Morandotti, *Nonlinear Photonics and Novel Optical Phenomena*, Springer, New York **2009**.
- [170] S. W. Eaton, M. Lai, N. A. Gibson, A. B. Wong, L. Dou, J. Ma, L.-W. Wang, S. R. Leone, P. Yang, *Proc. Natl. Acad. Sci. USA* **2016**, 113, 1993.
- [171] X. Han, Y. Zheng, S. Chai, S. Chen, J. Xu, *Nanophotonics* **2020**, 9, 1787.
- [172] A. Ferrando, J. P. Martínez Pastor, I. Suárez, *J. Phys. Chem. Lett.* **2018**, 9, 5612.
- [173] R. W. Boyd, in *Nonlinear Optics*, 2nd ed. (Ed: R. W. Boyd), Academic Press, San Diego, CA **2003**, p. 1.
- [174] L. Zhou, H. Fu, T. Lv, C. Wang, H. Gao, D. Li, L. Deng, W. Xiong, *Nanomaterials* **2020**, 10, 2263.
- [175] G. Vijaya Prakash, K. Pradeesh, R. Ratnani, K. Saraswat, M. E. Light, J. J. Baumberg, *J. Phys. D: Appl. Phys.* **2009**, 42, 185405.
- [176] Z.-Y. Zhang, H.-Y. Wang, Y.-X. Zhang, K.-J. Li, X.-P. Zhan, B.-R. Gao, Q.-D. Chen, H.-B. Sun, *Phys. Chem. Chem. Phys.* **2017**, 19, 2217.
- [177] W. Chen, S. Bhaumik, S. A. Veldhuis, G. Xing, Q. Xu, M. Grätzel, S. Mhaisalkar, N. Mathews, T. C. Sum, *Nat. Commun.* **2017**, 8, 15198.
- [178] Y. Yamada, T. Yamada, L. Q. Phuong, N. Maruyama, H. Nishimura, A. Wakamiya, Y. Murata, Y. Kanemitsu, *J. Am. Chem. Soc.* **2015**, 137, 10456.
- [179] F. Zhao, J. Li, X. Gao, X. Qiu, X. Lin, T. He, R. Chen, *J. Phys. Chem. C* **2019**, 123, 9538.
- [180] S. Roy, A. Mandal, A. Raj R, S. Bhattacharyya, B. Pal, *J. Phys. Chem. C* **2020**, 124, 15558.
- [181] V. Amendola, R. Pilot, M. Frasconi, O. M. Maragò, M. A. Iati, *J. Phys.: Condens. Matter* **2017**, 29, 203002.
- [182] N. Jiang, X. Zhuo, J. Wang, *Chem. Rev.* **2018**, 118, 3054.
- [183] W. L. Mochán, in *Encyclopedia of Condensed Matter Physics* (Eds: F. Bassani, G. L. Liedl, P. Wyder), Elsevier, Oxford **2005**, p. 310.
- [184] M. Litinskaya, in *Reference Module in Materials Science and Materials Engineering*, Elsevier, Amsterdam **2019**.
- [185] D. T. Ha, D. T. Thuy, V. T. Hoa, T. T. Van, N. A. Viet, *J. Phys.: Conf. Ser.* **2017**, 865, 012007.
- [186] D. N. Basov, A. Asenjo-Garcia, P. J. Schuck, X. Zhu, A. Rubio, *Nanophotonics* **2021**, 10, 549.
- [187] B. Deveaud, *Annu. Rev. Condens. Matter Phys.* **2015**, 6, 155.
- [188] R. Su, A. Fieramosca, Q. Zhang, H. S. Nguyen, E. Deleporte, Z. Chen, D. Sanvitto, T. C. H. Liew, Q. Xiong, *Nat. Mater.* **2021**, 20, 1315.
- [189] C. Ouyang, Y. Li, X. Fu, Z. Zeng, L. Huang, S. Liu, X. Wang, T. Gao, A. Pan, *Appl. Phys. Lett.* **2020**, 117, 221107.
- [190] R. Balili, V. Hartwell, D. Snoke, L. Pfeiffer, K. West, *Science* **2007**, 316, 1007.
- [191] J. Wang, R. Su, J. Xing, D. Bao, C. Diederichs, S. Liu, T. C. H. Liew, Z. Chen, Q. Xiong, *ACS Nano* **2018**, 12, 8382.
- [192] J. B. Khurgin, *Nanophotonics* **2019**, 8, 629.
- [193] J. Flick, N. Rivera, P. Narang, *Nanophotonics* **2018**, 7, 1479.
- [194] D. G. Lidzey, D. D. C. Bradley, A. Armitage, S. Walker, M. S. Skolnick, *Science* **2000**, 288, 1620.
- [195] P. Vasa, C. Lienau, *ACS Photonics* **2018**, 5, 2.
- [196] C. M. Guvenc, N. Polat, S. Balci, *J. Mater. Chem. C* **2020**, 8, 16520.
- [197] R. Su, C. Diederichs, J. Wang, T. C. H. Liew, J. Zhao, S. Liu, W. Xu, Z. Chen, Q. Xiong, *Nano Lett.* **2017**, 17, 3982.
- [198] J. M. Richter, F. Branchi, F. Valduga de Almeida Camargo, B. Zhao, R. H. Friend, G. Cerullo, F. Deschler, *Nat. Commun.* **2017**, 8, 376.
- [199] Y. Yang, D. P. Ostrowski, R. M. France, K. Zhu, J. van de Lagemaat, J. M. Luther, M. C. Beard, *Nat. Photonics* **2016**, 10, 53.
- [200] W. Graudszus, E. O. Göbel, *Physica B+C* **1983**, 117-118, 555.
- [201] T. Sohler, M. Calandra, F. Mauri, *Phys. Rev. B* **2016**, 94, 085415.
- [202] M. Baranowski, P. Plochocka, *Adv. Energy Mater.* **2020**, 10, 1903659.
- [203] Y. Li, X. Luo, Y. Liu, X. Lu, K. Wu, *ACS Energy Lett.* **2020**, 5, 1701.
- [204] V. I. Klimov, *J. Phys. Chem. B* **2000**, 104, 6112.
- [205] W. Tao, C. Zhang, Q. Zhou, Y. Zhao, H. Zhu, *Nat. Commun.* **2021**, 12, 1400.
- [206] C. Villamil Franco, B. Mahler, C. Cornaggia, T. Gustavsson, E. Cassette, *ACS Appl. Nano Mater.* **2021**, 4, 558.

- [207] J. Aneesh, A. Swarnkar, V. Kumar Ravi, R. Sharma, A. Nag, K. V. Adarsh, *J. Phys. Chem. C* **2017**, *121*, 4734.
- [208] A. Shukla, G. Kaur, K. J. Babu, N. Ghorai, T. Goswami, A. Kaur, H. N. Ghosh, *J. Phys. Chem. Lett.* **2020**, *11*, 6344.
- [209] Y. Zhai, S. Baniya, C. Zhang, J. Li, P. Haney, C.-X. Sheng, E. Ehrenfreund, Z. V. Vardeny, *Sci. Adv.* **2017**, *3*, e1700704.
- [210] B. Scharf, T. Frank, M. Gmitra, J. Fabian, I. Žutić, V. Perebeinos, *Phys. Rev. B* **2016**, *94*, 245434.
- [211] M. Combescot, R. Combescot, *Phys. Rev. B* **1989**, *40*, 3788.
- [212] B. R. C. Vale, E. Socie, A. Burgos-Caminal, J. Bettini, M. A. Schiavon, J.-E. Moser, *J. Phys. Chem. Lett.* **2020**, *11*, 387.
- [213] M. Gramlich, B. J. Bohn, Y. Tong, L. Polavarapu, J. Feldmann, A. S. Urban, *J. Phys. Chem. Lett.* **2020**, *11*, 5361.
- [214] G. Delpont, G. Chehade, F. Lédée, H. Diab, C. Milesi-Brault, G. Trippé-Allard, J. Even, J.-S. Lauret, E. Deleporte, D. Garrot, *J. Phys. Chem. Lett.* **2019**, *10*, 5153.
- [215] V. I. Klimov, A. A. Mikhailovsky, D. W. McBranch, C. A. Leatherdale, M. G. Bawendi, *Science* **2000**, *287*, 1011.
- [216] Y. Li, T. Ding, X. Luo, Z. Chen, X. Liu, X. Lu, K. Wu, *Nano Res.* **2019**, *12*, 619.
- [217] I. Robel, R. Gresback, U. Kortshagen, R. D. Schaller, V. I. Klimov, *Phys. Rev. Lett.* **2009**, *102*, 177404.
- [218] Q. Li, Y. Yang, W. Que, T. Lian, *Nano Lett.* **2019**, *19*, 5620.
- [219] H. Yeo, J. S. Lee, M. E. Khan, H. S. Kim, D. Y. Jeon, Y.-H. Kim, *J. Phys. Mater.* **2020**, *3*, 034012.
- [220] M. Elsässer, S. G. Hense, M. Wegener, *Appl. Phys. Lett.* **1997**, *70*, 853.
- [221] M. A. Green, A. Ho-Baillie, *ACS Energy Lett.* **2017**, *2*, 822.
- [222] Z. Xiao, Q. Dong, C. Bi, Y. Shao, Y. Yuan, J. Huang, *Adv. Mater.* **2014**, *26*, 6503.
- [223] Z.-K. Tan, R. S. Moghaddam, M. L. Lai, P. Docampo, R. Higler, F. Deschler, M. Price, A. Sadhanala, L. M. Pazos, D. Credgington, F. Hanusch, T. Bein, H. J. Snaith, R. H. Friend, *Nat. Nanotechnol.* **2014**, *9*, 687.
- [224] G. Xing, N. Mathews, S. Sun, S. S. Lim, Y. M. Lam, M. Grätzel, S. Mhaisalkar, T. C. Sum, *Science* **2013**, *342*, 344.
- [225] S. Deng, E. Shi, L. Yuan, L. Jin, L. Dou, L. Huang, *Nat. Commun.* **2020**, *11*, 664.
- [226] J. Sung, C. Schnedermann, L. Ni, A. Sadhanala, R. Y. S. Chen, C. Cho, L. Priest, J. M. Lim, H.-K. Kim, B. Monserrat, P. Kukura, A. Rao, *Nat. Phys.* **2020**, *16*, 171.
- [227] L. M. Herz, *ACS Energy Lett.* **2017**, *2*, 1539.
- [228] R. L. Milot, R. J. Sutton, G. E. Eperon, A. A. Haghighirad, J. M. Hardigree, L. Miranda, H. J. Snaith, M. B. Johnston, L. M. Herz, *Nano Lett.* **2016**, *16*, 7001.
- [229] X. Y. Zhu, V. Podzorov, *J. Phys. Chem. Lett.* **2015**, *6*, 4758.
- [230] X. Xiao, M. Wu, Z. Ni, S. Xu, S. Chen, J. Hu, P. N. Rudd, W. You, J. Huang, *Adv. Mater.* **2020**, *32*, 2004080.
- [231] M. Seitz, A. J. Magdaleno, N. Alcázar-Cano, M. Meléndez, T. J. Lubbers, S. W. Walraven, S. Pakdel, E. Prada, R. Delgado-Buscalioni, F. Prins, *Nat. Commun.* **2020**, *11*, 2035.
- [232] J. D. Ziegler, J. Zipfel, B. Meisinger, M. Menahem, X. Zhu, T. Taniguchi, K. Watanabe, O. Yaffe, D. A. Egger, A. Chernikov, *Nano Lett.* **2020**, *20*, 6674.
- [233] E. Penzo, A. Loiudice, E. S. Barnard, N. J. Borys, M. J. Jurow, M. Lorenzon, I. Rajzbaum, E. K. Wong, Y. Liu, A. M. Schwartzberg, S. Cabrini, S. Whitelam, R. Buonsanti, A. Weber-Bargioni, *ACS Nano* **2020**, *14*, 6999.
- [234] C. Zhao, W. Tian, Q. Sun, Z. Yin, J. Leng, S. Wang, J. Liu, K. Wu, S. Jin, *J. Am. Chem. Soc.* **2020**, *142*, 15091.
- [235] Y. L. Simon, M. Sze, K. K. Ng, in *Physics of Semiconductor Devices*, 4th ed., John Wiley and Sons, New York **2021**.
- [236] C. Zhao, W. Tian, J. Leng, Y. Zhao, S. Jin, *J. Phys. Chem. Lett.* **2019**, *10*, 3950.
- [237] E. Shi, S. Deng, B. Yuan, Y. Gao, Akriti, L. Yuan, C. S. Davis, D. Zemlyanov, Y. Yu, L. Huang, L. Dou, *ACS Nano* **2019**, *13*, 1635.
- [238] B. Traore, L. Pedesseau, L. Assam, X. Che, J.-C. Blancon, H. Tsai, W. Nie, C. C. Stoumpos, M. G. Kanatzidis, S. Tretiak, A. D. Mohite, J. Even, M. Kepenekian, C. Katan, *ACS Nano* **2018**, *12*, 3321.
- [239] Y. Zhang, M. Sun, N. Zhou, B. Huang, H. Zhou, *J. Phys. Chem. Lett.* **2020**, *11*, 7610.
- [240] X. Wu, M. T. Trinh, X. Y. Zhu, *J. Phys. Chem. C* **2015**, *119*, 14714.
- [241] A. Z. Chen, M. Shiu, J. H. Ma, M. R. Alpert, D. Zhang, B. J. Foley, D.-M. Smilgies, S.-H. Lee, J. J. Choi, *Nat. Commun.* **2018**, *9*, 1336.
- [242] W. A. Dunlap-Shohl, Y. Zhou, N. P. Padture, D. B. Mitzi, *Chem. Rev.* **2019**, *119*, 3193.
- [243] Q. Li, T. Lian, *J. Phys. Chem. Lett.* **2019**, *10*, 566.
- [244] M. C. Gélvez-Rueda, M. B. Fridriksson, R. K. Dubey, W. F. Jager, W. van der Stam, F. C. Grozema, *Nat. Commun.* **2020**, *11*, 1901.
- [245] Z. Yin, J. Leng, S. Wang, G. Liang, W. Tian, K. Wu, S. Jin, *J. Am. Chem. Soc.* **2021**, *143*, 4725.
- [246] C. Bao, J. Yang, S. Bai, W. Xu, Z. Yan, Q. Xu, J. Liu, W. Zhang, F. Gao, *Adv. Mater.* **2018**, *30*, 1803422.
- [247] X.-K. Liu, W. Xu, S. Bai, Y. Jin, J. Wang, R. H. Friend, F. Gao, *Nat. Mater.* **2021**, *20*, 10.
- [248] K. Zhang, N. Zhu, M. Zhang, L. Wang, J. Xing, *J. Mater. Chem. C* **2021**, *9*, 3795.
- [249] T. Chiba, Y. Hayashi, H. Ebe, K. Hoshi, J. Sato, S. Sato, Y.-J. Pu, S. Ohisa, J. Kido, *Nat. Photonics* **2018**, *12*, 681.
- [250] H. Wang, X. Gong, D. Zhao, Y.-B. Zhao, S. Wang, J. Zhang, L. Kong, B. Wei, R. Quintero-Bermudez, O. Voznyy, Y. Shang, Z. Ning, Y. Yan, E. H. Sargent, X. Yang, *Joule* **2020**, *4*, 1977.
- [251] X. Zhao, Z.-K. Tan, *Nat. Photonics* **2020**, *14*, 215.
- [252] G. Pacchioni, *Nat. Rev. Mater.* **2021**, *6*, 108.
- [253] P. Vashishtha, J. E. Halpert, *Chem. Mater.* **2017**, *29*, 5965.
- [254] G. Li, F. W. R. Rivarola, N. J. L. K. Davis, S. Bai, T. C. Jellicoe, F. de la Peña, S. Hou, C. Ducati, F. Gao, R. H. Friend, N. C. Greenham, Z.-K. Tan, *Adv. Mater.* **2016**, *28*, 3528.
- [255] N. K. Kumawat, A. Dey, A. Kumar, S. P. Gopinathan, K. L. Narasimhan, D. Kabra, *ACS Appl. Mater. Interfaces* **2015**, *7*, 13119.
- [256] M. Karlsson, Z. Yi, S. Reichert, X. Luo, W. Lin, Z. Zhang, C. Bao, R. Zhang, S. Bai, G. Zheng, P. Teng, L. Duan, Y. Lu, K. Zheng, T. Pullerits, C. Deibel, W. Xu, R. Friend, F. Gao, *Nat. Commun.* **2021**, *12*, 361.
- [257] F. Yuan, C. Ran, L. Zhang, H. Dong, B. Jiao, X. Hou, J. Li, Z. Wu, *ACS Energy Lett.* **2020**, *5*, 1062.
- [258] H. P. Kim, J. Kim, B. S. Kim, H.-M. Kim, J. Kim, A. R. b. M. Yusoff, J. Jang, M. K. Nazeeruddin, *Adv. Opt. Mater.* **2017**, *5*, 1600920.
- [259] H. Wang, X. Zhao, B. Zhang, Z. Xie, *J. Mater. Chem. C* **2019**, *7*, 5596.
- [260] B. Zhao, S. Bai, V. Kim, R. Lamboll, R. Shivanna, F. Auras, J. M. Richter, L. Yang, L. Dai, M. Alsari, X.-J. She, L. Liang, J. Zhang, S. Lilliu, P. Gao, H. J. Snaith, J. Wang, N. C. Greenham, R. H. Friend, D. Di, *Nat. Photonics* **2018**, *12*, 783.
- [261] Y. J. Yoon, Y. S. Shin, H. Jang, J. G. Son, J. W. Kim, C. B. Park, D. Yuk, J. Seo, G.-H. Kim, J. Y. Kim, *Nano Lett.* **2021**, *21*, 3473.
- [262] G. Li, in *Advanced Nanomaterials for Solar Cells and Light Emitting Diodes* (Ed: F. Gao), Elsevier, Amsterdam **2019**, p. 305.
- [263] Y.-H. Kim, S. Kim, A. Kakekhani, J. Park, J. Park, Y.-H. Lee, H. Xu, S. Nagane, R. B. Wexler, D.-H. Kim, S. H. Jo, L. Martínez-Sarti, P. Tan, A. Sadhanala, G.-S. Park, Y.-W. Kim, B. Hu, H. J. Bolink, S. Yoo, R. H. Friend, A. M. Rappe, T.-W. Lee, *Nat. Photonics* **2021**, *15*, 148.
- [264] T. Chiba, S. Ishikawa, J. Sato, Y. Takahashi, H. Ebe, S. Ohisa, J. Kido, *Adv. Opt. Mater.* **2020**, *8*, 2000289.
- [265] M. C. Brennan, S. Draguta, P. V. Kamat, M. Kuno, *ACS Energy Lett.* **2018**, *3*, 204.
- [266] A. J. Knight, L. M. Herz, *Energy Environ. Sci.* **2020**, *13*, 2024.
- [267] M. Kuno, M. C. Brennan, *Matter* **2020**, *2*, 21.

- [268] Z. Chu, Y. Zhao, F. Ma, C.-X. Zhang, H. Deng, F. Gao, Q. Ye, J. Meng, Z. Yin, X. Zhang, J. You, *Nat. Commun.* **2020**, *11*, 4165.
- [269] N. Yantara, N. F. Jamaludin, B. Febriansyah, D. Giovanni, A. Bruno, C. Soci, T. C. Sum, S. Mhaisalkar, N. Mathews, *ACS Energy Lett.* **2020**, *5*, 1593.
- [270] S. Yuan, Z.-K. Wang, L.-X. Xiao, C.-F. Zhang, S.-Y. Yang, B.-B. Chen, H.-T. Ge, Q.-S. Tian, Y. Jin, L.-S. Liao, *Adv. Mater.* **2019**, *31*, 1904319.
- [271] Z. Li, Z. Chen, Y. Yang, Q. Xue, H.-L. Yip, Y. Cao, *Nat. Commun.* **2019**, *10*, 1027.
- [272] K.-H. Wang, Y. Peng, J. Ge, S. Jiang, B.-S. Zhu, J. Yao, Y.-C. Yin, J.-N. Yang, Q. Zhang, H.-B. Yao, *ACS Photonics* **2019**, *6*, 667.
- [273] Y. Dong, Y.-K. Wang, F. Yuan, A. Johnston, Y. Liu, D. Ma, M.-J. Choi, B. Chen, M. Chekini, S.-W. Baek, L. K. Sagar, J. Fan, Y. Hou, M. Wu, S. Lee, B. Sun, S. Hoogland, R. Quintero-Bermudez, H. Ebe, P. Todorovic, F. Dinic, P. Li, H. T. Kung, M. I. Saidaminov, E. Kumacheva, E. Spiecker, L.-S. Liao, O. Voznyy, Z.-H. Lu, E. H. Sargent, *Nat. Nanotechnol.* **2020**, *15*, 668.
- [274] G. S. Kumar, R. R. Sumukam, B. Murali, *J. Mater. Chem. C* **2020**, *8*, 14334.
- [275] L. Zhang, C. Sun, T. He, Y. Jiang, J. Wei, Y. Huang, M. Yuan, *Light: Sci. Appl.* **2021**, *10*, 61.
- [276] Y. Shang, G. Li, W. Liu, Z. Ning, *Adv. Funct. Mater.* **2018**, *28*, 1801193.
- [277] H. Lu, X. Zhu, C. Miller, J. S. Martin, X. Chen, E. M. Miller, Y. Yan, M. C. Beard, *J. Chem. Phys.* **2019**, *151*, 204305.
- [278] M. Imran, P. Ijaz, L. Goldoni, D. Maggioni, U. Petralanda, M. Prato, G. Almeida, I. Infante, L. Manna, *ACS Energy Lett.* **2019**, *4*, 819.
- [279] S. Kumar, J. Jagielski, T. Marcato, S. F. Solari, C.-J. Shih, *J. Phys. Chem. Lett.* **2019**, *10*, 7560.
- [280] Z. Dang, B. Dhanabalan, A. Castelli, R. Dhall, K. C. Bustillo, D. Marchelli, D. Spirito, U. Petralanda, J. Shamsi, L. Manna, R. Krahn, M. P. Arciniegas, *Nano Lett.* **2020**, *20*, 1808.
- [281] S. Kumar, J. Jagielski, N. Kallikounis, Y.-H. Kim, C. Wolf, F. Jenny, T. Tian, C. J. Hofer, Y.-C. Chiu, W. J. Stark, T.-W. Lee, C.-J. Shih, *Nano Lett.* **2017**, *17*, 5277.
- [282] S. B. Naghadeh, S. Sarang, A. Brewer, A. L. Allen, Y.-H. Chiu, Y.-J. Hsu, J.-Y. Wu, S. Ghosh, J. Z. Zhang, *J. Chem. Phys.* **2019**, *151*, 154705.
- [283] Y. Ling, Z. Yuan, Y. Tian, X. Wang, J. C. Wang, Y. Xin, K. Hanson, B. Ma, H. Gao, *Adv. Mater.* **2016**, *28*, 305.
- [284] J. Cui, Y. Liu, Y. Deng, C. Lin, Z. Fang, C. Xiang, P. Bai, K. Du, X. Zuo, K. Wen, S. Gong, H. He, Z. Ye, Y. Gao, H. Tian, B. Zhao, J. Wang, Y. Jin, *Sci. Adv.* **2021**, *7*, eabg8458.
- [285] S. D. Stranks, R. L. Z. Hoye, D. Di, R. H. Friend, F. Deschler, *Adv. Mater.* **2019**, *31*, 1803336.
- [286] Z. Chen, Z. Li, T. R. Hopper, A. A. Bakulin, H.-L. Yip, *Rep. Prog. Phys.* **2021**, *84*, 046401.
- [287] Y. Jiang, M. Cui, S. Li, C. Sun, Y. Huang, J. Wei, L. Zhang, M. Lv, C. Qin, Y. Liu, M. Yuan, *Nat. Commun.* **2021**, *12*, 336.
- [288] J. Qin, X.-K. Liu, C. Yin, F. Gao, *Trends Chem.* **2021**, *3*, 34.
- [289] X. Zheng, Y. Hou, H.-T. Sun, O. F. Mohammed, E. H. Sargent, O. M. Bakr, *J. Phys. Chem. Lett.* **2019**, *10*, 2629.
- [290] D. Yang, X. Li, H. Zeng, *Adv. Mater. Interfaces* **2018**, *5*, 1701662.
- [291] F. Krieg, S. T. Ochsenbein, S. Yakunin, S. ten Brinck, P. Aellen, A. Süess, B. Clerc, D. Guggisberg, O. Nazarenko, Y. Shynkarenko, S. Kumar, C.-J. Shih, I. Infante, M. V. Kovalenko, *ACS Energy Lett.* **2018**, *3*, 641.
- [292] J.-N. Yang, Y. Song, J.-S. Yao, K.-H. Wang, J.-J. Wang, B.-S. Zhu, M.-M. Yao, S. U. Rahman, Y.-F. Lan, F.-J. Fan, H.-B. Yao, *J. Am. Chem. Soc.* **2020**, *142*, 2956.
- [293] A. Cervellino, R. Frison, F. Bertolotti, A. Guagliardi, *J. Appl. Crystallogr.* **2015**, *48*, 2026.
- [294] P. Scardi, L. Gelisio, *Sci. Rep.* **2016**, *6*, 22221.
- [295] S. ten Brinck, F. Zaccaria, I. Infante, *ACS Energy Lett.* **2019**, *4*, 2739.
- [296] Y. Wu, D. Wang, J. Liu, H. Cai, *Nanomaterials* **2021**, *11*, 775.
- [297] Y. Wang, Z. Zhang, M. Tao, Y. Lan, M. Li, Y. Tian, Y. Song, *Nanoscale* **2020**, *12*, 18563.
- [298] L. Xu, J. Li, B. Cai, J. Song, F. Zhang, T. Fang, H. Zeng, *Nat. Commun.* **2020**, *11*, 3902.
- [299] S. Watanabe, G. Tumen-Ulzii, T. Cheng, T. Matsushima, C. Adachi, *J. Phys. Chem. C* **2020**, *124*, 27422.
- [300] W. Zou, R. Li, S. Zhang, Y. Liu, N. Wang, Y. Cao, Y. Miao, M. Xu, Q. Guo, D. Di, L. Zhang, C. Yi, F. Gao, R. H. Friend, J. Wang, W. Huang, *Nat. Commun.* **2018**, *9*, 608.
- [301] J. P. Philbin, A. Brumberg, B. T. Diroll, W. Cho, D. V. Talapin, R. D. Schaller, E. Rabani, *J. Chem. Phys.* **2020**, *153*, 054104.
- [302] J. C. Yu, J. H. Park, S. Y. Lee, M. H. Song, *Nanoscale* **2019**, *11*, 1505.
- [303] R. L. Z. Hoye, J. Hidalgo, R. A. Jagt, J.-P. Correa-Baena, T. Fix, J. L. MacManus-Driscoll, *Adv. Energy Mater.* **2021**, <https://doi.org/10.1002/aenm.202100499>.
- [304] J. Pan, L. N. Quan, Y. Zhao, W. Peng, B. Murali, S. P. Sarmah, M. Yuan, L. Sinatra, N. M. Alyami, J. Liu, E. Yassitepe, Z. Yang, O. Voznyy, R. Comin, M. N. Hedhili, O. F. Mohammed, Z. H. Lu, D. H. Kim, E. H. Sargent, O. M. Bakr, *Adv. Mater.* **2016**, *28*, 8718.
- [305] T.-H. Han, S. Tan, J. Xue, L. Meng, J.-W. Lee, Y. Yang, *Adv. Mater.* **2019**, *31*, 1803515.
- [306] F. Cao, H. Wang, P. Shen, X. Li, Y. Zheng, Y. Shang, J. Zhang, Z. Ning, X. Yang, *Adv. Funct. Mater.* **2017**, *27*, 1704278.
- [307] Y. Hassan, J. H. Park, M. L. Crawford, A. Sadhanala, J. Lee, J. C. Sadighian, E. Mosconi, R. Shivanna, E. Radicchi, M. Jeong, C. Yang, H. Choi, S. H. Park, M. H. Song, F. De Angelis, C. Y. Wong, R. H. Friend, B. R. Lee, H. J. Snaith, *Nature* **2021**, *591*, 72.
- [308] D. Marongiu, M. Saba, F. Quochi, A. Mura, G. Bongiovanni, *J. Mater. Chem. C* **2019**, *7*, 12006.
- [309] V. Sarritzu, N. Sestu, D. Marongiu, X. Chang, Q. Wang, M. A. Loi, F. Quochi, M. Saba, A. Mura, G. Bongiovanni, *Adv. Opt. Mater.* **2018**, *6*, 1700839.
- [310] Q. Zhang, D. Zhang, Y. Fu, S. Poddar, L. Shu, X. Mo, Z. Fan, *Adv. Funct. Mater.* **2020**, *30*, 2002570.
- [311] M. J. Jurow, T. Morgenstern, C. Eisler, J. Kang, E. Penzo, M. Q. Do, M. Engelmayer, W. T. Osowiecki, Y. Bekenstein, C. J. Tassone, L.-W. Wang, A. P. Alivisatos, W. Brutting, Y. Liu, *Nano Lett.* **2019**, *19*, 2489.
- [312] T. Marcato, C.-J. Shih, *Helv. Chim. Acta* **2019**, *102*, e1900048.
- [313] W. L. Barnes, *J. Mod. Opt.* **1998**, *45*, 661.
- [314] J. Cui, Y. Liu, Y. Deng, C. Lin, Z. Fang, C. Xiang, P. Bai, K. Du, X. Zuo, K. Wen, S. Gong, H. He, Z. Ye, Y. Gao, H. Tian, B. Zhao, J. Wang, Y. Jin, *Sci. Adv.* **2021**, *7*, eabg8458.
- [315] K. Sudhir, M. Tommaso, K. Frank, L. Yen-Ting, C. Yu-Cheng, S. Chih-Jen, *Nature Portfolio* **2021**, *Preprint*, <https://www.researchsquare.com/article/rs-344894/v1>.
- [316] S. Kumar, J. Jagielski, S. Yakunin, P. Rice, Y.-C. Chiu, M. Wang, G. Nedelcu, Y. Kim, S. Lin, E. J. G. Santos, M. V. Kovalenko, C.-J. Shih, *ACS Nano* **2016**, *10*, 9720.
- [317] J. Si, Y. Liu, Z. He, H. Du, K. Du, D. Chen, J. Li, M. Xu, H. Tian, H. He, D. Di, C. Lin, Y. Cheng, J. Wang, Y. Jin, *ACS Nano* **2017**, *11*, 11100.
- [318] J. Lv, L. Fang, J. Shen, *Mater. Lett.* **2018**, *211*, 199.
- [319] D. Yang, Y. Zou, P. Li, Q. Liu, L. Wu, H. Hu, Y. Xu, B. Sun, Q. Zhang, S.-T. Lee, *Nano Energy* **2018**, *47*, 235.
- [320] W. Yin, M. Li, W. Dong, Z. Luo, Y. Li, J. Qian, J. Zhang, W. Zhang, Y. Zhang, S. V. Kershaw, X. Zhang, W. Zheng, A. L. Rogach, *ACS Energy Lett.* **2021**, *6*, 477.
- [321] B. A. Connor, L. Leppert, M. D. Smith, J. B. Neaton, H. I. Karunadasa, *J. Am. Chem. Soc.* **2018**, *140*, 5235.
- [322] V. M. Burlakov, Y. Hassan, M. Danaie, H. J. Snaith, A. Goriely, *J. Phys. Chem. Lett.* **2020**, *11*, 6535.
- [323] C. Bi, S. Wang, S. V. Kershaw, K. Zheng, T. Pullerits, S. Gaponenko, J. Tian, A. L. Rogach, *Adv. Sci.* **2019**, *6*, 1900462.



Clara Otero-Martínez received her master degree in chemical research and industrial chemistry from the University of Vigo in 2020. Now, she is a Ph.D. candidate in Materials Chemistry and Physics group with Dr. Lakshminarayana Polavarapu. Her research interests are focused on synthesis and study of the optical properties of hybrid and inorganic halides perovskites, and their optoelectronic applications.



Junzhi Ye received his bachelor degree in chemical and materials engineering at the University of Auckland, New Zealand. He is currently a Ph.D. student in Cavendish Laboratory, Department of Physics at the University of Cambridge (2019-). His primary supervisor is Dr. Akshay Rao, and cosupervised by Dr. Robert Hoye. His research interests are currently focused on perovskite optoelectronic devices, including perovskite quantum dots light-emitting diodes and perovskite-silicon tandem solar cells.



Jooyoung Sung is an assistant professor in the Department of Emerging Materials Science at DGIST (Korea, republic of). She completed her Ph.D. at Yonsei University (Republic of Korea) in 2016. As she won a postdoctoral research fellowship supported by National Research Foundation of Korea, Dr. Sung started post-doctoral research at University of Oxford (2016–2017). She carried out second post-doctoral research at Cavendish Laboratory, University of Cambridge (2017–2021) before joining DGIST from July, 2021. Her research interests are focused on revealing the hidden spatial dynamics of complex nanostructured semiconductors by utilizing various range of spectroscopic techniques.



Isabel Pastoriza-Santos obtained her Ph.D. degree in chemistry at the Universidade de Vigo (2001). She worked as a postdoctoral fellow at the University of Melbourne (Australia) between 2002 and 2003. In 2004 she got a postdoctoral research position at the University of Vigo. In 2009, she obtained a faculty position at the Department of Physical Chemistry of the University of Vigo. She is coauthor of about 145 articles. Her current interests include the synthesis of plasmonic nanoparticles and nanocomposites, as well as their use in sensing and catalysis.



Jorge Pérez-Juste has a Ph.D. from the University of Vigo (1999). He is currently an associate professor at the Biomedical Research Center at the University of Vigo. His research is focused on the synthesis and characterization of metal and semiconductor nanoparticles as well as the understanding of the mechanisms involved in nanoparticle growth, which determine the final size and shape. Besides, he is interested in the application of nanoparticles for photocatalysis.



Zhiguo Xia is presently a professor of materials chemistry and physics in the South China University of Technology. He obtained his bachelor degree in 2002 and master degree in 2005 from Beijing Technology and Business University, and he received his Ph.D. degree from Tsinghua University, Beijing in 2008. His research interests focus on designing new rare earth phosphors and luminescent metal halides for emerging photonics applications by integrating structural discovery, modification and structure–property relation studies.



Akshay Rao received his undergraduate degree from St Stephen's College, University of Delhi in 2006 and his M.Sc. from the University of Sheffield in 2007. He received his Ph.D. from the University of Cambridge in 2011, working in the group of Prof. Sir Richard Friend. From 2011 to 2014 he held a junior research fellowship at Corpus Christi College, Cambridge. As of October 2014 he has run an independent research group at the University of Cambridge and is an EPSRC Early Career Fellow & Winton Advanced Research Fellow. He was appointed to a Harding Lectureship in October 2019.



Robert L. Z. Hoye is a lecturer (assistant professor) in the Department of Materials at Imperial College London. There, he also holds a Royal Academy of Engineering Research Fellowship. He completed his Ph.D. at the University of Cambridge (2012–2014), before working as a postdoctoral researcher at the Massachusetts Institute of Technology (2015–2016). He subsequently received two College Research Fellowships at Cambridge, first at Magdalene College (2016–2019), then at Downing College (2019–2020), before taking up his Lectureship at Imperial in 2020. His research focuses on defect-tolerant semiconductors, and their development into optoelectronic devices.



Lakshminarayana Polavarapu obtained his M.Sc. in Chemistry from the University of Hyderabad (India) in 2005 and Ph.D. from the National University of Singapore in 2011. After postdoctoral research at CIC biomaGUNE and the University of Vigo in Spain, he joined the Chair for Photonics and Optoelectronics at the Ludwig-Maximilians-University of Munich (Germany) in 2015 as an Alexander von Humboldt postdoctoral fellow and later continued as a junior group leader. In 2020 he became the principal investigator of the Materials chemistry and physics research group at the Centro de Investigaciones Biomédicas (CINBIO), University of Vigo.